Circulation, dynamics and variability in Australia's boundary currents

Author:
Bull, Christopher

Publication Date:
2018

DOI:
https://doi.org/10.26190/unsworks/20502

Climate Change Research Centre

University of New South Wales

Circulation, Dynamics and Variability in Australia's Boundary Currents

Christopher Yit Sen Bull

January 2018

A thesis submitted in fulfilment of the requirements for the degree of Doctor of Philosophy

THE UNIVERSITY OF NEW SOUTH WALES
Thesis/Dissertation Sheet

Surname or Family name: Bull

First name: Christopher | Other name/s: Yit Sen

Abbreviation for degree as given in the University calendar: PhD

School: Climate Change Research Centre | Faculty: Science

Title: Circulation, dynamics and variability in Australia's boundary currents

Abstract:
Meridional heat transport around Australia is determined by Australia's two poleward flowing boundary currents: the East Australian Current (EAC) and Leeuwin Current (LC). This thesis aims to improve our understanding of the circulation, variability and dynamics of the LC and EAC by characterising the importance of bathymetry and non-linear processes in terms of the role of eddy fluxes and forcing variability.

In Part 1, a quantitative assessment of LC pathways suggests that more than half of LC source waters originate from tropical waters. The Lagrangian framework quantifies the preference for LC waters to exit the LC north of 30S; if the LC waters travel beyond this latitude, then they are more likely to continue downstream. In particular, eddy fluxes allow only limited transport (0.2 Sv) to travel the entire length of the LC into the Great Australian Bight.

In Part 2, we examine the role of deep bathymetry in the EAC separation by removing New Zealand. We find that the complete removal of New Zealand leads to the EAC mean separation latitude shifting >100km southward. We remove New Zealand with a hierarchy of linear models of increasing complexity; we find that linear processes and deep bathymetry play a major role in the Tasman Front position, whereas non-linear processes are crucial for the extent of the EAC retroflection. Contrary to previous work, we find that meridional gradients in the basin-wide wind stress curl are not the sole factor determining EAC separation.

Part 3 examines the EAC separation in terms of the role of local versus remote forcing variability in setting the mean state of the Tasman Sea circulation. We find that local, variable wind stress forcing, with a period shorter than ~2 months, results in a rectified Tasman Sea circulation. The increased extent of the EAC extension is characterized by increases in eddy shedding rates, southward eddy propagation and increased EAC extension transports. An energetics framework suggests that these EAC extension changes are coincident with increases in offshore, upstream eddy variance (via near-surface barotropic instability) as well as increases in subsurface mean kinetic energy along the path of the EAC.

Originality Statement

'I hereby declare that this submission is my own work and to the best of my knowledge it contains no materials previously published or written by another person, or substantial proportions of material which have been accepted for the award of any other degree or diploma at UNSW or any other educational institution, except where due acknowledgement is made in the thesis. Any contribution made to the research by others, with whom I have worked at UNSW or elsewhere, is explicitly acknowledged in the thesis. I also declare that the intellectual content of this thesis is the product of my own work, except to the extent that assistance from others in the project's design and conception or in style, presentation and linguistic expression is acknowledged.'

Signed ………………………………………………...........

Date …13/01/2018………………………………………….

Copyright Statement

Authenticity Statement

'I certify that the Library deposit digital copy is a direct equivalent of the final officially approved version of my thesis. No emendation of content has occurred and if there are any minor variations in formatting, they are the result of the conversion to digital format.'

Signed ………………………………………………………...........................

Date …13/01/2018……………………………………………….......

Acknowledgements

I would like to thank my supervisors and collaborator, in order of appearance as follows. I am grateful to Erik van Sebille, who sparked my interest in Australia's ocean circulation, provided valuable support early on, and shared his contagious enthusiasm for all things Lagrangian. I am also grateful to Matthew England for his boundless optimism and strategic advice/support; thank you for enabling the very best science and taking up the challenge of communicating across continents and universities. I am deeply thankful to Nicolas Jourdain whose timely, pragmatic NEMO expertise enabled so much of this project and provided an endearing, lasting heuristic for learning about ocean physics. Thank you Nico for showing me what an exceptional collaborator can be and always indulging my crazy ideas for new simulations. My deepest gratitude to Andrew Kiss, whose conscientious diligence, by example, is a tremendous source of inspiration; thank you for always putting the science first. Your insight, curiosity, and patience are greatly appreciated; it has been a privilege working with you!

I gratefully acknowledge the Australian Government Research Training Program Scholarship, Erik van Sebille's ARC DECRA Fellowship, Climate Change Research Centre (CCRC), ARC Centre of Excellence for Climate System Science, University of New South Wales and the National Computational Infrastructure for their financial, computational and logistical support of my candidature. This research could not have occurred without these excellent institutions, providing me with the opportunity to attend summer schools, conferences, visit other labs, run numerical simulations and foster collaborations. I am grateful to the groups who shared their model output data on which this thesis depends: Franziska Schwarzkopf, Arne Biastoch and Claus Böning at GEOMAR, Germany (TROPAC01) and Bernard Barnier and Jean-Marc Molines at IGE, France (ORCA025-L75-MJM95). I am also grateful for the excellent technical support provided by Martin Thompson and the CMS team. A special mention goes to the phenomenally effective CCRC admin team; particularly Stephen Gray whose commitment to student equity is deeply appreciated. Similarly, my heartfelt gratitude to Gab Abramowitz and Katrin Meissner, I cannot imagine better post-graduate coordinators. ‘Summer’ school directors: Melissa Hart, Martin Visbeck and Ian Turner, thank you. I also thank Chris Turney and Ken Ridgway for having me on the AAE and EAC cruises, respectively; both experiences greatly enriched my PhD experience.

The CCRC is the finest example of a positive (research) workplace culture that I have known; a dear thank-you to the students and staff, both former and present, that embody this sentiment. I would also like to acknowledge Gurvan Madec and Paulo Polito whose openness, warmth and generosity during their brief CCRC visit were touching. Similarly, I am indebted to Eric Oliver for sharing his Godfrey Island Rule and eddy tracking codes. I would like to thank Ryan Holmes and David Hutchinson for their sage advice. I acknowledge Nadja Herger for her assistance with Figure 0-1. I am grateful to Andy Hogg and the GFD group at ANU, for welcoming me on numerous occasions. Special thanks to Marcus Thatcher at CSIRO whom facilitated my first climate modelling experience; our sprawling discussions and your generous mentorship helped consolidate my interest in the field.

Swa Rath, I dearly appreciate you making Sydney feel like my new home. Alice Barthel, what a swashbuckling, intellectual adventure we have had, thank you! My ardent recognition to Julian Berton and Ben Fisk for our lucid dreaming in the vertical. My sincere thanks to Lee Sen Chai and Gordon Bull whose love and support continue to know no bounds. And Hilary, my deepest thanks, your unwavering, fervent love (and baked goods) provided the courage to carry on.

Thesis Summary

The meridional heat transport around Australia is determined by Australia's two poleward flowing boundary currents: the East Australian Current (EAC) and the Leeuwin Current (LC). Australia's marine ecosystems are under increasing pressure from warming ocean temperatures, and improvements in future projections of Australia's coastal regions depend critically on our understanding of the dynamics of the LC and EAC. This thesis aims to improve our understanding of the circulation, variability and dynamics of the LC and EAC by characterising the importance of bathymetry and non-linear processes in terms of the role of eddy fluxes and forcing variability.

In Part 1, a quantitative assessment of LC pathways suggests that more than half of the LC source waters originate from tropical waters. The Lagrangian framework quantifies the preferential pathway for LC waters to bifurcate north of 30°S; beyond this latitude they are more likely to continue downstream. We find that eddy fluxes allow only very limited transport (0.2 Sv) to travel the entire length of the LC into the Great Australian Bight.

In Part 2, we examine the role of deep bathymetry in the EAC separation by removing New Zealand and its associated bathymetry whilst retaining the same atmospheric forcing. We find that the removal of the New Zealand plateau leads to the EAC mean separation latitude shifting >100km southward. To expose the underlying dynamics, we remove New Zealand with a hierarchy of linear models of increasing complexity. We find that linear processes and deep bathymetry play a major role in the mean Tasman Front position, whereas non-linear processes are crucial for the extent of the EAC retroflection. Contrary to previous work, we find that meridional gradients in the basin-wide wind stress curl are not the sole factor determining EAC separation.

Part 3 extends our analysis of non-linear processes in the EAC separation in terms of the role of local versus remote forcing variability in setting the mean state of the EAC and Tasman Sea circulation. We find that local, variable wind stress forcing, with a period shorter than ~2 months, results in a rectified Tasman Sea circulation. The increased extent of the EAC extension is characterized by increases in eddy shedding rates, southward eddy propagation and increased EAC extension transports. An energetics framework suggests that these EAC extension changes are coincident with increases in offshore, upstream eddy variance (via near-surface barotropic instability) as well as increases in subsurface mean kinetic energy along the path of the EAC.

“The best climber in the world is the one having the most fun”

Alex Lowe

Contents

List of Tables

List of Figures

Supporting Publications

The main body of the thesis is composed of three parts, each part is published as a journal publication, specifically:

- Part 1. Status: published Journal of Geophysical Research: Oceans:
    - **Bull, C. Y. S.**, and E. van Sebille (2016), Sources, fate, and pathways of Leeuwin Current water in the Indian Ocean and Great Australian Bight: A Lagrangian study in an eddy-resolving ocean model, *Journal of Geophysical Research: Oceans*, 121(3), doi:10.1002/2015JC011486.

- Part 2. Status: published Journal of Geophysical Research: Oceans:
    - **Bull, C. Y. S.**, Kiss, A. E., van Sebille, E., Jourdain, N. C., & England, M. H. (2018). The role of the New Zealand plateau in the Tasman Sea circulation and separation of the East Australian Current, *Journal of Geophysical Research: Oceans*, 123. https://doi.org/10.1002/2017JC013412.

- Part 3. Status: published Journal of Geophysical Research: Oceans:
    - **Bull, C. Y. S.**, Kiss, A. E., Jourdain, N. C., England, M. H., & van Sebille, E. (2017). Wind forced variability in eddy formation, eddy shedding and the separation of the East Australian Current. *Journal of Geophysical Research: Oceans*, 122. https//doi.org/10.1002.2017JC013311.

Preface

This thesis aims to improve our understanding of the circulation, variability and dynamics of the Leeuwin Current and East Australian Current by characterising the importance of bathymetry and non-linear processes in terms of the role of eddy fluxes and forcing variability.

Motivation

Meridional ocean heat transport around Australia is fundamentally controlled by two poleward flowing boundary currents: the Leeuwin Current (LC) and East Australian Current (EAC) (see Figure 0-1). Australia's coastal marine environment is under increasing pressure from warming ocean temperatures (e.g. [*Wernberg et al.*, 2011; *Oliver et al.*, 2017]). In recent decades, an intensification of the equatorial trade winds in the Pacific Ocean and a southward shift / intensification in the westerly winds around Antarctica have been related to increased warm water and transport in the Indonesian Throughflow [*Lee et al.*, 2015] and a spin-up of the South Pacific gyre [*Cai et al.*, 2005; *Roemmich et al.*, 2016], respectively. As a result of these changes, the East Australian Current is thought to be extending further south [*Ridgway*, 2007a]. Impacts of the changes in the Indonesian Throughflow to the western Australian coastline are yet to be quantified. Improvements in future projections of Australia's coastal regions depend critically on our understanding of the dynamics of the LC and EAC.

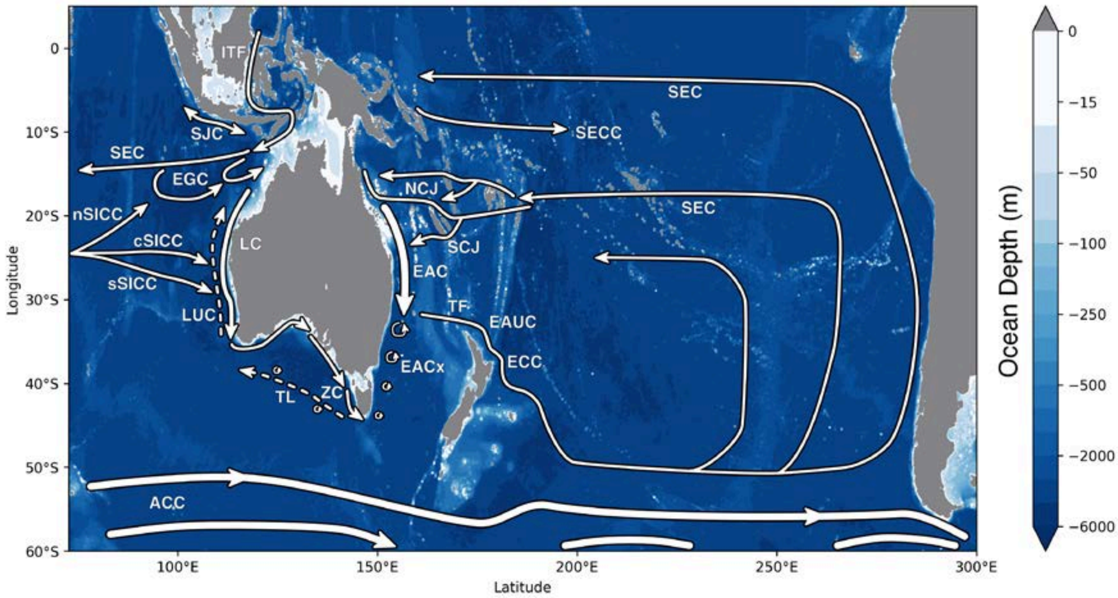

Figure 0-1. Time-mean large-scale currents around Australia. Ocean bathymetry is from ETOPO1 [*Amante and Eakins*, 2009]. Current abbreviations are: East Australian Current (EAC), East Australian Current extension (EACx), Tasman Leakage (TL) Zeehan Current (ZC), Leeuwin Undercurrent (LUC), Leeuwin Current (LC), north/central/south South Indian Countercurrent (nSICC, cSICC, sSICC), South Java Current (SJC), Eastern Gyral Current (EGC), South Equatorial Current (SEC), Indonesian Throughflow (ITF), North/South Caledonian Jet (NCJ/SCJ), Tasman Front (TF), East Auckland Current (EAUC), East Cape Current, South Equatorial Counter Current (SECC), Antarctic Circumpolar Current (ACC). Figure is adapted from [*Tomczak and Godfrey*, 2003; *Middleton and Bye*, 2007; *Ridgway*, 2007b; *Ganachaud et al.*, 2014; *Menezes et al.*, 2014b; *Hu et al.*, 2015].

To first order, the dynamics of the LC are described by linear theory [*Kundu and McCreary*, 1986; *McCreary et al.*, 1986; *Weaver and Middleton*, 1989, 1990; *Furue et al.*, 2013]. A model realization of the large-scale surface time-mean geostrophic circulation is indicated by sea surface height contours in Figure 0-2 (or as a schematic in Figure 0-1). On the western side of Australia, the Indonesian Throughflow and Indian Ocean interior jets (the ITF and SICC jets pictured in Figure 0-1) create the necessary background state to drive the Leeuwin Current system [*Furue et al.*, 2013, 2017; *Schloesser*, 2014; *Lambert et al.*, 2016]. The Leeuwin Current is driven by a meridional pressure gradient in the eastern Indian Ocean; this pressure gradient is predominantly due to easterly trade winds in the Pacific, which force warm, low-density tropical Pacific water into the eastern Indian Ocean via the Indonesian Throughflow (density gradient pictured in Figure 0-2a). The resulting pressure gradient then overwhelms the equatorward geostrophic flow expected from the local offshore Ekman transport, resulting in a net poleward transport. Despite major improvements in numerical modelling of the ocean circulation around Australia in recent years, and many additions to the simple linear theories outlined above (e.g. [*Batteen and Miller*, 2009; *Furue et al.*, 2013; *Benthuysen et al.*, 2014a]), fundamental uncertainties regarding the role of mesoscale variability in the LC remain. This thesis will address this by examining the role of eddy fluxes in controlling the circulation and variability of Leeuwin Current.

To first order, the dynamics of the EAC are also explicable by linear theory [*Tomczak and Godfrey*, 1994] and are described as follows. The anti-cyclonic South Pacific wind stress curl (pictured in Figure 0-2b) results in downward Ekman pumping. *Sverdrup* [1947], showed that the subsequent squeezing of fluid parcels decreases the magnitude of their associated potential vorticity, and since relative vorticity is negligible compared to planetary vorticity in the ocean at large scales, an equatorward flow arises to compensate. *Stommel* [1948] adds linear bottom friction which acts as a vorticity sink, leading to a western intensified boundary current. Aside from a constant offset due to the *Godfrey* [1989] Island Rule, the transport close to the western boundary then is determined by the zonally integrated wind stress curl across the basin (thick green line pictured in Figure 0-2b). A commonly used application of this linear theory (e.g. [*Tilburg et al.*, 2001; *Bostock et al.*, 2006; *Oliver and Holbrook*, 2014]) is that the EAC partially separates from Australia's coast at a latitude where the meridional gradient in the zonally-integrated wind stress curl is locally large (unlike some other western boundary currents there is no zero crossing of the integrated wind stress curl). Like the Leeuwin Current, despite many additions to the simple linear theories outlined above (e.g.

[*Marchesiello and Middleton*, 2000; *Mata et al.*, 2006]), fundamental uncertainties regarding the role of non-linear processes and eddy fluxes in the EAC remain. This thesis will also address some of these non-linear effects by examining the role of deep bathymetry and forcing variability on the EAC separation and Tasman Sea circulation.

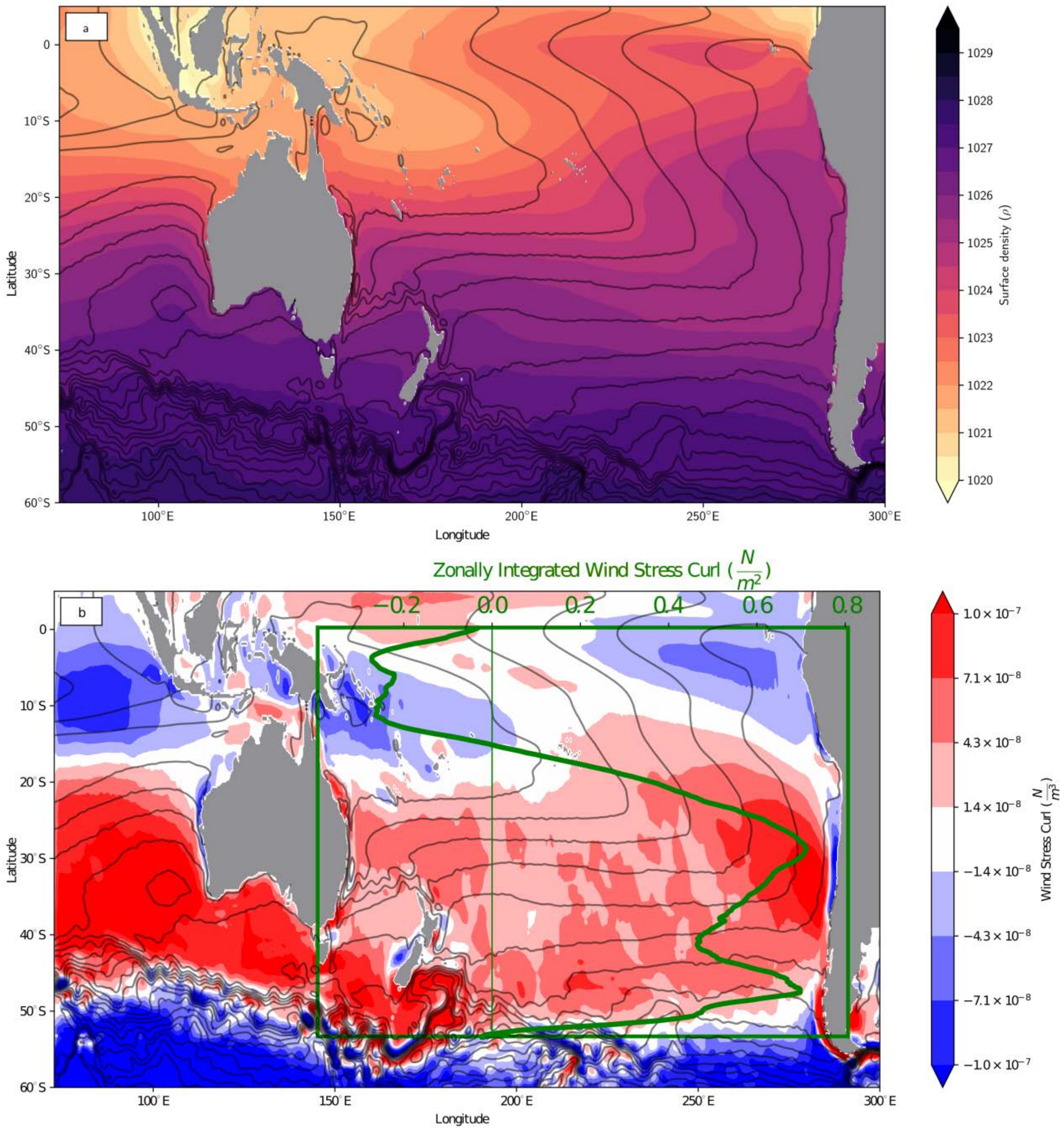

Figure 0-2. Schematic of the key factors determining the time-mean circulation of the Leeuwin Current (a) and East Australian Current (b). The grey contours in both panels show sea surface height, indicative of the time-mean surface geostrophic flow. a) The

Indonesian Throughflow (pictured in Figure 0-1) transports warm, low-density water creating a meridional density gradient (filled contours) driving the Leeuwin Current. b) the trade/westerly winds create an anti-cyclonic curl structure in the South Pacific Ocean (filled contours), driving the subtropical gyre in the South Pacific. The zonal integral of the wind stress curl across the South Pacific basin (thick green line in green box) and a constant offset due to the *Godfrey* [1989] Island Rule determines the meridional Sverdrup transport at the western boundary of the gyre. All fields from ORCA025-L75-MJM95 (global model used in Part 2 and Part 3).

A characterisation of the non-linear processes that set the time-mean circulation in the eastern Indian Ocean and Tasman Sea is essential if we wish to improve uncertainties in climate simulations. Important questions, which define the scope of this thesis include:

1. What is the role of eddies in determining water parcel trajectories along the Leeuwin Current?
2. Is there a pathway of water between the Indonesian Throughflow and the Leeuwin Current, and if so, what transport rate is involved?
3. Is the meridional gradient in the wind stress curl the sole factor that determines the EAC partial separation?
4. What is the role of non-linear processes (e.g. advection term in the momentum equations) in setting the EAC retroflection location?
5. Is remote ocean variability or local surface variability important in setting the time-mean Tasman Sea circulation?
6. What factors determine the rate of EAC eddy shedding? Does a variable wind stress affect the upstream stability of the EAC?

In essence the answers to these questions will extend our understanding of the key processes that drive the time-mean circulation around Australia.

Thesis structure and objectives

This thesis is presented as three separate parts, all using the ocean circulation model Nucleus for European Modelling of Ocean (NEMO) [*Madec*, 2012] in a regional configuration around Australia. The three parts are summarised:

- Part 1 uses a Lagrangian framework to investigate the sources, fate and pathways of Leeuwin Current water in the Indian Ocean and Great Australian Bight;

- Part 2 investigates the role of New Zealand, and the associated bathymetry, in the Partial separation of the East Australian Current and circulation of the Tasman Sea;

- Part 3 focuses on the East Australian Current's response to both local and remote forcing variability.

The NEMO modeling configuration is used for a series of sensitivity experiments aimed at exposing the underlying processes and dynamics necessary to resolve different aspects of the circulation. Part 1 utilises the most complete simulation, an eddy-resolving fifty-year hindcast TROPAC01 (NEMO) experiment, designed to characterise the role of eddies in driving the circulation in the Leeuwin Current. To reduce computational cost and facilitate a large number of simulations, Part 2 and Part 3 utilises a regional eddy-permitting NEMO configuration. As much as possible, the physics options in NEMO and the forcing used are the same across Part 2 and Part 3, enabling insight gained from Part 2 to be readily applied to Part 3.

Part 2 involves a highly idealized scenario, namely the removal of New Zealand. This approach is not, of course, part of any proposed grand engineering project, but instead aimed at improving our understanding of the underlying dynamics of the EAC and other components of the Tasman Sea circulation. Specifically, Part 2 suggests that non-linear processes and deep bathymetry are crucial in determining the separation of the East Australian Current and position of the Tasman Front, respectively. The Part 2 comparison of the Sverdrup / Godfrey Island Rule [*Sverdrup*, 1947; *Godfrey*, 1989] solution with linear NEMO suggests forcing variability may be important for the EAC separation; this is subsequently investigated in Part 3. Thus, the highly idealized approach of Part 2 builds the foundation for a more sophisticated, realistic examination of non-linear EAC separation dynamics and the role of variable forcing in Part 3.

The modeling approach used in this thesis offers some advantages as compared to previous studies in the region. In Part 1, we release virtual Lagrangian particles *offline*, enabling the first quantitative assessment of Leeuwin Current pathways. In Part 2 and Part 3, running an ocean-only model allows an examination of intrinsic ocean dynamics without confounding issues of ocean-atmosphere interactions. The regional configuration used in Part 3 facilitates a novel suite of experiments; we examine the relative role of local and remote variability on setting the EAC mean state. Whilst Part 2 and Part 3 employ idealized configurations to uncover the underlying dynamics within a sensitivity framework, at ¼° degree resolution they also offer a realism that is beyond virtually all CMIP5 models (that are typically run at ~1° degree horizontal resolution). Our experiment sets are also novel in that they progress from idealized scenarios through to a fully realistic simulation, with small increments that allow a detailed analysis of the underlying ocean dynamics at play.

The rest of this thesis is divided into three parts, corresponding to the three lead-authored publications listed in the Supporting Publications (see Supporting Publication, page xv). Each part consists of a self-contained and complete scientific article, including an abstract, full introduction, methods, results, discussion and conclusion; this preface is thus purposefully limited in its coverage of introductory material. While each part is self-contained, the references are compiled into a single bibliography at the end of the thesis. Finally, a Concluding Remarks section (page 99) provides a summary of the key findings of the thesis as well as recommendations for future research.

Part 1. Sources, fate, and pathways of Leeuwin Current water in the Indian Ocean and Great Australian Bight: A Lagrangian study in an eddy-resolving ocean model.

Part 1 contains a reformatted version of the published manuscript:

Bull, C. Y. S., and E. van Sebille (2016), Sources, fate, and pathways of Leeuwin Current water in the Indian Ocean and Great Australian Bight: A Lagrangian study in an eddy-resolving ocean model, *Journal of Geophysical Research: Oceans*, 121(3), doi:10.1002/2015JC011486.

Abstract

The Leeuwin Current is the dominant circulation feature in the eastern Indian Ocean, transporting tropical and subtropical water southward. Whilst it is known that the Leeuwin Current draws its water from a multitude of sources, existing Indian Ocean circulation schematics have never quantified the fluxes of tropical and subtropical source water flowing into the Leeuwin Current. This paper uses virtual Lagrangian particles to quantify the transport of these sources along the Leeuwin Current's mean pathway. Here, the pathways and exchange of Leeuwin Current source waters across six coastally bound sectors on the south-west Australian coast are analysed. This constitutes the first quantitative assessment of Leeuwin Current pathways within an offline, 50-year integration time, eddy-resolving global ocean model simulation. Along the Leeuwin Current's pathway we find a mean poleward transport of 3.7 Sv in which the tropical sources account for 60-78% of the transport. Whilst the net transport is small, we see large transports flowing in and out of all the offshore boundaries of the Leeuwin Current sectors. Along the Leeuwin Current's pathway, we find that water from the Indonesian Throughflow contributes 50-66% of the seasonal signal. By applying conditions on the routes particles take entering the Leeuwin Current, we find particles are more likely to travel offshore north of 30°S, while south of 30°S particles are more likely to continue downstream. We find a 0.2 Sv pathway of water from the Leeuwin Current's source regions, flowing through the entire Leeuwin Current pathway into the Great Australian Bight.

1.1 Introduction

The surface Leeuwin Current is a globally unique eastern boundary current, flowing poleward year round [*Smith et al.*, 1991], it transports fresh, warm water into the Western and South Australian coastlines [*Waite et al.*, 2007]. An observationally based study [*Ridgway and Condie*, 2004] showed that the surface Leeuwin Current is the western part of a 5500 km system of currents originating at the North West Cape of Australia (114°E, 22°S) and extending to the southern tip of Tasmania (approx. 146°E, 44°S). However, the circulation off the western coast of Australia is more complicated than a continuous coastal flow confined to the continental slope. Compared to other eastern boundary currents, the Leeuwin Current is rich in eddy activity [*Feng et al.*, 2005]; mesoscale eddies generated from mixed barotropic and baroclinic instability play an important role in transporting heat and salt offshore [*Morrow et al.*, 2003]. Moreover, the Leeuwin Current is not the only named current in the region. Slightly farther offshore and deeper than the surface Leeuwin Current flows the Leeuwin undercurrent, an equatorward flowing subsurface current [*Woo and Pattiaratchi*, 2008]. Inshore of the surface Leeuwin Current are the summer only, wind driven equatorward Ningaloo Current and Capes Current, located between 22-24°S [*Woo et al.*, 2006] and 33-34°S [*Pearce and Pattiaratchi*, 1998; *Gersbach et al.*, 1999], respectively.

The surface Leeuwin Current is an important pathway for water originating in the Pacific Ocean to enter into Australia's boundary current system. Since *Kundu and McCreary* [1986] it has been suggested that the Leeuwin Current, via the Indonesian Throughflow, provides a pathway for water coming from the Pacific Ocean into western Australia's coastlines. A more recent Lagrangian modelling study [*Domingues et al.*, 2007] confirmed this general pathway, but the quantitative contribution of this source remains unclear [*Furue et al.*, 2013]. In the context of the recent warming air temperature hiatus, the Indonesian Throughflow has transported 70% of the Pacific Ocean's anomalous heat in the past decade into the upper 700m of the Indian Ocean [*Lee et al.*, 2015]. The multi-decadal trend in stronger Pacific trade winds corresponds to stronger Leeuwin Current transport [*Feng et al.*, 2011] and is a contributing factor to the unprecedented 2011 marine heat wave off Western Australia [*Feng et al.*, 2013; *Benthuysen et al.*, 2014b]. Thus, to understand the regional impact of the anomalous ocean heat in the Indian Ocean and identify/characterise Australia's extreme ocean warming events in the future, a more thorough understanding of the Leeuwin Current's tropical sources is needed.

The surface Leeuwin Current is also an important component of the large scale circulation in the Indian Ocean. Using a five year POP11B model simulation with a Lagrangian framework where water parcels are tracked, *Domingues et al.* [2007] found that water leaving the Indonesian Throughflow exits in the South Java Current and then returns eastward in the Eastern Gyral Current. *Domingues et al.* [2007] found an additional tropical source region for the Leeuwin Current, that is, water flowing from the equatorial Indian Ocean via the South Java Current. From the subtropical Indian Ocean, *Domingues et al.* [2007] found water entering the Leeuwin Current via the southern branch of the South Indian Countercurrent (SICC) (here, the definition is from [*Menezes et al.*, 2014b], however the SICC was discovered by [*Siedler et al.*, 2006; *Palastanga et al.*, 2007]). More recently, *Menezes et al.* [2014b] has better resolved the SICC, this work suggests that the central branch of the SICC is also a source for the Leeuwin Current. These pathways have been corroborated observationally, examples include the use of in situ observations [*Woo and Pattiaratchi*, 2008; *Xu et al.*, 2015], Argo-based atlases and satellite data [*Menezes et al.*, 2013, 2014b]. Whilst the aforementioned studies describe the circulation of the region, they do not quantify the relative contributions of the different surface Leeuwin Current sources to the mean flow [*Furue et al.*, 2013].

Understanding of the fate of Leeuwin Current water is even more limited than that of its sources. Whilst the Leeuwin Current extends to around 300m [*Feng*, 2003], surface observations might give some insight into the fate of Leeuwin Current water. *Ridgway and Condie* [2004], however, when looking for surface drifters that had advected from the Leeuwin Current proper into the Great Australian Bight noted there was 'no single period in which drifters were deployed over the entire current path'. Due to this lack of observations, it is not well known how much water flows from the Leeuwin Current into the Great Australian Bight as compared to flowing offshore into the Indian Ocean.

Although there is a lack of quantitative estimates of the Leeuwin Current's water pathways, there are observationally based Eulerian estimates of transport across Leeuwin Current sections. An observationally based study by *Feng* [2003] found southward transports at 32°S of 3.4 Sv, 3.0 Sv and 4.2 Sv for the mean, El Niño and La Niña years respectively. Recent work by *Ridgway and Godfrey* [2015] suggests that the source of the Leeuwin Current's seasonal cycle is an annual sea level "pulse" starting in the Gulf of Carpentaria in November and travelling around Australia's coast as far as Tasmania by July. The seasonal variability of the Leeuwin Current is well established [*Ridgway and Condie*, 2004; *Meuleners et al.*, 2007; *Waite et al.*, 2007; *Hendon and Wang*, 2009]. The current is strongest in Austral winter when equatorward winds are weakest [*Smith et al.*, 1991; *Meuleners et al.*, 2007; *Hendon and Wang*, 2009]. In the most extensive field study to date, *Smith et al.* [1991] calculated the Leeuwin Current's alongshore southward transport at 29.5°S as ranging from< 2 Sv in February to >6 Sv in March and June.

The aims of this study are twofold. First, to quantify tropical and subtropical source exchanges in the Leeuwin Current. Specifically, we quantify how much water comes from the tropical Indonesian Throughflow, the tropical equatorial Indian Ocean and the subtropical interior western Indian Ocean. Second, to quantify the amount of water that goes into the Great Australian Bight compared to the amount of water that recirculates offshore into the Indian Ocean. Both of these questions will be addressed using a Lagrangian framework in the context of a 1/10° global ocean model over a fifty year time series.

This study builds on the aforementioned previous Lagrangian study [*Domingues et al.*, 2007] in a number of ways. Specifically, we use finer temporal resolution, namely five days compared to twenty days, and we study a longer temporal extent, namely fifty years compared to five years. As a result we are able to consider long term Leeuwin Current pathways and the seasonal cycle. Similarly, as our experiment is run offline we are able to track significantly more particles allowing for quantitative inferences. In addition, by defining sectors along the south west Australian coastline this work quantifies source exchange fluxes, source pathways and the seasonal cycle across and alongshore the south west Australian coastline. Finally, having a longer time series and a Lagrangian framework allows us to examine the fate of Leeuwin Current water farther downstream. Thus, this study extends the previous work by calculating transports and pathways associated with different Leeuwin Current sources.

The chapter is organised as follows. Section 1.2 describes the ocean model, Lagrangian framework and definition of the Leeuwin Current sectors used in this paper. Results are examined in section 1.3. Section 1.4 provides a summary and comparison of results, closing with a discussion of the limitations of the work, its broader importance and suggestions for future work.

1.2 The Model and Methods

1.2.1 Ocean General Circulation Model

In this study, the sources and destinations of Leeuwin Current water are studied using the high-resolution TROPAC01 model. This model configuration, developed by the European Drakkar cooperation [*Barnier et al.*, 2007], is based on NEMO [*Madec*, 2008] code. It is a 1/10° horizontal resolution model of the tropical Indo-Pacific region (73°E–63°W to 49°S–31°N), nested within a half-degree global ocean/sea-ice model. In the vertical, TROPAC01 has 46 z-levels: 10 levels in the top 100m and a maximum layer thickness of 250m at depth, whereby bottom cells are allowed to be partially filled [*Barnier et al.*, 2007]. The COREv2-IA atmospheric forcing is used in this study, it has been designed to aid our understanding of the observed ocean record and has broad usage with global ocean-ice models as established by the Coordinated Ocean-ice Reference Experiments [*Griffies et al.*, 2009]. The atmospheric forcing builds on the CORE reanalysis products developed by *Large and Yeager* [2008] covering the period 1948–2009 and is applied via bulk air-sea flux formulae. The TROPAC01 simulation uses laterally spatially varying eddy coefficients, namely, a Laplacian operator for iso-neutral diffusion of tracers and a bi-laplacian operator for lateral diffusion of momentum. TROPAC01 is run with a prognostic turbulent kinetic energy scheme [*Gaspar et al.*, 1990] for vertical mixing. Further details in *Madec* [2008]. For the analysis, 50 years (1960–2009) of data from the TROPAC01 hind-cast experiment will be used, with temporal means available every 5 days. The combination of output every five days, over a long time series with eddy-resolving resolution enables us to address a range of questions on different temporal and spatial scales.

With reasonable accuracy, the model reproduces the major circulation features in the region. This is evident when comparing the overlapping time period of 1993–2009 in terms of simulated sea-surface height with AVISO altimetry data (Figure 1-1). In *van Sebille et al.* [2014], using the same model, the authors note an extended tongue of elevated sea surface height in the model Indian Ocean at around 15°S, which is confined to the far eastern basin in the altimetry data. We can see that other biases in our region of interest are relatively small, except for the slightly higher sea surface height values very close to the coast. The variability of sea surface height in the model is also in good agreement when compared to altimetry (Figure 1-1d-e), we see the south Indian Ocean is eddy rich (e.g. [*Feng et al.*, 2005]). As *van Sebille et al.* [2014] noted, TROPAC01 tends to underestimate more energetic regions (Figure 1-1f) with the exception of coastal areas. These coastal discrepancies (Figure 1-1c and Figure 1-1f), may be due to satellite performance deteriorating near coastal areas [*Saraceno et al.*, 2008] and therefore do not necessarily imply the model is doing a poor job.

1.2.2 Eulerian TROPAC01 validation at 32°S

As we are particularly interested in water transport in the Leeuwin Current region, we validate TROPAC01 against [*Feng*, 2003]. To minimise the effect of interannual variability, throughout this subsection we use TROPAC01's entire timeseries 1960-2009. In *Feng* [2003], Leeuwin Current variability (offshore of Fremantle) was reconstructed using a range of observations including Fremantle sea level and temperature/salinity records near Rottnest Island. TROPAC01's (Eulerian) mean and bimonthly mean velocity fields in Figure 1-2 may be compared to the geostophic velocities in Figure 6d and Figure 7c of [*Feng*, 2003] (respectively). From Figure 8 of [*Feng*, 2003] we know that the southward Ekman transport across this section is low and so its contribution to Figure 1-2 would be small. Figure 1-2 shows that along 32°S, like in

[*Feng*, 2003], the core of the Leeuwin Current is at 115°E and the velocity core tilts slightly toward the coast with increasing depth.

The bimonthly means in Figure 1-2 show that TROPAC01 performs well, qualitatively; in the summer months we see the characteristic weakening of the Leeuwin Current, as we approach the winter months we can see the expected deepening and widening of the core of the Leeuwin Current. Quantitatively, in both Figures the flow speeds are lower than the observed values but we notice that this effect on transport is cancelled out by the flow being broader (Figure 1-2). Depth integrating from 110°E to the continental edge at 32°S down to 270m gives a transport estimate of 2.9 Sv, this compares well with [*Feng*, 2003] of 3.4 Sv.

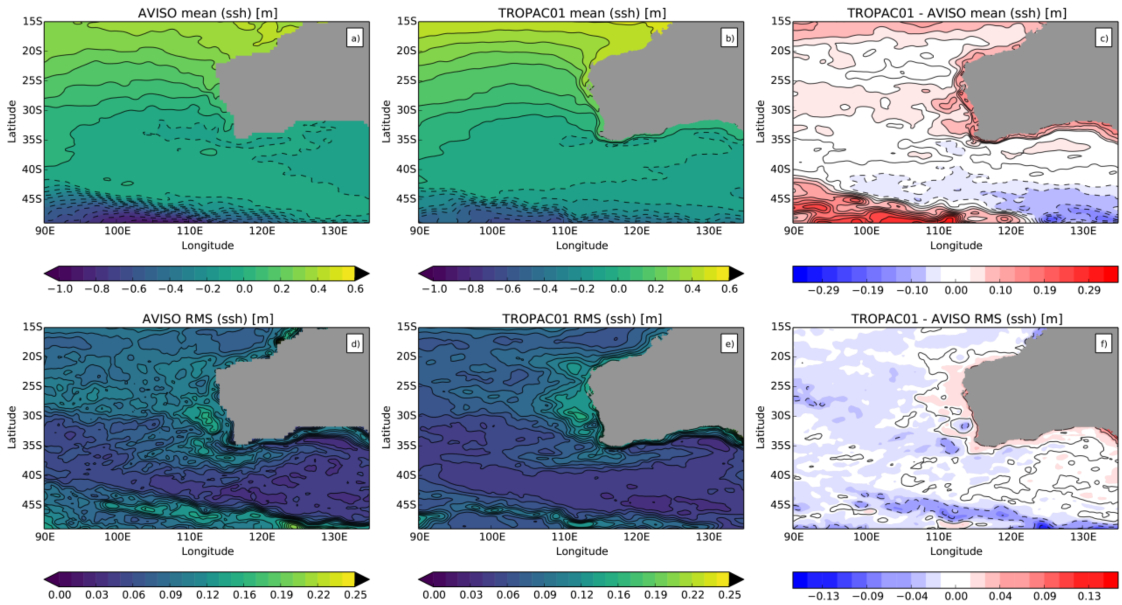

Figure 1-1. Evaluation of the TROPAC01 model: comparing the model sea surface height data for the period 1993–2009 to AVISO altimetry data over the same period. (a)-(c) comparison of mean sea surface height. (d)-(f) comparison of sea surface height variability, computed as the local root-mean-square variance of the sea surface height time series.

Figure 1-3 shows how well TROPAC01 reproduces the seasonality of the Leeuwin Current. We compare the monthly mean Eulerian transport between 1960-2009 in TROPAC01 at 32°S with *Feng's* [2003] (Figure 8) mean for years 1950-2000 at 32°S. This and the depth integration done above are typical means of validation for a model's transport for the Leeuwin Current (e.g. [*Smith et al.*, 1991; *Feng et al.*, 2008; *Hendon and Wang*, 2009; *Benthuysen et al.*, 2014b]). Given the different time periods, the agreement in Figure 1-3 is quite good, the seasonal cycle is captured well and the timing of the winter intensification of the Leeuwin Current agrees well with observations (e.g. [*Feng*, 2003]). Indeed, TROPAC01 has improved its representation of the seasonal cycle since previous versions of the model. In *Feng et al.* [2008] fields from the ORCA025-KAB001 (ORCA025) 0.25° model were analysed in the Leeuwin Current region. ORCA025 is an earlier version of TROPAC01 and used the same atmospheric forcing. Comparing Figure 1-3 here with Figure 5 from *Feng et al.* [2008], we see that the higher resolution TROPAC01 has increased summer transport and an improved timing of winter intensification; two issues *Feng et al.* [2008] raised when validating the earlier ORCA025 version of TROPAC01.

1.2.3 The Lagrangian particle model and setup

The Leeuwin Current sources, pathways and associated transports can most aptly be studied by tracking virtual Lagrangian particles in model velocity fields (e.g. [*van Sebille et al.*, 2013]). We use the Connectivity Modelling System (CMS) v1.1 [*Paris et al.*, 2013] to integrate the virtual particles in the three-dimensional time-evolving flow using a 4th order Runge-Kutta method.

As the focus is on the region around Australia, only data in a subdomain between 90°E–190°E and 49°S–15°N are used (pictured in Figure 1-9). Using the TROPAC01 dataset to track water masses into the Leeuwin Current, we release particles in the following known Leeuwin Current source regions. Specifically:

1. The *Indonesian Throughflow region* consisting of two zonal release sections and one meridional release section. A Karimata Strait release section at 4°S between 106-114.5°E with 0.1° horizontal spacing and 10 m vertical spacing. Another zonal section in Makassar and Moluccas Straits at 4°S between 115.6-134.6°E with 0.1° horizontal spacing and 50 m vertical spacing. A Torres Strait meridional release section along 142.5°E between 9.3-10.7°S with 0.1° horizontal spacing and 10 m vertical spacing. The vertical spacing in Karimata and Torres Straits has been reduced to accommodate for shallow bathymetry.
2. The *northern offshore* section: a zonal section at 4°S between 90.0-102.25°E with 0.25° horizontal spacing and 50 m vertical spacing.
3. The *western offshore* section: A meridional section along 90°E between 4-49°S with 0.5°degree horizontal spacing and 50 m vertical spacing.

These release sections are pictured in Figure 1-9, supplementary material. Maps of depth-integrated transport in Sverdrups into the Leeuwin Current region from each of the Indonesian straits, Torres Strait and both offshore Indian releases are shown in Figure 1-10.

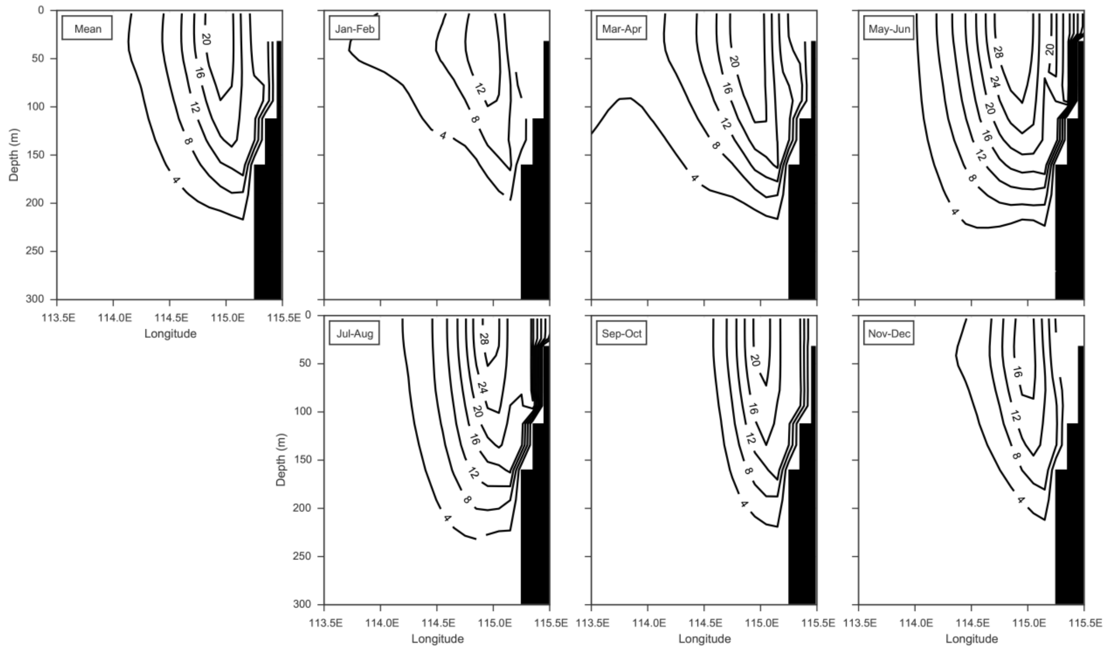

Figure 1-2. Mean (upper left) and bimonthly mean (1960-2009) meridional velocity (m/s) at 32°S in the TROPAC01 model. Contours are 0.04 m/s and only negative velocities are shown.

As the objective of the present work is to identify source contributions to the Leeuwin Current's mean flow, particles will not be allowed north of 4°S or west of 90°E. Meaning, once a particle crosses either of these lines, it is removed from the experiment from that point on. Particles are released every five days down to a depth of 1075 metres (where bathymetry allows). This is more than sufficient depth as neither the South Indian Countercurrent nor Leeuwin Current system extend below 1000 m [*Siedler et al.*, 2006; *Waite et al.*, 2007]. Since this study's focus is on Leeuwin Current trajectories, particles are only released if they have an initial southward/eastward trajectory for zonal/meridional sections, respectively. These three release sections equate to a tracking of 4.8 million particles.

Particle trajectories need to account for the ramp-up effect [*van Sebille et al.*, 2012, 2014], this ensures the particle transports are calculated once the spatial distribution of tracked particles is statistically steady in the areas of interest. In practice, the ramp up effect is determined by the time it takes for water to reach the south-eastern end of the Leeuwin Current region from the release locations. Specifically, out of all three releases, the water coming from the western offshore section takes the longest to be advected through the Leeuwin Current region. The distribution of transit times of western offshore particles suggests a ramp up time of ~6 years. This comes from the amount of time it takes 90% of the particles from the western offshore release section to arrive at the farthest area of interest in this paper: the Great Australian Bight. For this reason, for the remainder of this paper, across all sources, particles released between 1960-2003 that arrive in the Leeuwin Current region after 1965 are analysed.

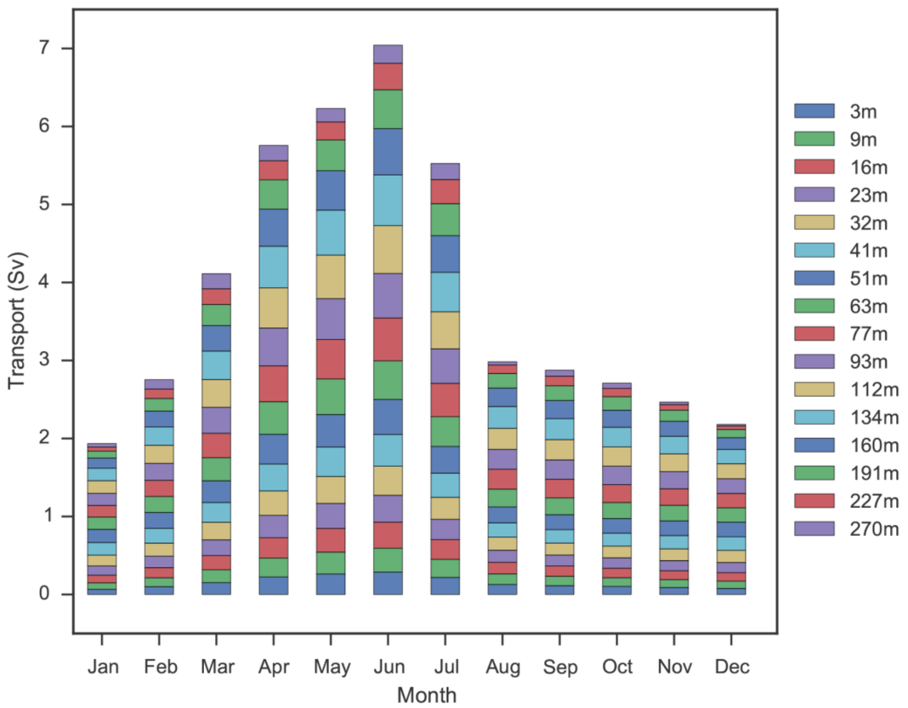

Figure 1-3. Eulerian southward transport from TROPAC01 at 32°S (110°E to the coast) for years 1960-2009. Bar colours are different groupings of levels from TROPAC01.

The particles are assigned a transport equal to the local velocity in the release grid cell times the area of that grid cell. The length of the release grid cell in this experiment varies on the release section, the release grid cell for each release section can be found in the release definitions above. The particles are then tracked forward in time until they reach one of the domain boundaries or until the end of the time series. Along a particle's trajectory, the particle maintains its original transport; this method has been used successfully by others, for example see [*Döös*, 1995; *Speich et al.*, 2002; *van Sebille et al.*, 2010, 2012] and the theoretical background in [*van Sebille et al.*, 2018]. This method has recently been validated in the Indonesian archipelago, yielding transports that largely agree with their Eulerian analogue [*van Sebille et al.*, 2014], namely a temporal correlation of R=0.64; significant at the 95% confidence level and total ITF Eulerian transport to be 14.0 Sv and a Lagrangian estimate of 14.3 Sv. Furthermore, this last paper demonstrated TROPAC01's capacity to simulate a realistic Indonesian Throughflow, which is important for the present work as the Leeuwin Current is partially forced by the Indonesian Throughflow [*Furue et al.*, 2013; *Schloesser*, 2014]. Previous versions of TROPAC01 have also been validated in a variety of ways in terms of the Leeuwin Current and Indonesian Throughflow [*Feng et al.*, 2008, 2011; *Schwarzkopf and Böning*, 2011].

1.2.4 Defining six coastally bound sectors along the south-west Australian coast

Since we are interested in the water mass source exchanges in the Leeuwin Current region, we define six adjacent sectors along the south-western coastal boundary of Australia (see black lines Figure 1-5). For the remainder of this paper, the sectors will be numbered 1-6 starting upstream in the northwest and then moving downstream south and east (as numbered in Figure 1-5). Studies such as [*Smith et al.*, 1991; *Feng et al.*, 2008; *Benthuysen et al.*, 2014b] suggest that the Leeuwin Current's mean flow does not meander beyond 200-300 km offshore.

1.3 Results

1.3.1 Particle connectivity from the Pacific Ocean and equatorial Indian Ocean to south western Australia

Figure 1-4 maps the proportion of transport in each 0.5° grid cell that enter the Leeuwin Current. Dark blue regions indicate that all particles (100%) that visit those grid cells pass through the Leeuwin Current at some point along their trajectories, while dark red regions indicate no particles (0%) visit the Leeuwin Current. Here, particles are defined to visit the Leeuwin Current region when they enter any of the six sectors defined in section 1.2.4 (black lines on Figure 1-4). As this section focuses on the tropical sources of the Leeuwin Current, Figure 1-4 does not consider particle trajectories from the western offshore source. Cells that are unshaded indicate grid cells where no trajectories entered.

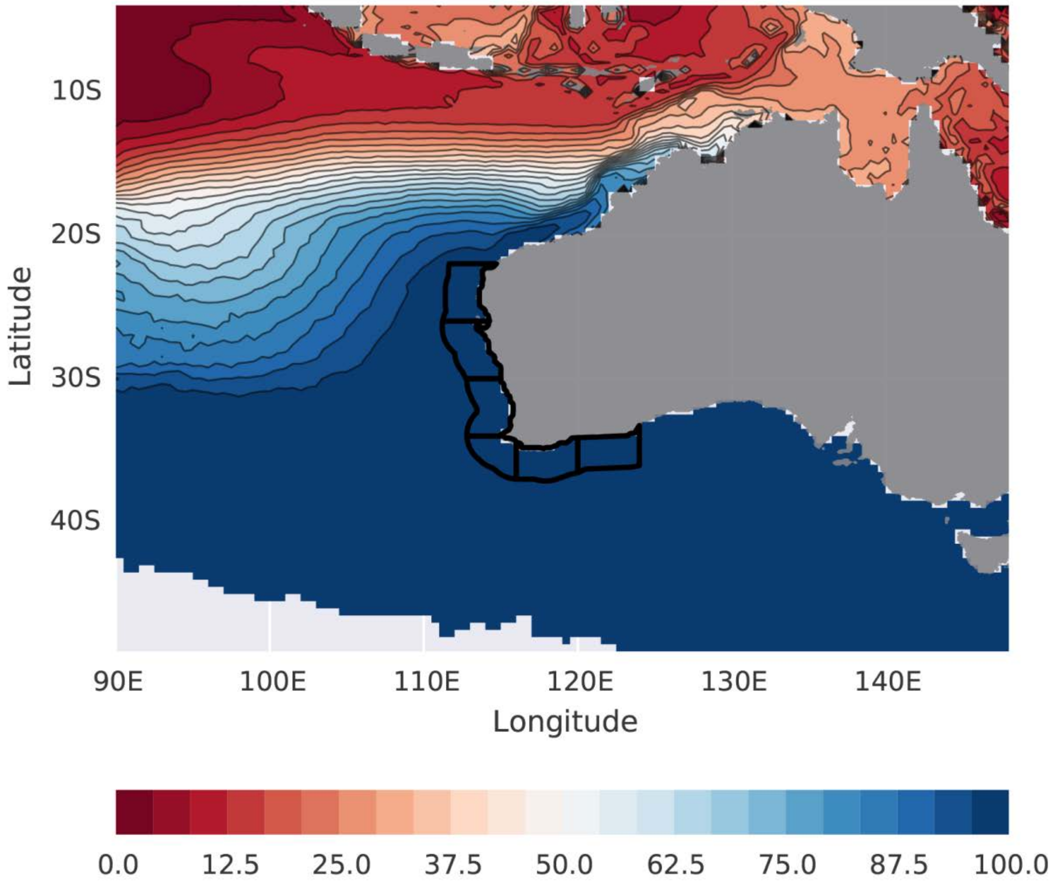

Figure 1-4. Connectivity map between the northern offshore/Indonesian Throughflow particles and the Leeuwin Current region as diagnosed from Lagrangian trajectories. The proportion of transport in each 0.5° × 0.5° degree grid cell from trajectories that entered the Leeuwin Current region (blue) and trajectories that did not (red). Any blue value above 50% indicates that grid cell was dominated by trajectories that entered the Leeuwin Current region. The Leeuwin Current region is defined as any sectors pictured by the thick black lines. This Figure demonstrates the importance of the Leeuwin Current as a pathway for water between the northern offshore region/Indonesian Throughflow and Australia's mid-latitude and South Australian coastlines.

Using Lagrangian trajectories, Figure 1-4 highlights the northern regions in the southeast Indian Ocean that are connected by the Leeuwin Current. Grid cells south of the 50% contour are dominated by particles bound for or coming from the Leeuwin Current region. The tongue of blue contours extending along the northwest shelf of Australia indicates that once water is near the northwest shelf of Australia it is likely to enter the Leeuwin Current region. Indeed, at approximately 19.5°S, 118.5°E the 100%

contour indicates that any particle in that location will enter the Leeuwin Current region (or has come from there). Similarly, comparing water southeast and west of the Indonesian Aru Islands (134°E), water on the south eastern side is more likely to end up in (or come from) the Leeuwin Current region. From Figure 1-4 we can conclude that within the domain presented, on the timescales available in the model, the only way for water originating in the low latitudes to get to mid-latitude and South Australia is to pass through the Leeuwin Current region. Thus, as expected the Leeuwin Current is the only western Australian pathway for water travelling from the tropical Pacific Ocean/equatorial Indian Ocean to mid-latitude and southern Australia.

1.3.2 Mean and seasonal source water exchanges in the Leeuwin Current region.

Figure 1-5 addresses a key objective of this paper, to quantify the tropical and subtropical source exchange in the Leeuwin Current region. Specifically, we have depth-integrated the Lagrangian transports (in Sv) from the surface to 300m across the borders of the (pictured) sectors, taking the mean over 1966-2003 (a date range shorter than the available model data, due to 'ramp-up effect', see section 1.2.3). The colour of the arrows represent the three different particle source releases (section 1.2.3): orange arrows are particles originating from the Indonesian Throughflow region, purple arrows are for the northern offshore release and green arrows for the western offshore release. See section 1.2.3 for the formal definition of these releases. This colouring scheme persists for Figure 1-6 and Figure 1-7. Size and direction of arrows are indicative of transport size and direction of flow (respectively). The sectors in Figure 1-5 have arrows in both directions as particles are allowed to circulate freely in the domain. We define *downstream flow* to mean the southward crossing of sectors 1/2/3 and eastward bound water for sectors 4/5/6 (as numbered in Figure 1-5).

Figure 1-6 and Figure 1-7 examine only the downstream flow. Reference to the Leeuwin Current's extension is meant to be any Leeuwin Current water rounding Cape Leeuwin heading east into sectors 5 and 6.

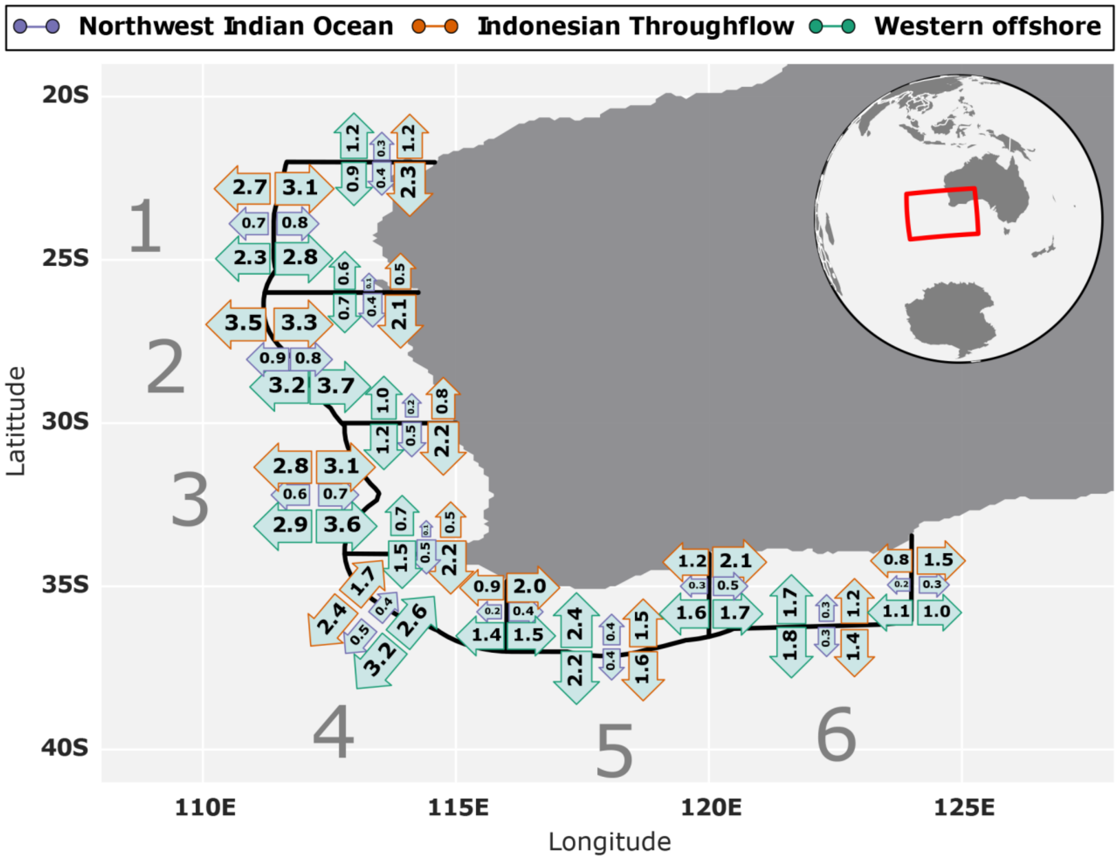

Figure 1-5. Source water exchange along the Leeuwin Current's pathway. Numbers are transport (Sv) across the pictured sector boundaries (black lines), taking the average for years 1966-2003 and depth-integrating to 300m. Orange arrows are particles originating from the Indonesian Throughflow region, purple arrows are from the northern offshore section and green arrows from the western offshore section. Size and direction of arrows are indicative of transport size and direction of flow, respectively.

The combined downstream alongshore transports in Figure 1-5 gives transport estimates of 3.6, 3.2, 3.9, 4.2, 3.9, 4.3, 2.8 Sv. These transports can be interpreted as the Lagrangian analogue of transport for the Leeuwin Current from observationally based studies (e.g. [*Smith et al.*, 1991; *Feng*, 2003]). The net southward transport 1.9 Sv and

2.6 Sv for sectors 2 and 3, respectively from Figure 1-5 are slightly higher than the core based estimates of ~1.5 Sv from *Furue et al.* [2017]. The Lagranagian estimates are also weaker than *Feng* [2003] 3.4 Sv at 32°S (across a wider fixed distance offshore from 110°E). The closer agreement with *Furue et al.* [2017] is likely due to the closer alignment of the transport sections.

Since we are using a Lagrangian framework, these transports can be broken up in terms of their origin. The northern sources (orange/purple) account for 60-78% of the water found in the downstream flow of the Leeuwin Current. Along the downstream flow, the Indonesian Throughflow source (orange) is the largest, followed by the western offshore source (green) and then the northern offshore source (purple). Also along the downstream flow, aside from the poleward fluxes exiting sector 2, the western offshore fluxes (green) are 2-3 times bigger than the northern offshore fluxes (purple). The transports from the western offshore source are significant in magnitude, but water from this source is slightly deeper and less well mixed than the northern sources (Figure 1-7).

Whilst the mean flow of the Leeuwin Current is poleward, Figure 1-5 reveals significant exchange across the outside boundaries of the sectors, particularly from the western offshore water (purple). The net transports, however, are a small fraction compared to the eastward and westward flows, individually. This is indicative of the eddy rich region west of the mean Leeuwin Current pathway (see Figure 1-1e and [*Morrow et al.*, 2004; *Feng et al.*, 2005]). These transport results are interesting as observational data across these boundaries are quite sparse. As *Menezes et al.* [2014a] highlight 'the South Indian Ocean is historically poorly observed on a basin scale', this can be seen clearly in Figure 3.A.2 in [*Rhein et al.*, 2013]. Historically, most observations of transport have been taken perpendicular to the coast (e.g. [*Woo and Pattiaratchi*, 2008]).

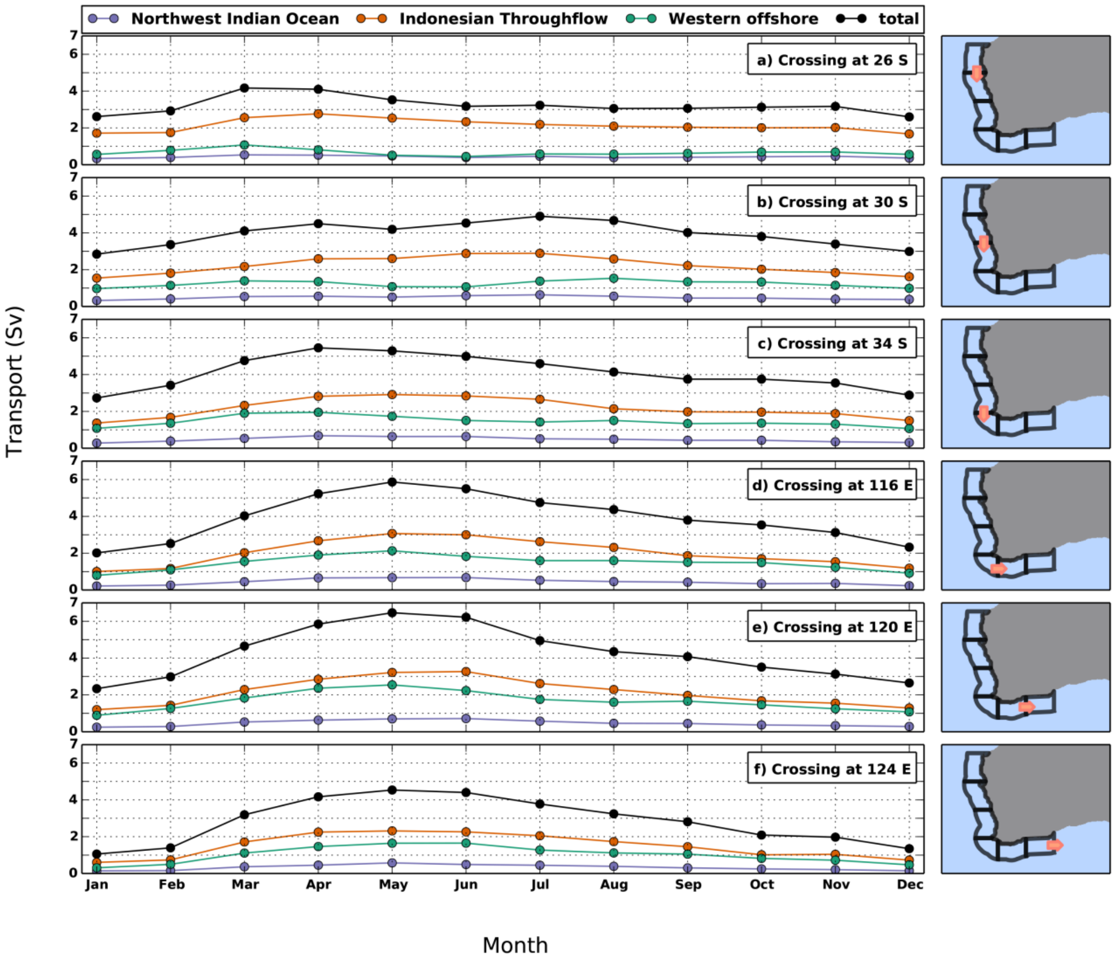

Figure 1-6. Mean seasonal contribution of Leeuwin Current sources along the Leeuwin Current's downstream flow, as located by the coral arrows in the maps on the right, for each row. Units are in Sv and the mean is taken over the years 1966-2003 and depth-integrating to 300m. Orange lines are particles originating from the Indonesian Throughflow region, purple lines are from the northern offshore section and green lines from the western offshore section. The black lines are the totals of the three coloured lines.

In section 1.2, it was shown that TROPAC01 captures the Leeuwin Current's seasonal cycle reasonably well. In 2004, *Ridgway and Condie* [2004] demonstrated how the seasonality of the Leeuwin Current affects sea surface temperatures. What has not been quantified is the contribution of the Leeuwin Current's different sources to the seasonal cycle, this is presented in Figure 1-6. Looking at the crossings at 26°S, 30°S and 34°S (Figure 1-6a-c) the peak transport occurs in different months. In the 26°S and 34°S crossings (Figure 1-6a, c) maximum transport occurs in March and April, respectively. The maximum at 30°S (Figure 1-6b) in July compares favourably with the maximum observed by *Smith et al.* [1991] at Dongara (29.5°S) in June. *Smith et al.* [1991] measured a geostrophic transport range of 2 Sv (February 1987) to more than 5 Sv (March, June and August 1987) at Dongara (29.5°S), whilst the summer transports in Figure 1-6b are higher, given the different sampling periods and location this appears to be in reasonable agreement with Figure 1-6b. In the Leeuwin Current extension we see that the peak transport occurs consistently in May. The strongest downstream flow month is in May, across 120°E (Figure 1-6e), which is due to the western offshore section contributing more (compare Figure 1-6d and Figure 1-6e). The largest seasonal variability is also at 120°E with an approximate 4 Sv difference between January and May. A number of papers on the Leeuwin Current have shown a seasonal southward propagating sea surface height signal for example Figure 5 in [*Ridgway and Godfrey*, 2015] and Figure 3 in [*Ridgway and Condie*, 2004]. In contrast, a similar signal is not found from the Lagrangian transport sections plotted in Figure 1-6. This somewhat surprising discrepancy may be a deficiency of the TROPAC01 simulation and is possibly caused by the sea surface height bias in the model Indian Ocean (around 15°S) discussed in section 1.2.1.

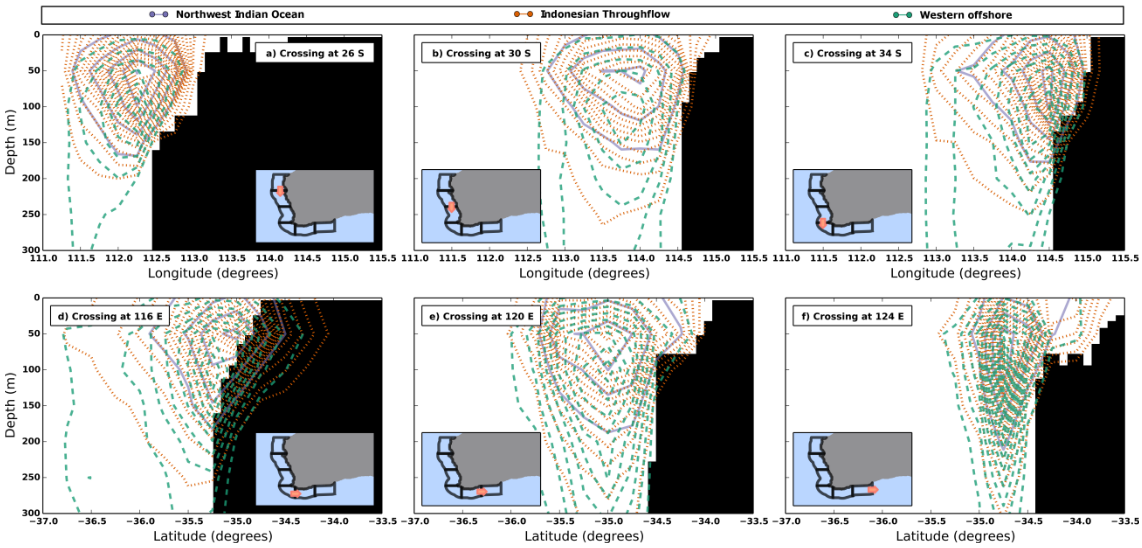

Figure 1-7. Depth-horizontal space transport sections along the Leeuwin Current's downstream flow. Plots (a)-(c) are in depth-longitude space, contoured transport is the water leaving sectors 1, 2 and 3, respectively. Similarly, plots (d)-(e) show transport due to water leaving sectors 4, 5 and 6 (respectively) but now in depth-latitude space. Contour intervals are 0.01 Sv where results have been binned to 0.25 degrees and 50 metres for horizontal and depth space, respectively. Orange lines are particles originating from the Indonesian Throughflow region, purple lines are from the northern offshore section and green lines from the western offshore section.

The relative contributions of each source and their seasonal cycle vary at each crossing. Across all crossings, the Indonesian Throughflow region source (orange) has the most seasonal variability, followed by the western offshore source (green). Since the northwest Indian Ocean's contribution is small and has little seasonality, it is the seasonality of the western offshore source and Indonesian Throughflow (including Torres Strait) that contribute the seasonality of the total. Indeed, the Indonesian Throughflow region contributes 66%, 56%, 53%, 51%, 50% and 53% of the total transport to the crossings in Figure 1-6a-f, respectively. As discussed in the introduction, the Lagrangian framework provides an opportunity to track the mixing of source waters along the Leeuwin Current's downstream pathway. Figure 1-7 is a series of depth-horizontal coordinate space plots for the sector crossings along the downstream flow for the mean over 1966-2003. Along the downstream flow (all plots in Figure 1-7) the core regions of the northern sources (orange and purple) are almost coincident. The western offshore source (green) has a core that is slightly deeper than the other two sources, so it follows that transport from the northern sources is closer to the shelf. The Indonesian Throughflow region (orange) contributes slightly more transport near the shelf than any other source. The location of the core at 30°S agrees well with the core location of the mooring at 29.5°S in [*Smith et al.*, 1991]. In sectors 4-6 (Figure 1-7d-f), along the Leeuwin Current extension, all three sources steadily shallow and the core regions continue to merge.

1.3.3 Particle Connectivity in the Indian Ocean and Great Australian Bight

A number of papers suggest that the Leeuwin Current is part of a continuous 5500 km coastal current system (e.g. [*Ridgway and Condie*, 2004; *Batteen and Miller*, 2009; *Ridgway and Godfrey*, 2015]). Whilst these studies have successfully tracked sea surface height/temperature anomalies around the Australian coast, it has not been clear how much water makes it directly from the source regions to the Great Australian Bight. Lagrangian tracking of water parcels provides an opportunity to quantify how these regions are connected by advection. To address this question, Figure 1-8 is different to Figure 1-5, Figure 1-6 and Figure 1-7; particles must meet strict criteria for their flux to be shown. particle trajectories in Figure 1-8 will therefore be labelled as *conditional pathways*. Specifically, the conditions applied are as follows: the particle's trajectory must enter by the first sector and recirculating particles are not counted. Thus, this Figure is a quantification of direct pathways through the Leeuwin Current region. The bold end of each edge indicates the direction of flux and inshore green edges indicate water that is travelling close to the coast having passed through all preceding inshore sector(s). For example, a flux of 0.7 Sv on the third green edge indicates transport from particles that have travelled directly through the first two sectors and are now crossing into the third sector. The flux itself is thus interpreted as the volume of water undertaking that pathway over the mean of the time series. Offshore red edges quantify trajectories that travelled through all green inshore upstream sector(s) and then exited the system via the red offshore edge. Finally, purple curved edges indicate trajectories that have travelled directly through the previous inshore sector(s) and then recirculated upstream. Units are in Sv and the mean is taken over the years 1966-2003 and depth-integrated to 300m.

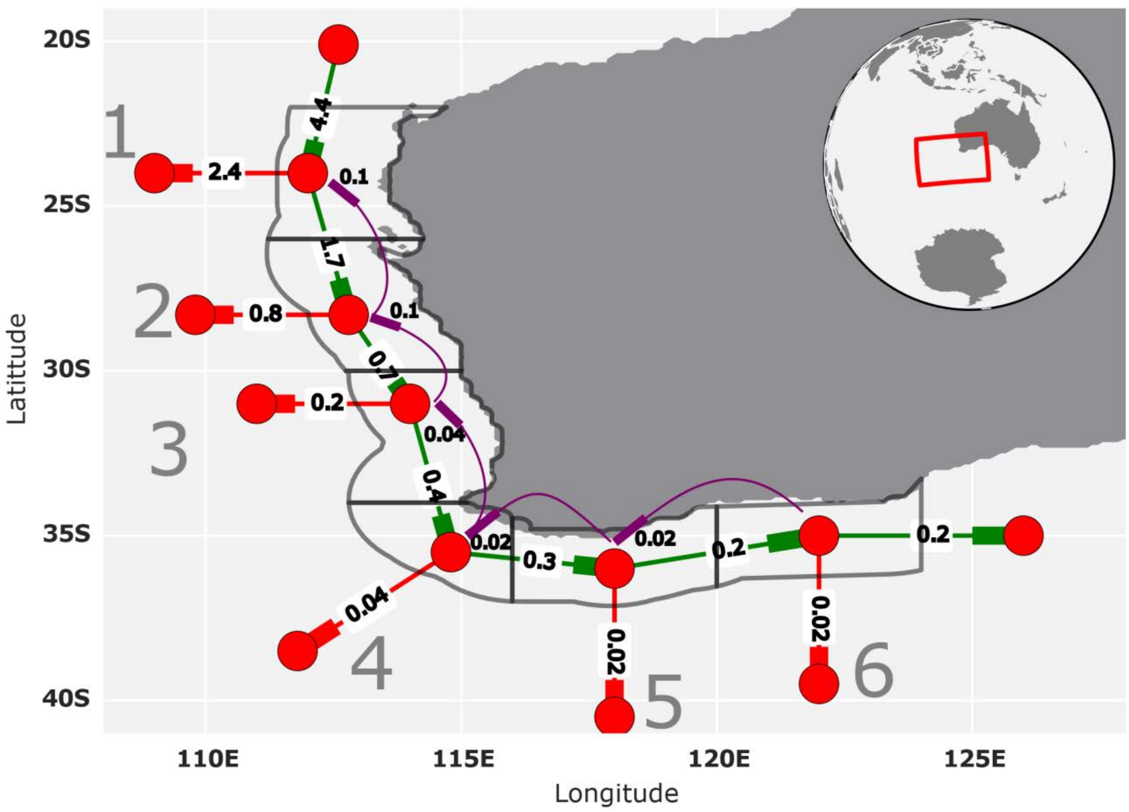

Figure 1-8. Quantification of direct pathways through the Leeuwin Current region. The bold end of each edge indicates direction of flux. Inshore green edges indicate water that is travelling close to the coast having passed through all preceding inshore sector(s). Offshore red edges quantify trajectories that travelled through all green inshore upstream sector(s) and then exited the system via the red offshore edge. Purple curved edges indicate trajectories that have travelled directly through the previous inshore sector(s) and then recirculated upstream. Units are in Sv and the mean is taken over the years 1966-2003 and depth-integrating to 300m.

This Figure addresses the second key objective of this paper, to quantify the amount of water that goes into the Leeuwin Current's extension compared to the amount of water that moves offshore into the Indian Ocean. Looking at the first sector, the flux going offshore (red edge) is larger than the flux going downstream (green edge). From the second sector particles heading offshore and downstream are approximately equal, and by the third sector more particles continue downstream than flow offshore. This partitioning then continues for the remainder of the downstream sectors. In other words, once a particle has gone through the first three sectors directly, it is likely to continue around Cape Leeuwin into the Great Australian Bight. Looking at the purple edges, it is clear that recirculating particles make up a very small fraction of the particle pathways. Sources have been combined in Figure 1-8 as there is little difference in the pathway taken when comparing source. The exception to this is the western offshore particles, Figure 1-11 shows that very few particles from the western offshore section follow the mean Leeuwin Current pathway. When compared to particles from the two northern sections, Figure 1-7 shows that western offshore particles are further offshore and so are less influenced by bathymetry. There are likely a number of processes that influence the pathway of the western offshore particles; *Menezes et al.* [2014b] discuss the dynamics that influence the flow patterns of the basin wide flows in detail.

Comparing these conditional pathways to the unrestricted particles in Figure 1-5, it is clear that the fluxes in the downstream sectors are much smaller when re-circulating particles are not allowed. In other words, Figure 1-8 shows that compared to the unrestricted pathways across the same sectors in Figure 1-5, very little water actually travels the full length of the Leeuwin Current and then around Cape Leeuwin into the Great Australian Bight directly.

1.4 Conclusions and Discussion

By tracking virtual Lagrangian particles in the eddy-resolving TROPAC01 model, we have quantified the fluxes of source waters and major pathways through the Leeuwin Current region. The Lagrangian framework has provided an insight into the connectivity between the tropical and subtropical sources of the Leeuwin Current and the Great Australian Bight. Indeed, if we take the particles from all the northern releases that have and have not entered any of the sectors and plot their proportion of transport (Figure 1-4), then we see that, within the model domain, the only way to reach the Great Australian Bight is via the Leeuwin Current.

Along the Leeuwin Current's pathway, we find water originating from the northern releases to be the most important, accounting for 60-78% of the transport; corroborating the traditional view that the Leeuwin Current is principally sourced from the Indonesian Throughflow, Torres Strait and the tropical Indian Ocean. Nevertheless, we also find large exchanges from all sources across the outside boundaries of the sectors; this includes water sourced from the interior Indian Ocean (the western offshore source). As the Leeuwin Current gains strength over winter (Figure 1-6), we see that water coming from the Indonesian Throughflow dominates the seasonal cycle.

Whilst thinking about the kinds of eddies that are resolved in a 1/10° model with output every five days we ask the following question. What portion of the fluxes in Figure 1-5 are attributable to water recirculating in large eddies? We address this by reproducing Figure 1-5 and only considering particles that transit directly through the sectors, in order from northwest to southeast, removing times a particle crosses a boundary more than once (Figure 1-8). Figure 1-8 indicates that significant amounts of the fluxes in Figure 1-5 are from recirculating particles or particles that did not start in sector 1 and flow directly through the sectors. In the sectors downstream of Cape Leeuwin, Figure 1-8 when compared to Figure 1-5 indicates that relatively little water travels directly from the start of the Leeuwin Current into the Great Australian Bight.

These differences between the non-conditional and conditional pathway analyses exemplify the non-laminar pathways in the Leeuwin Current region. This is important for two reasons. Firstly, it indicates the importance of eddies causing particles to recirculate. Secondly, it shows the relatively small number of particles that navigate the direct route along the Leeuwin Current and into the Leeuwin Current extension as described by *Ridgway and Condie* [2004]. This study is the first quantitative estimate of transport connecting the tropics and subtropics to the Great Australian Bight via the Leeuwin Current.

A number of studies have shown that the increase in Leeuwin Current transport in La Niña years can have a damaging effect on the temperature sensitive coastlines of western Australia [*Pearce and Feng, 2007; Wernberg et al., 2011; Thompson et al., 2015*]. Whilst beyond the scope of the present work, higher transports along the western Australian coast in La Niña years are expected, with more particles rounding Cape Leeuwin into the Great Australian Bight. Future work could extend this study by quantifying the change in pathways between El Niño and La Niña years. Building on recent work by *Ayers et al.* [2014], future work could regionally examine the biological implications of few tracked particles travelling the whole length of the Leeuwin Current into the Great Australian Bight. Recent work by *Wang et al.* [2015] has challenged the conventional view that Leeuwin Current strength is the single indicator of annual catch size of western rock lobster. *Wang et al.* [2015] found that cyclonic cold core eddies have a positive effect on the nutritional condition of the larvae, as a result, it would be interesting to track particle exchanges between the Leeuwin Current and Leeuwin Undercurrent.

The results in this paper are based on a single model and so are affected by biases in the forcing, sensitivity to a z-level coordinate system, the resolution of the model and the subsequent processes it can resolve. In section 1.2.1, biases in TROPAC01's sea surface height were discussed when compared to AVISO. As TROPAC01 tends to underestimate the energetic regions (Figure 1-1f) it is possible the results in this paper underestimate some of the eddy-driven fluxes. Thus, it is possible other eddy-resolving ocean model simulations using different forcing products would give slightly different results. Although the results in this paper are based purely on a model, they will assist future work in understanding the Leeuwin Current's role in regional climate and circulation in the region. Examples include: marine heatwaves [*Benthuysen et al.*, 2014b], connectivity in the region [*Coleman et al.*, 2013], the effects of climate change on Australia's boundary currents [*Sun et al.*, 2012] and understanding the dynamics of the Indian Ocean's anomalous eastward flows [*Menezes et al.*, 2014b].

1.5 Supplementary Figures

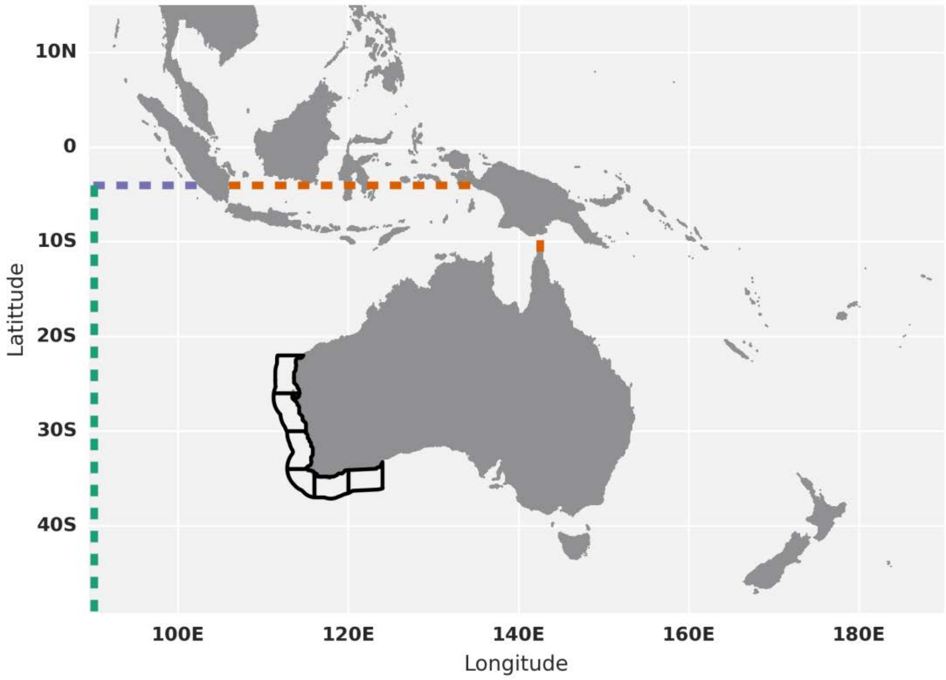

Figure 1-9. Map of Lagrangian virtual drifter release regions. Each colour represents a different release: orange is the Indonesian Throughflow region, purple is the northern offshore section and green is the western offshore section.

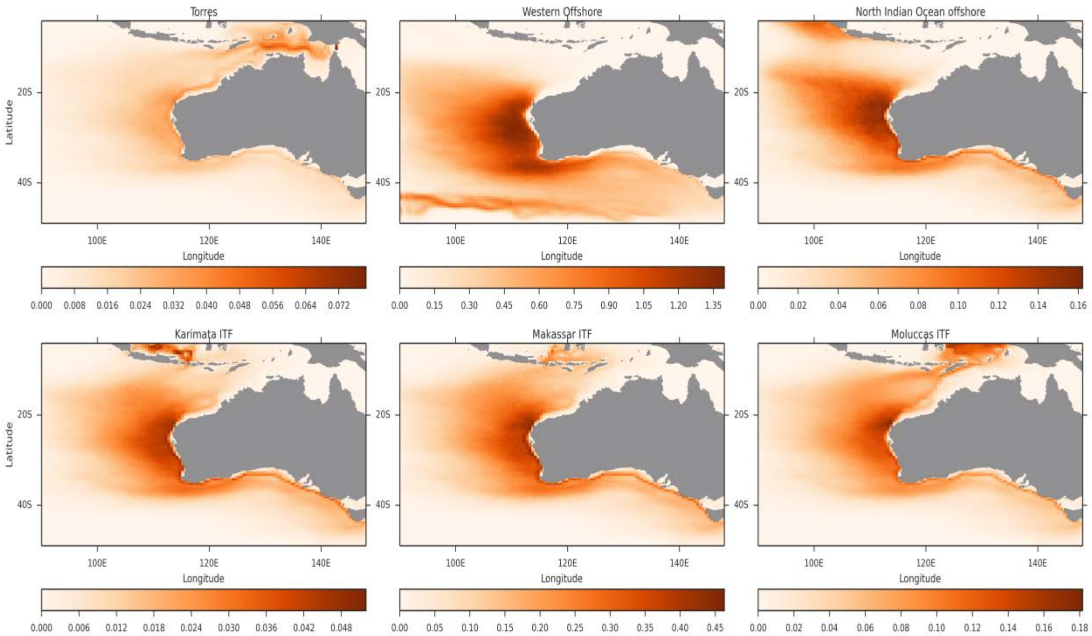

Figure 1-10. Maps of depth-integrated transport in Sverdrup from the different Leeuwin Current source waters, on a 0.5° × 0.5° degree grid. Only particles pathways entering a Leeuwin Current sector (see black lines Figure 1-9) are shown. Higher values indicate higher volumes of water from that source entering those grid cells at any depth and at any point in the experiment.

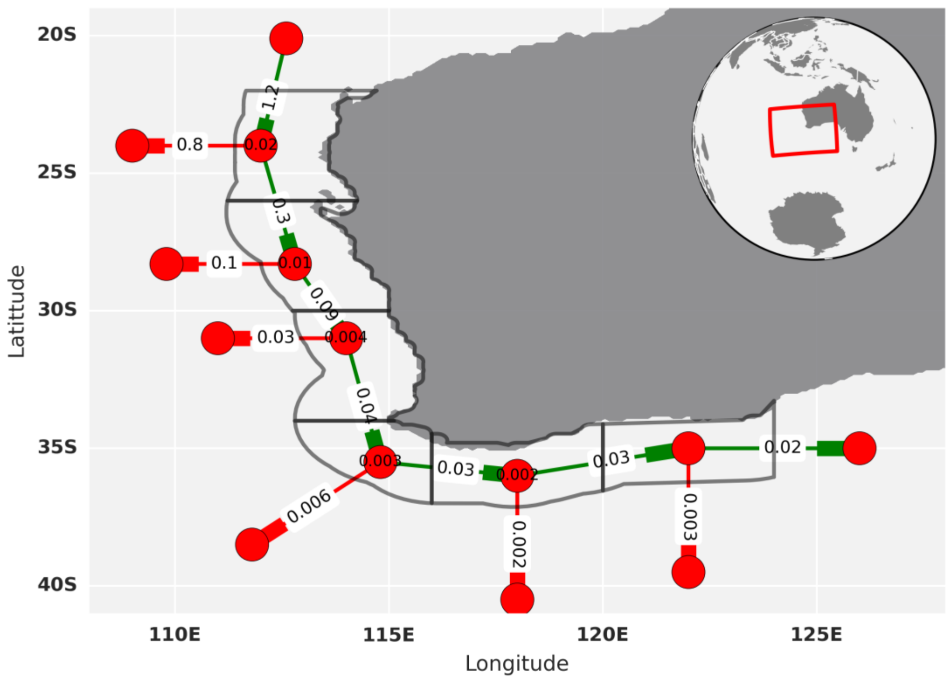

Figure 1-11. Same as in Figure 1-8 but for particles coming from the western offshore section only. Bold end of each edge indicates direction of flux. Inshore green edges

indicate water that is travelling close to the coast having passed through all preceding inshore sector(s). Offshore red edges quantify trajectories that travelled through all green inshore upstream sector(s) and then exited the system via the red offshore edge. Fluxes on nodes indicate trajectories that have travelled directly through the inshore edges to the closest downstream sector to the node, the particle has then recirculated back into the node. Units are in Sv and the mean is taken over the years 1966-2003 and depth-integrating to 300m.

Part 2. The role of New Zealand in the Tasman Sea circulation and separation of the East Australian Current.

Part 2 contains a reformatted version of the published manuscript (Journal of Geophysical Research: Oceans):

Bull, C. Y. S., Kiss, A. E., van Sebille, E., Jourdain, N. C., & England, M. H. (2018). The role of the New Zealand plateau in the Tasman Sea circulation and separation of the East Australian Current, *Journal of Geophysical Research: Oceans*, 123. https://doi.org/10.1002/2017JC013412.

Abstract

The East Australian Current (EAC) plays a major role in regional climate, circulation and ecosystems, but predicting future changes is hampered by limited understanding of the factors controlling EAC separation. Whilst there has been speculation that the presence of New Zealand may be important for the EAC separation, the prevailing view is that the time-mean partial separation is set by the ocean's response to gradients in the wind-stress curl. This study focuses on the role of New Zealand, and the associated adjacent bathymetry, in the partial separation of the EAC and ocean circulation in the Tasman Sea. Here, utilising an eddy-permitting ocean model (NEMO), we find that the complete removal of the New Zealand plateau leads to a smaller fraction of EAC transport heading east and more heading south, with the mean separation latitude shifting >100km southward. To examine the underlying dynamics, we remove New Zealand with two linear models: the Sverdrup/Godfrey Island Rule [Sverdrup, 1947; Godfrey, 1989] and NEMO in linear mode. We find that linear processes and deep bathymetry play a major role in the mean Tasman Front position whereas nonlinear processes are crucial for the extent of the EAC retroflection. Contrary to past work, we find that meridional gradients in the basin-wide wind stress curl are not the sole factor determining the latitude of EAC separation. We suggest that the Tasman Front location is set by either the maximum meridional gradient in the wind stress curl or the northern tip of New Zealand, whichever is furthest north.

2.1 Introduction

Subtropical western boundary current (WBC) regions are warming two to three times faster than the globally averaged surface ocean warming rate [*Wu et al.*, 2012; *Yang et al.*, 2016]. The intensification and poleward shift in separation of WBCs is thus an important problem to study, but our current understanding is hampered by limited historical measurements as well as a lack of regionally relevant modelling studies addressing a range of factors thought to influence separation. Global ocean climate modellers are yet to find a single set of modelling parameters (e.g. bathymetry, model resolution, sidewall boundary condition, sub-grid scale parameterisations, vertical grid type et cetera) that ensure correct separation of all the major western boundary currents [*Chassignet and Marshall*, 2008]. Historically, studies of the Gulf Stream separation occupy much of the literature and numerous physical theories exist. As described in the Preface, the starting point is the linear theories of [*Sverdrup*, 1947; *Stommel*, 1948; *Munk*, 1950] suggesting that separation occurs in response to a change in sign of the wind stress curl. More sophisticated mechanisms (upon inclusion of the non-linear terms) are: potential vorticity crisis, regions of adverse pressure gradient, collision with another western boundary current and outcropping of isopycnals and overshooting from a cape (see [*Chassignet and Marshall*, 2008; *Kiss*, 2010a; *Schoonover et al.*, 2016] and references therein).

In the Australian context, the poleward shift in the westerlies [*Swart and Fyfe*, 2012] – driven by both ozone depletion and greenhouse gas increases – is thought to be driving a change in the South Pacific wind stress curl field leading to an enhancement or ‘spin up’ of the EAC extension [*Cai et al.*, 2005; *Ridgway*, 2007a; *Ridgway et al.*, 2008; *Oliver and Holbrook*, 2014; *Sloyan and O’Kane*, 2015; *Feng et al.*, 2016; *Roemmich et al.*, 2016]. It is an open question as to whether the entire EAC spins up, or the EAC extension alone [*Ridgway*, 2007a; *Cetina-Heredia et al.*, 2014; *Sloyan and O'Kane*, 2015; *Feng et al.*, 2016]. A widely-held explanation for the latitude of separation (based on the Sverdrup [1947] balance) is that the partial separation of the East Australian Current (EAC) is determined by the steepest meridional gradient in the Pacific basin zonal-averaged wind stress curl [Tilburg et al., 2001; Bostock et al., 2006; Oliver and Holbrook, 2014]. Similar linear assumptions are used in global studies; for example Wu et al. [2012] use the mid-latitude zero wind stress curl line to explain shifts in the boundary between the subtropical and subpolar gyres. Despite well-known issues in using linear theory in western boundary current regions (e.g. vorticity advection, see [Pedlosky, 1996; Gray and Riser, 2014; Thomas et al., 2014]), climate change attribution studies often resort to linear dynamics (e.g. [Cai, 2006; Hill et al., 2011; Oliver and Holbrook, 2014; Sen Gupta et al., 2016]) when relating the spin-up of the EAC to anthropogenic changes in the South Pacific wind stress curl.

The EAC system is the most energetic circulation feature in the south western Pacific Ocean and is a primary conduit for poleward heat transport from the tropics to midlatitudes [Ridgway and Dunn, 2003; Hu et al., 2015; Sloyan et al., 2016]. The EAC system (summarised in Figure 2-1e) consists of a relatively steady upstream current (22.1±7.5 Sv at 27°S [Sloyan et al., 2016]), which partially bifurcates at 30-34°S [Cetina-Heredia et al., 2014]. The branch that flows east forms the Tasman Front [Sutton and Bowen, 2014] and contributes to New Zealand's boundary currents, including the East Auckland Current and East Cape Current [Chiswell et al., 2015]. In the process of separation, the EAC sheds an anti-cyclonic eddy (average radius 95 km [Everett et al., 2012]) every ~100 days [Mata et al., 2006]. Once the eddy detaches from the main current, the EAC then retracts northward [Mata et al., 2006] and it is this non-linear eddy dominated asymmetric oscillation that defines the time-mean partial separation latitude. The shed eddies then move south-westward in a procession that characterises the EAC extension [Everett et al., 2012]. A small portion of these eddies then continue around Tasmania [Pilo et al., 2015], at times making it as far westward as the Indian Ocean; the latter pathway is known as the Tasman Leakage [van Sebille et al., 2012]. Via Tasman Leakage the EAC participates in the Southern Hemisphere supergyre circulation [Ridgway and Dunn, 2007; Speich et al., 2007]. Hill et al. [2011] found that the EAC extension and Tasman Front transport are anti-correlated in response to basin-scale winds with a time lag of ~3 years. Using observations and models, several other studies [Oliver and Holbrook, 2014; Chiswell and Sutton, 2015; Hu et al., 2015; Sloyan and O'Kane, 2015] have made similar findings; however the underlying roles of non-linear dynamics and bathymetry warrant further investigation.

Previous studies have suggested New Zealand may be important for the EAC's separation latitude and Tasman Sea circulation [*Warren*, 1970; *Heath*, 1985]. Prior to direct satellite observations, Warren [1970] suggested that mass balance requires the existence of a Tasman Front to satisfy Sverdrup [1947] transport constraints. Although *Warren* [1970] did not state it in these terms, subsequent authors (e.g. *Godfrey et al.* [1980] and *Tilburg et al.* [2001]) portrayed *Warren* [1970] as arguing that New Zealand has this putative effect by blocking westward-propagating Rossby waves. *Godfrey et al.* [1980] left open the possibility that New Zealand's blocking of Rossby waves determines the general region in which EAC separation can occur, but argued that the specific location of separation is controlled locally by coastline shape (particularly Sugarloaf Point). *Tilburg et al.* [2001] investigated the Tasman Sea circulation in a hierarchy of models of increasing realism, but studied the removal of New Zealand only in the simplest of these: a linear, 1.5-layer, Sverdrup-Munk [*Sverdrup*, 1947; *Munk*, 1950] model. In this idealized model the removal of New Zealand did not affect the separation latitude, and the authors invoked Sverdrup theory to suggest that the partial separation of the

EAC can be explained by a steep meridional gradient at that latitude in the zonally-integrated *Hellerman and Rosenstein* [1983] wind stress curl dataset they used. However, linear models have been shown to lack skill in predicting changes in the EAC separation latitude [*Oliver and Holbrook*, 2014] and circulation changes in the Tasman Sea [*Ridgway and Godfrey*, 1994; *Couvelard et al.*, 2008; *Sen Gupta et al.*, 2016].

Our primary focus here is to investigate the role of New Zealand, and the associated adjacent bathymetry, in the partial separation of the EAC and circulation of the Tasman Sea. We aim to improve our understanding of the underlying dynamics of the EAC and other aspects of Tasman Sea circulation. We improve on Tilburg et al. [2001] by utilising a full primitive equation eddy-permitting model that includes non-linear dynamics and bottom topography. By removing New Zealand whilst retaining virtually the same atmospheric forcing, we are able to diagnose the impact of the bathymetry around New Zealand, without confounding changes in the wind stress curl. Using NEMO, we present a suite of experiments with modified bathymetry in the Tasman Sea (section 2.2.2) to investigate the relationship between the EAC separation latitude and New Zealand (section 2.4). Contrary to Tilburg et al. [2001], we find that bottom topography and non-linear effects are important for the EAC separation location.

2.2 Ocean model and experimental design

2.2.1 The ocean model and its configuration

We use version 3.4 of the Nucleus for European Modelling of Ocean (NEMO) model [*Madec*, 2012]. NEMO solves the incompressible, Boussinesq, hydrostatic, primitive equations on a z-coordinate C-grid with a filtered free surface and free-slip lateral boundaries. We use 75 vertical levels, with 24 levels in the first 100m and 22 levels between 100-1000m to realistically represent coastlines and continental shelves. Bathymetry is from ETOPO1 [*Amante and Eakins*, 2009] and is represented by partial cells. NEMO is run with a prognostic turbulent kinetic energy (TKE) scheme for vertical mixing. We use spatially varying lateral eddy coefficients (according to local mesh size) with Laplacian iso-neutral tracer diffusion and biharmonic lateral viscosity.

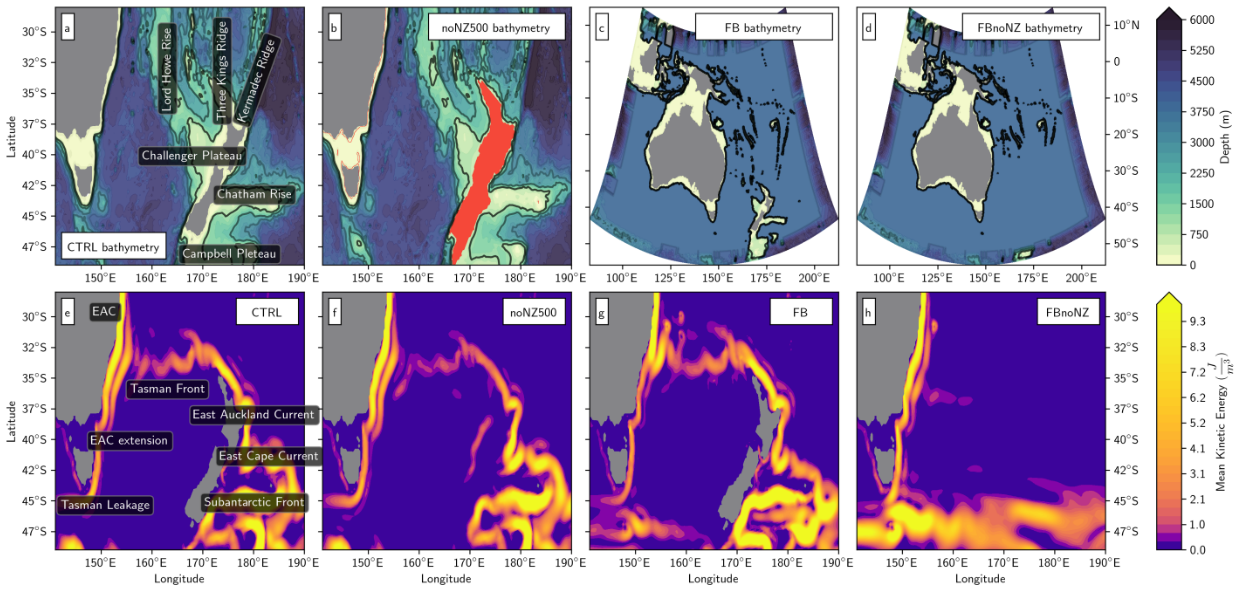

Figure 2-1. a-d) bathymetry of the perturbed bathymetry experiments, solid contours are at: 1km, 2km, 3km and 4km. b) has an additional red filled contour to indicate 500m isobath around New Zealand which was excavated. Regional NEMO modelling domain pictured in c-d. e-h) volume-averaged MKE down to 1945m.

The model domain is pictured in Figure 2-1c-d. The horizontal grid is curvilinear and eddy-permitting (nominally 1/4°; meridional resolution is 24.5 km and zonal resolution is 19.5 - 24.5 km depending on longitude and latitude). This regional simulation is forced at the open ocean boundaries by temperature, salinity and velocity with 5-day means from a global NEMO ocean simulation run at 1/4° resolution with 75 vertical levels (namely, ORCA025-L75-MJM95, provided by the DRAKKAR/MyOcean group [Barnier et al., 2011]). The initial conditions for ocean temperature and salinity are taken from *Levitus et al.* [1998] with an ocean at rest. River input is prescribed from monthly climatology [Dai and Trenberth, 2002]. The regional simulation and ORCA025-L75-MJM95 are both forced at the surface by 10m winds, 2m air temperature, humidity (every 3 hours), precipitation, long wave, and short wave radiation (every day) from the ERA-interim atmospheric reanalysis [*Dee et al.*, 2011] between 1989-2009 through the CORE bulk formulae [*Large and Yeager*, 2004].

2.2.2 Experimental design

Eight experiments are used to investigate the relationship between the EAC separation latitude and the Tasman Sea bathymetry (Figure 2-1a-d):

1. CTRL: realistic bathymetry (i.e. interpolated from ETOPO1);
2. noNZ500: as for CTRL, but New Zealand levelled to 500m deep (i.e. all bathymetry within the 500m isobath around NZ, and NZ itself, is set to an ocean depth of 500m – shaded red in Figure 2-1b);
3. FB ("flat bottom"): bathymetry >1000m deep is set to 4000m throughout the domain (apart from near the open boundaries, where bathymetry is linearly interpolated from 4000m to ETOPO1 over ~7°). Bathymetry shallower than 1000m matches CTRL (note that this includes much of the Campbell Plateau);
4. FBnoNZ: as for FB, but with New Zealand, the Campbell Plateau within the domain and the islands and seamounts between New Zealand and New Caledonia levelled to 4000m (retaining New Caledonia as in FB). A small part of Campbell Plateau is retained within the 7° smoothing zone against the southern boundary.

Experiments 5-8 are additional NEMO experiments (CTRL-L, noNZ500-L, FB-L, FBnoNZ-L) with the same series of bathymetry changes and forcing as in experiments 1-4, but with non-linear advection terms omitted from the momentum equations; advection is retained in the tracer equations. The southern boundary of the regional domain cuts through Campbell Plateau, so this is only partly removed in experiments 4 and 8.

The CTRL experiment provides a reference of the model's most realistic circulation. The noNZ500 simulation shows the impact of the near-surface New Zealand landmass. The FB and FBnoNZ experiments are designed to be analysed as a set. The

FB experiment is a new control simulation retaining the New Zealand plateau alone, for comparison with its removal in FBnoNZ. To investigate the linear dynamics of the circulation changes due to the removal of New Zealand in the simplest possible scenario, we calculate the steady-state Sverdrup / Godfrey Island Rule [Sverdrup, 1947; Godfrey, 1989] stream function (Figure 2-7a-b) with and without New Zealand, utilising the time-mean ORCA025-L75-MJM95 (global NEMO) wind stress and curl fields. Linear experiments 5-8 extend the Sverdrup balance calculation by including most of the features of experiments 1-4 such as complex bathymetry/continental shelves, stratification (outcropping) and forcing variability.

For the grid points where submarine topography has become part of the ocean domain, Levitus et al. [1998] initial conditions of temperature and salinity are interpolated from the horizontally closest values. Similar island-removing studies by *Tilburg et al.* [2001] and *Penven et al.* [2006] do not specify what is done with the atmospheric fluxes over the removed island. In this study, the atmospheric fluxes over the area where New Zealand used to be are the same value as the closest ocean grid point. This removes the effect of New Zealand's orography on local winds and the potential for unrealistic heat fluxes over the ocean grid points coinciding with the New Zealand landmass. We did not attempt to eliminate the effect of NZ on wind stress and other fluxes at the surrounding ocean points. Most importantly, this methodology results in an integrated time-mean wind stress curl that is not significantly different across the experiments, enabling us to test the hypothesis that the partial separation of the EAC is set solely by the meridional gradients in the wind stress curl.

Model outputs and subsequent analyses are based on daily averages. Similar to other boundary current regional configurations (e.g. [*Renault et al.*, 2016b]), all eight

NEMO experiments are spun-up for five years, and all results in this study use model output between January 1, 1994 and December 31, 2009 (i.e., after the 5-year spin-up phase of January 1, 1989 – December 31, 1993).

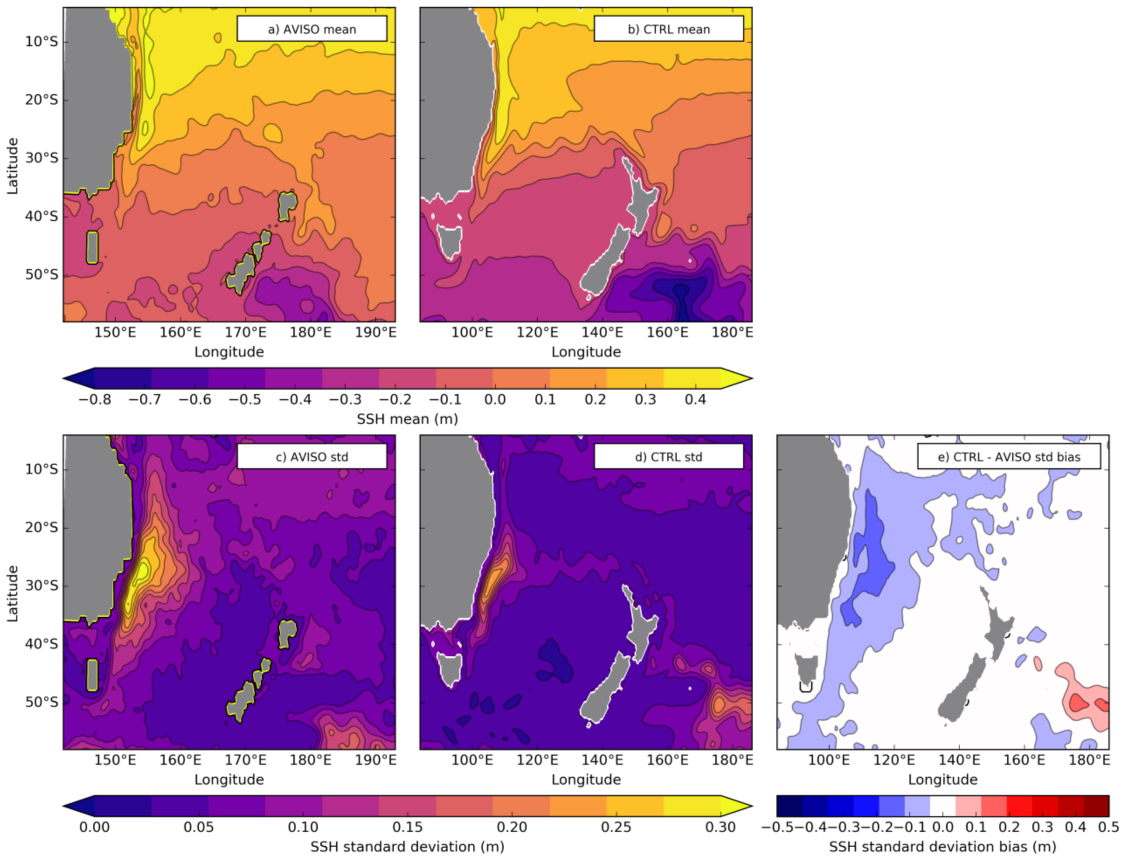

Figure 2-2. Comparison of NEMO (CTRL) and AVISO sea surface height between 1994-2009 where a-b) mean and c-e) standard deviation. The time-mean of sea surface height is calculated with the temporal and spatial average in the Tasman Sea region removed to emphasise the difference in time-mean gradients between CTRL and AVISO.

2.3 Model evaluation

Figure 2-2 compares the CTRL simulation sea surface height (SSH) to satellite altimetry observations (AVISO) over the years 1994-2009 for which the two products overlap. The time-mean gradients of SSH are generally in good agreement; the EAC and East Auckland Current are clearly visible, and importantly the modelled SSH gradients in the EAC have similar location and structure to the observations. Prior to separation, the upstream EAC has a range of observed and modelled transports from past studies; observed estimates include 27.4 Sv [Ridgway and Godfrey, 1994] and 25.8 Sv [derived from CARS; Ridgway et al., 2002]. Modelling estimates of EAC transport range between 20.4 Sv and 30 Sv [Wang et al., 2013; Oliver and Holbrook, 2014; Ypma et al., 2016]. In our study, the modelled CTRL upstream EAC transport to 1945 m across 154°E-156°E at 28°S is 24.3 Sv (Figure 2-3), and therefore within both modelled and observed estimates of EAC transport, and also consistent with the 22.1±7.5 Sv directly observed transport at 27°S [Sloyan et al. 2016].

Nonetheless, biases do exist, in the model simulation. For example, there are sharper SSH gradients in CTRL both on the south-eastern side of New Zealand and across the Tasman Sea in the Tasman Front. The bias across the Tasman Sea results in a more focused eastward flow and is typical of other modelling studies in the region [*Oliver and Holbrook*, 2014; *Ypma et al.*, 2016]. The Tasman Front's observed transport is highly variable and at times westward [*Sutton and Bowen*, 2014]. Observed in different time periods, across different sections, mean transport estimates vary: 7.6-8.5 Sv [*Stanton*, 1979], 12-13 Sv [*Stanton*, 1981], 12.9 Sv [*Ridgway and Dunn*, 2003] and the first direct measurements by *Sutton and Bowen* [2014] of 7.8 Sv. The CTRL experiment Tasman Sea mean outflow of 7.6 Sv (Figure 2-3 section GD) is within the range of observed transports.

The variability of sea surface height in CTRL is also in good agreement with AVISO in many areas but underestimated in the EAC (Figure 2-2c-e). This is typical of 1/4° eddy-permitting resolution models (e.g. [*Ypma et al.*, 2016]). The standard deviation bias (Figure 2-2e) south-east of New Zealand may be related to the documented semi-permanent eddies in the region (see Figure 13 of *Chiswell and Sutton*

[2015], who note that some altimetry datasets do not resolve these features) and/or the strong fronts associated with the confluence of subtropical and subantarctic waters in the region [*Fernandez et al.*, 2014].

2.4 Results

The importance of New Zealand for the presence and location of the Tasman Front is revealed in Figure 2-1e-h by the depth-averaged time-mean kinetic energy field (MKE), defined by MKE(x,y) = $\frac{\rho_0}{2D}\int_{-D}^{0}(\bar{u}^2(x,y,z)+\bar{v}^2(x,y,z))\,dz$, where $\bar{u}$ and $\bar{v}$ are the time-mean horizontal velocity components, $\rho_0 = 1035\ kg\ m^{-3}$, and D is the depth of the seafloor or 1945m, whichever is shallower. Comparing FB and FBnoNZ in Figure 2-1g and h, the latter has no East Auckland Current/East Cape Current and the partial separation of the EAC has shifted south (barely visible, clearer in Figure 2-7j). Specifically, FBnoNZ has a much weaker, more zonal Tasman Front located further south, as well as enhanced MKE in the EAC extension. The reduced eastward flow out of the Tasman Sea suggested by Figure 2-1 is confirmed by the transports shown in Figure 2-3. The eastward transport north of New Zealand (section GD) decreases from 8.8 Sv to -1.2 Sv when New Zealand is completely removed; FBnoNZ has zero net transport across sections GD+GP. Comparing the EAC extension (JK) with the East Cape Current (LM) sections in Figure 2-3, from FB to FBnoNZ, the EAC extension (JK) shows an increase of 5.4 Sv which is approximately balanced by a relative reduction of 5.3 Sv in LM. Finally, FBnoNZ shows a large northward shift in the Subantarctic Front (indicated in Figure 2-1e) south of Australia. This northward shift is associated with the partial removal of the Campbell Plateau (compare with noNZ500) and almost completely blocks Tasman leakage, which drops from 14.2 Sv to 1.5 Sv (section IH).

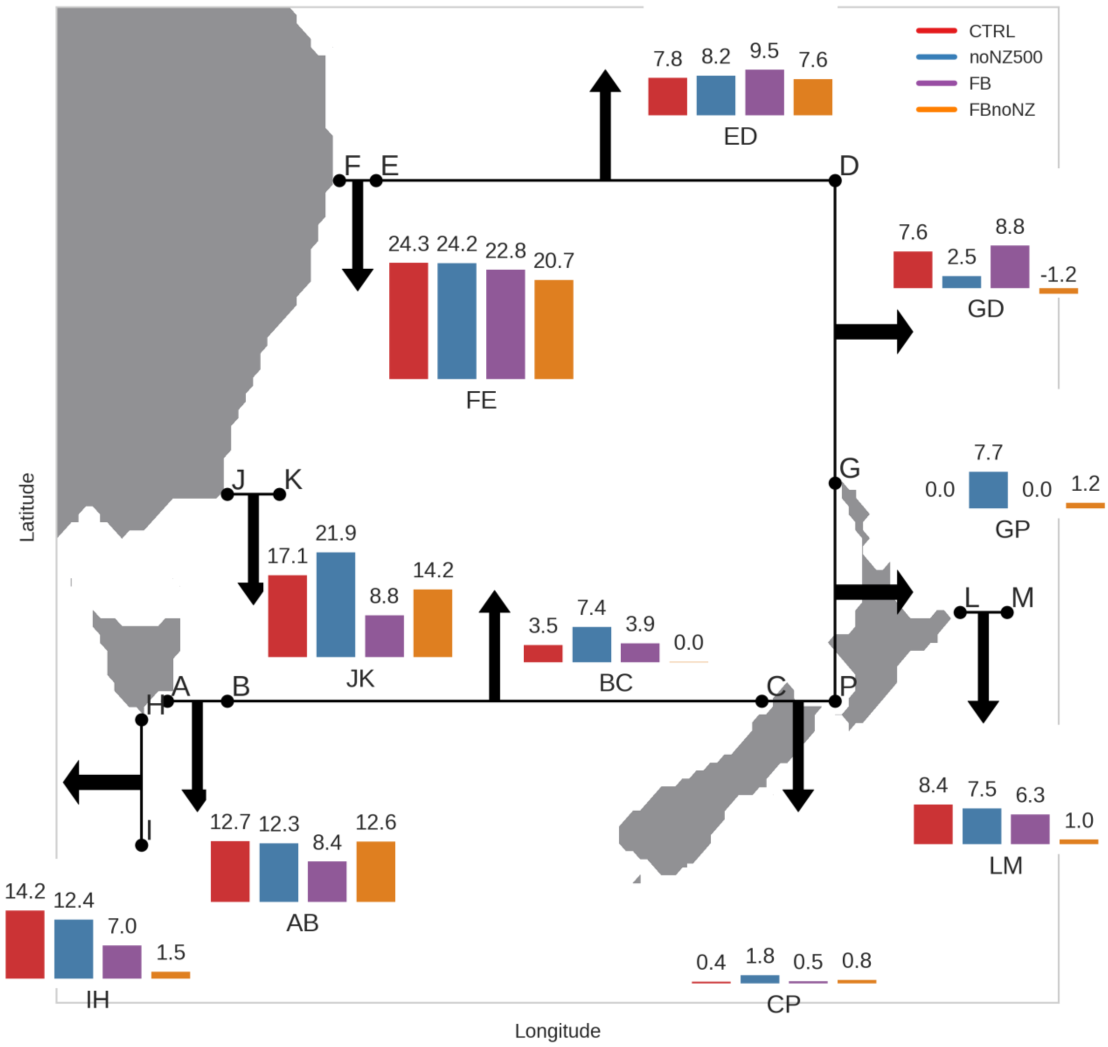

Figure 2-3. Schematic comparison of depth-integrated transport (Sv) to 1945m. Section end points are similar to Oliver and Holbrook [2014] but sections are aligned with the curvilinear model grid (not strictly zonal/meridional); transport is calculated using zonal velocities for IH, DP and meridional velocities for FD, JK, LM, AP. Section end points are: A (148.2°E 42.6°S), B (150.8°E 42.6°S), C (172.5°E 40.6°S), D (171.3°E 25.8°S), E (155.6°E 27.6°S), F (153.6°E 27.8°S), G (173.6°E 34.9°S), H (146.9°E 43.4°S), I (146.9°E 45.8°S), J (150.1°E 37.1°S), K (151.7°E 37.1°S), L(178.1°E 37.5°S) and M(179.9°E 36.8°S). Bar scales are relative to each section.

Compared to CTRL, experiments FB and noNZ500 show much smaller differences than FBnoNZ in Figure 2-1. Levelling all bathymetry below 1km to 4km (FB) leads to a diminished EAC extension and a stronger re-circulation in the separation region. This is consistent with decreased transports in the EAC extension (JK and AB), increased transport offshore flowing north at ED and increased Tasman Front transport (GD; Figure 2-3). In contrast, levelling the New Zealand landmass to 500m (noNZ500) leads to a substantial transport increase across BC (3.9 Sv) in the southern Tasman Sea; this is caused by an enhanced northward flow on the western side of the levelled New Zealand landmass (Figure 2-7f). Whilst Figure 2-1f suggests noNZ500 has a slightly weaker Tasman Front than CTRL, Figure 2-3 reveals that the overall Tasman Sea eastward transport (GD+GP) is higher and concentrated further south across GP, and this is compensated by a weaker net southward Tasman Sea outflow (AP) of 6.7 Sv for noNZ500 as compared to 9.6 Sv in the CTRL simulation.

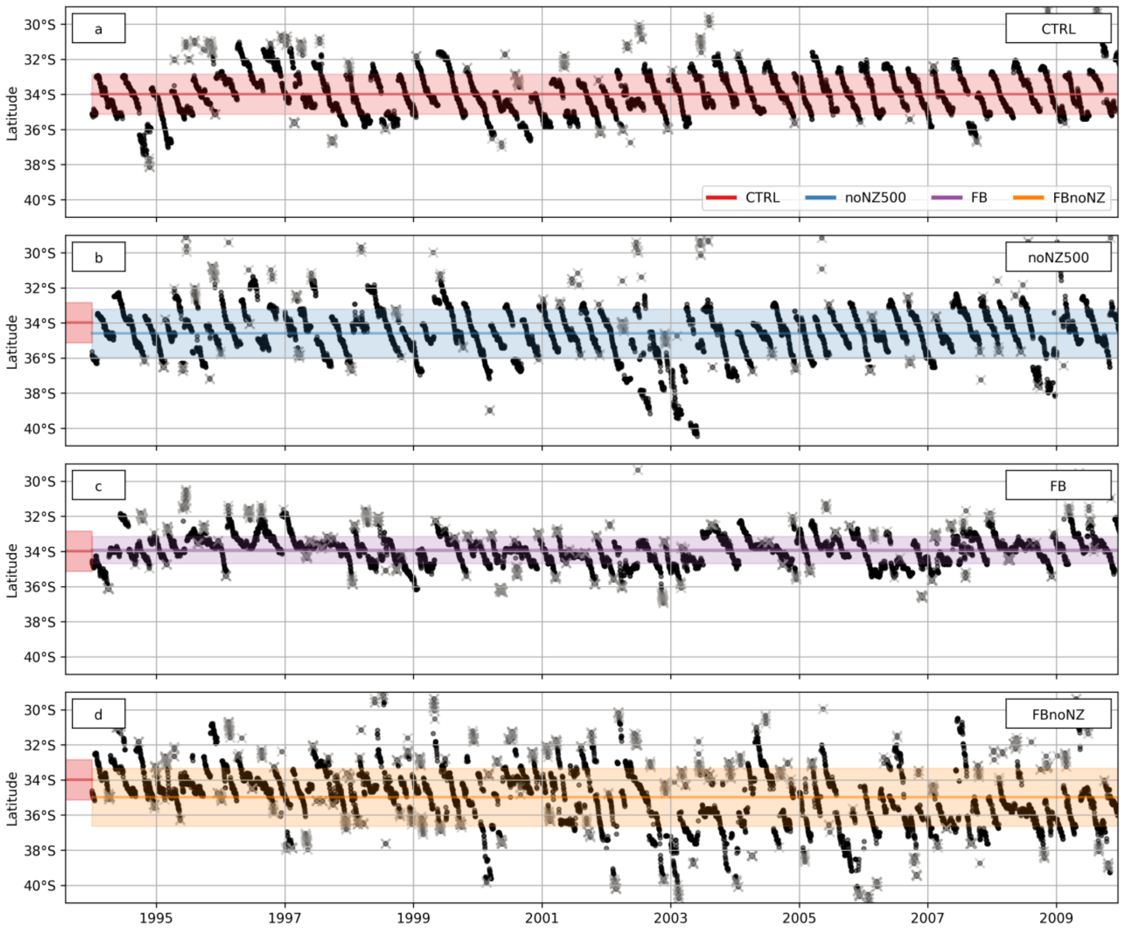

Figure 2-4. a-d) Separation latitude time series comparison. Black dots are detected separation latitude (gray crosses are false-positive outputs by the separation latitude algorithm). Thick solid line indicates the mean of each experiment and the shaded region indicates one standard deviation, CTRL mean and standard deviation are on rows 2-4 for comparison.

The separation latitude of the EAC shown in Figure 2-4a-d is calculated from each daily average snapshot. The separation latitude is found following the method described by Cetina-Heredia et al. [2014] and Ypma et al. [2016], namely, we first find the upstream core of the EAC, defined here as the maximum southward geostrophic surface velocity at 28°S. The SSH contour at the location of the maximum velocity is then followed south and the first location at which the contour turns more than 30° east of south is recorded as the separation latitude. In summary, the time-series describes where a representative EAC SSH contour first separates from the coast. Each diagonal line segment in the CTRL simulation (Figure 2-4a) represents the growth of the EAC retroflection south, then at ~35-37°S the detected EAC separation latitude retracts abruptly north to ~33°S (where the black line segment has a discontinuity). This occurs when an eddy detaches from the EAC, producing a closed SSH contour so that the detected separation latitude jumps from the southern to the northern edge of the eddy as it is shed. Therefore the mean of the separation latitude (thick red line) is not the mean latitude at which eddies are shed (~33°S). Consistent with the flat-bottom experiment of *Tilburg et al.* [2001], experiment FB's mean separation is essentially unchanged (northward shift of 0.1°, Figure 2-4c), however the standard deviation is reduced by 32%. Removal of New Zealand causes a 0.6° southward shift of the mean separation latitude in noNZ500 relative to CTRL (Figure 2-4a,b); for comparison, *Tilburg et al.* [2001] have a negligible shift in EAC separation on removal of New Zealand in their linear 1.5 layer experiments with an active layer thickness of 250m. A much stronger contrast to *Tilburg et al.* [2001] is seen in the difference between FB and FBnoNZ (Figure 2-4c,d) which shows that the removal of New Zealand shifts the mean separation latitude 1.1° further south, and also produces a much less organised pattern of eddy shedding in both timing and latitude, doubling the standard deviation of the separation latitude from 0.8° to 1.6°. Other factors influencing the regularity of EAC eddy shedding are re-visited in Section 3.4.3. Since the separation latitude has high variability, the standard error of the mean is used to check the statistical significance of these changes The standard error of the mean is defined as $\sigma/\sqrt{n}$ where σ is the standard deviation and n is the number of independent samples. The first minimum in the separation latitude autocorrelation across all experiments occurs within 120 days. Taking 120 days as a conservative interval for independent samples, yields a maximum standard error in the mean EAC separation latitude of 0.1° and 0.2° for FB and FBnoNZ, respectively. The 1.1° shift in the mean between FB and FBnoNZ is therefore statistically significant, despite being within the typical range of an individual eddy-shedding cycle. The 1.1° shift in the mean is also larger than those reported in both recent (1980–2010) and future climate simulations (*Cetina-Heredia et al.* [2014] and *Oliver and Holbrook* [2014], respectively).

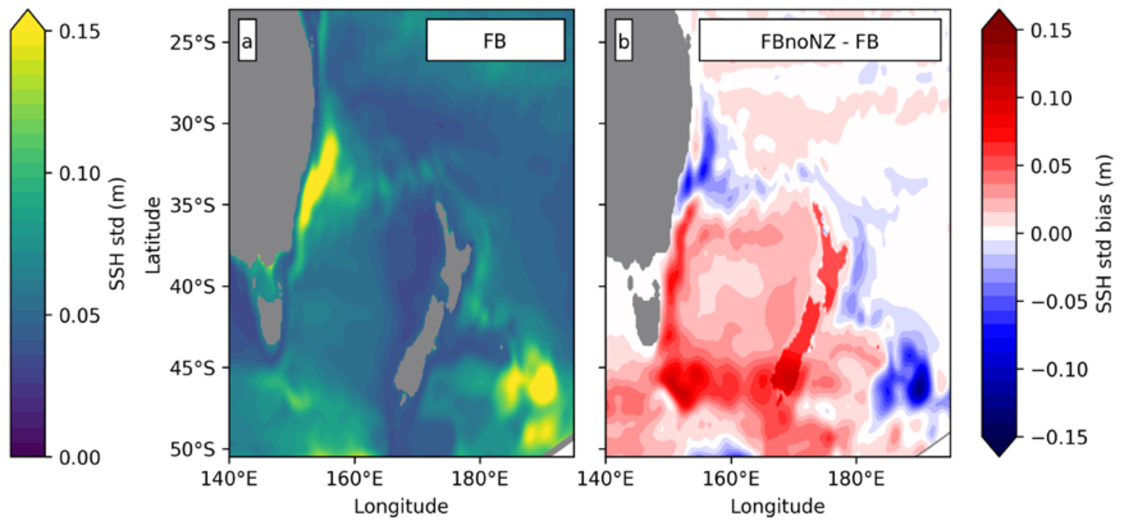

Figure 2-5. a) Standard deviation of sea surface height (m) for FB. b) Sea surface height standard deviation difference (m) between FB and FBnoNZ. Red (blue) indicates increased (decreased) variability in FBnonZ.

To summarise, when New Zealand is completely removed (FBnoNZ), the EAC's eddies travel a greater distance south before separating from the main current, but the EAC retracts to a similar latitude after eddy separation, giving a larger range of latitudes. Thus the shift in MKE (Figure 2-1g,h) between FB and FBnoNZ is due to the EAC separation transiently reaching farther south in FBnoNZ (Figure 2-4). This result, along with the change in Tasman Front position as shown in MKE in Figure 2-1, forms the evidence for the main finding of this paper: that bathymetric features around New Zealand play a key role in reducing the southward penetration of the EAC extension, which in turn causes the time-mean partial separation of the EAC to be 1.1° further north than it would be in the absence of New Zealand.

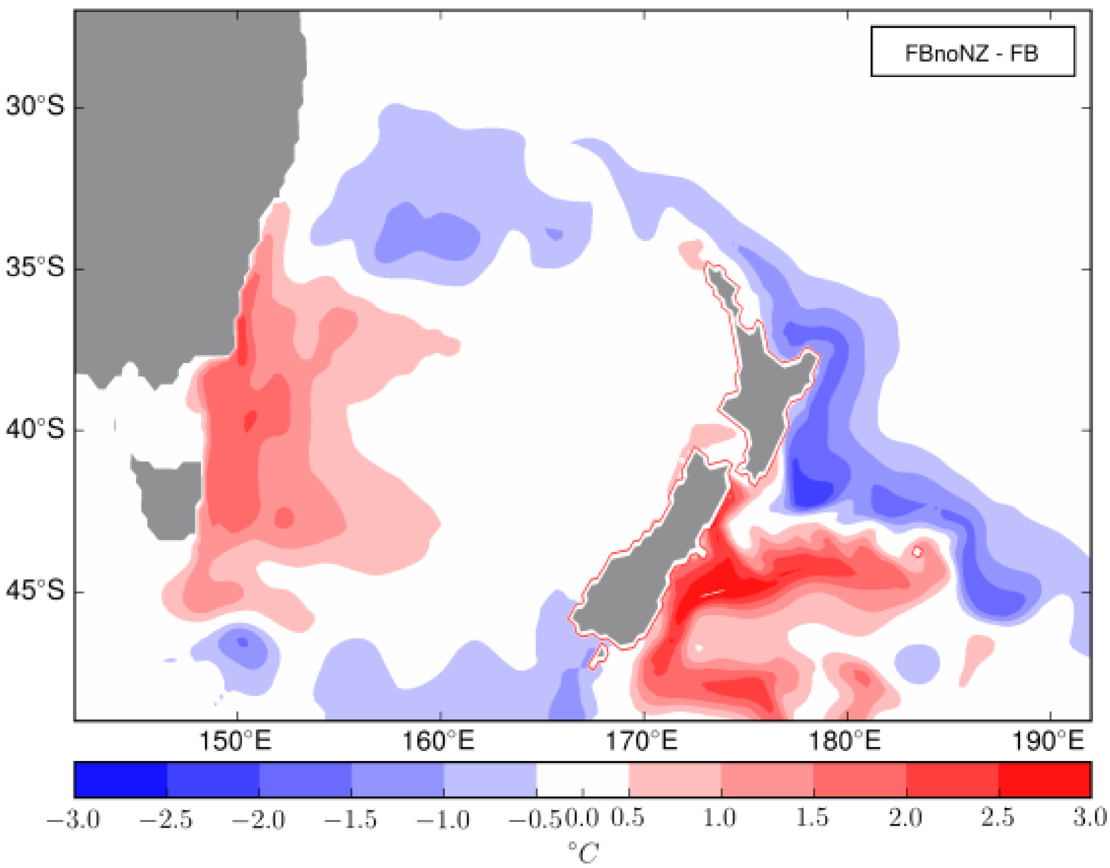

Figure 2-6. Time-mean sea surface temperature difference between FB and FBnoNZ.

We now focus on the largest changes between the experiments, namely between FB and FBnoNZ (with and without New Zealand where all bathymetry below 1km is levelled to 4km, respectively). The SSH variability changes shown in Figure 2-5 corroborate the former discussion around the Tasman Sea circulation changes shown in Figures 2-1, 2-3, 2-4. Specifically, FBnoNZ has reduced variability in the separation region, Tasman Front and East Auckland Current but enhanced variability in the southern half of the Tasman Sea and south of Tasmania. The circulation changes between experiments FB and FBnoNZ demonstrate the importance of the New Zealand submarine platform in setting the spatial structure of temperature in the Tasman Sea as shown in Figure 2-6. The greater southward migration of EAC extension eddies in FBnoNZ, as compared to FB (discussed in Figure 2-4 and also visible in Figure 2-5) leads to a warming of ~2°C in the EAC extension region. Due to the change in the EAC's partial separation and weakening of the Tasman Front (see Figure 2-1g-h), there is a similar reduction in temperature across the Tasman Sea and the East Auckland Current. The warming on the south-eastern side of New Zealand on partial removal of Campbell Plateau is due to the elimination of topographic steering, which normally directs cold Subantarctic waters northward.

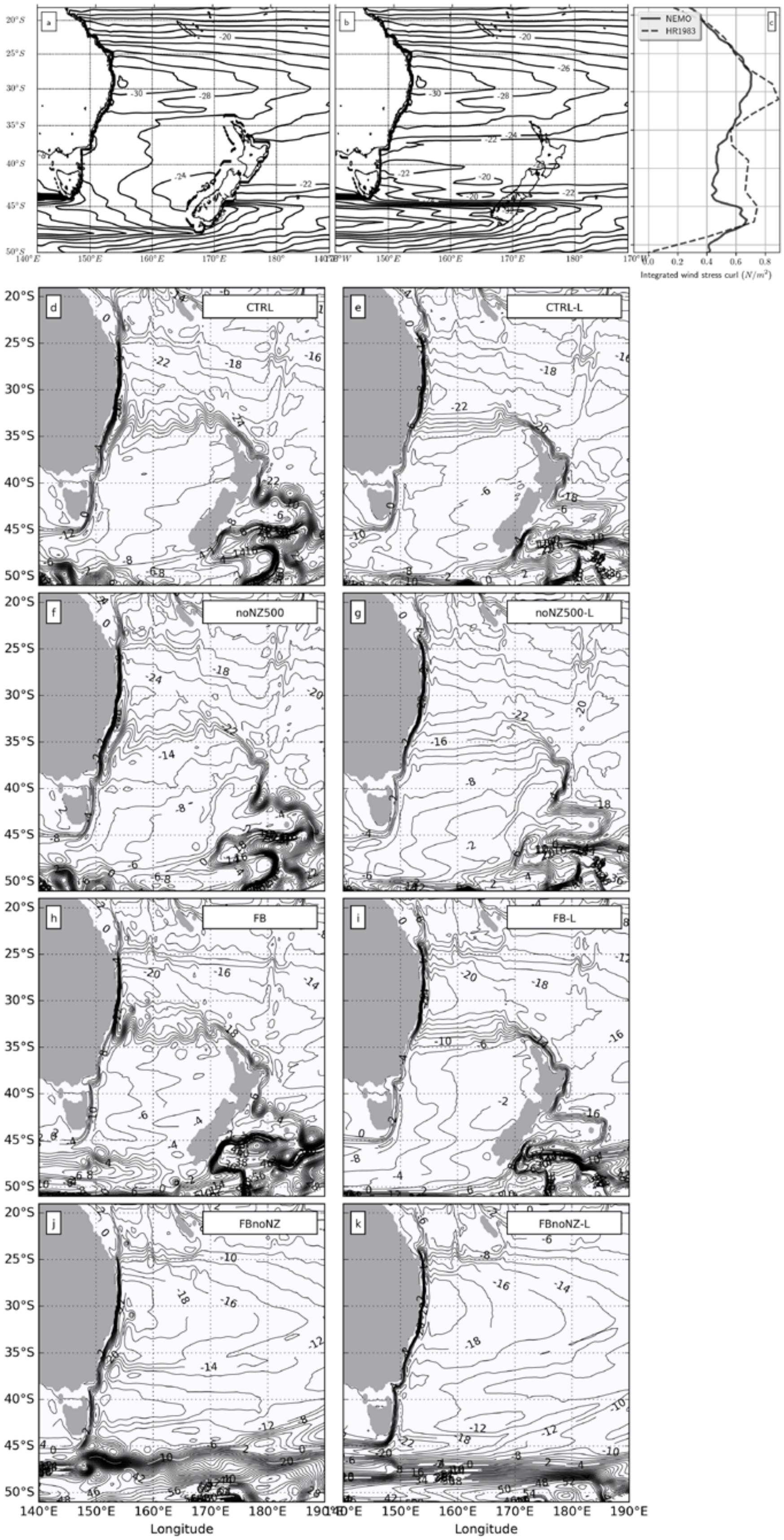
NEMO
HR1983
Integrated wind stress curl (N/m^2)
CTRL
CTRL-L
noNZ500
noNZ500-L
FB
FB-L
FBnoNZ
FBnoNZ-L
Longitude
Longitude

Figure 2-7. Analytical Godfrey Island Rule stream function comparison with a) and without b) New Zealand where stress and curl fields are from NEMO (time-mean ERA-interim atmospheric reanalysis as felt by ORCA025-L75-MJM95), contours every 2 Sv. c) time-mean zonally integrated South Pacific (145°E-291°E) wind stress curl from NEMO and Hellerman and Rosenstein [1983]. d-k) time-mean barotropic streamfunction (integration taken eastward from Australia down to 1945m; contours every 2 Sv) for perturbed bathymetry NEMO simulations.

Barotropic streamfunctions for different model parameters are shown in Figure 2-7 to investigate the dynamical reasons for the changes in Tasman Front position and EAC separation latitude. The Sverdrup/Island Rule stream function in Figure 2-7a-b illustrates the importance of New Zealand in setting the time-mean location of the EAC outflow under ERA-Interim forcing. Comparing Figure 2-7a with Figure 2-7b, when the New Zealand coastline is removed, the outflow is no longer constrained by the northern tip of New Zealand. This southward shift in the position of the Tasman Sea outflow was not seen in the Tilburg et al. [2001] solution and is likely caused by different meridional gradients in the wind stress curl products shown in Figure 2-7c (further discussed in Section 2.5). The narrow zonal outflow extending westward of Auckland in Figure 2-7b is due to localised patches of positive and negative curl around the Bay of Plenty (see Figure 0-2b) and is likely a forcing dataset artefact.

In the Tilburg et al. [2001] RG1/RG2 simulations, the authors inferred that nonlinearities were unimportant for setting the time-mean EAC separation; this issue is now revisited. Figure 2-7d-k examines the importance of nonlinear processes by comparing NEMO experiments with (left column) and without (right column) the non-linear advection terms in the momentum calculation. These experiments extend the 1.5-layer linear experiments RG1 and RG2 of Tilburg et al. [2001] by including continental shelves, stratification and topographic steering. Consistent with Ridgway and Godfrey [1994] and Tilburg et al. [2001], circulation features that are reliant on eddies (for example, the mean EAC retroflection or eddy driven recirculation at ~32°S in Figure

2-7h) are not present in the linear simulation (FB-L in Figure 2-7i). On the gyre-scale, the inclusion of momentum advection (Figure 2-7d,f,h,j) breaks the north-south symmetry of the gyre, leading to downstream intensification of the EAC (compare Figure 2-7j,k). Away from the western boundary, the effects of changing topography on the mean Tasman Front are similar in the linear and non-linear experiments. The linear experiments in Figure 2-7e,g,i show a similar, narrow Tasman Front when New Zealand or the subsurface New Zealand landmass is present (slightly broader in noNZ500-L), whereas the complete removal of New Zealand leads to a broader outflow than in the nonlinear case (Figure 2-7j,k). In summary, the presence of the New Zealand submarine platform is crucial to maintaining a narrow, coherent current across the northern Tasman Sea, and nonlinearity is important in controlling the extent of the retroflection in the EAC extension.

2.5 Discussion and Conclusions

Using a suite of modified bathymetry NEMO ocean model experiments we have found that the complete removal of New Zealand leads to broader offshore flow (formerly the Tasman Front) and an EAC extension that extends further south. These experiments challenge the conventional view that the EAC's partial separation is set by the wind field alone [*Tilburg et al.*, 2001; *Ridgway and Dunn*, 2003]. Due to the small surface area where New Zealand is removed and the minor effect of relative wind [*Dawe and Thompson*, 2006], the CTRL and FBnoNZ experiments are driven by nearly the same time-mean integrated wind stress curl. Since FB and FBnoNZ show different EAC partial separation behaviour, these results show that the steepest gradient in the basin-averaged wind stress curl is not the sole factor determining the latitude of partial separation of the EAC. This is an important consideration for attribution studies (e.g. [*Oliver and Holbrook*, 2014; *Feng et al.*, 2016]) that relate changes in circulation to changes in the wind-stress curl.

Tilburg et al. [2001]'s analysis of the removal of New Zealand was limited in a number of ways. First, their 1.5-layer model represented landmasses by their 250m isobath and could not address the effect of removing subsurface features such as shelves and ridges. Second, their East Auckland Current flowed north (the wrong direction) and lastly, the model they used did not incorporate higher vertical modes, isopycnal outcropping or non-linear dynamics (vorticity advection and flow instabilities). The NEMO model solutions address many of these deficiencies, particularly the role of sub-surface bathymetry. We found that the mean flow in the linear NEMO model experiments is qualitatively consistent with the full NEMO solutions, with the main exception that nonlinearity affects the extent of the mean retroflection in the EAC extension. We infer that deep bathymetry plays a major role in forming a narrow Tasman Front and nonlinear processes (e.g. eddies, rectification, momentum advection, etc.) are crucial for the extent of the EAC retroflection.

We find that removal of New Zealand affects the Tasman Front latitude in our linear and nonlinear experiments, in contrast to the linear experiments of *Tilburg et al.* [2001]. We attribute this difference to our use of the ERA-Interim wind stress product which is a significant improvement on the *Hellerman and Rosenstein* [1983] product used by *Tilburg et al.* [2001], as it is based on ERS-1, ERS-2 and QuickSCAT satellite coverage between 1992 and 2009 [Dee et al., 2011]. In particular, the *Hellerman and Rosenstein* [1983] integrated wind stress curl drops steeply from 30°S to 35°S (north of New Zealand) but falls more gradually between 29°S and 42°S in ERA-Interim (Figure 2-7c). Sverdrup dynamics dictate a strong outflow from the EAC in the region of strong wind stress curl gradient, explaining why *Tilburg et al.* [2001] found little effect of New Zealand on the Tasman Front (or EAC separation) latitude. In contrast, our Sverdrup/Godfrey Island Rule calculation with ERA-Interim (Figure 2-7a-b) shows that the outflow location moves south when New Zealand is removed. Features obviously related to topography and nonlinearity aside, linear and nonlinear NEMO experiments show the same effect (Figure 2-7d-k). We conclude that when New Zealand is absent, the maximum wind stress curl gradient sets the Tasman Front latitude but if New Zealand is present then the latitude of maximum wind stress curl gradient sets the Tasman Front location if it is north of New Zealand, but otherwise New Zealand sets the Tasman Front location.

The timescales, resolution dependence and dynamics that determine the EAC partitioning between the EAC extension and Tasman front remain an interesting topic that requires further investigation. Improving our understanding of the EAC dynamics controlling the separation is a key step towards quantifying climate change driven impacts on regional circulation and marine ecosystems. Whilst this study has shown that New Zealand affects the position of the EAC separation and Tasman Front under 1989-2009 ERA-Interim forcing, the degree to which this relationship persists under anthropogenic changes to the wind stress curl is an open question. Future work could perturb the wind field in a realistic way and look at changes in Tasman Sea circulation with respect to response times and sensitivity (e.g. [*Durgadoo et al.*, 2013]). Coarse-resolution (1° at 30°S) modelling results suggest that the Tasman Front transport is correlated to EAC transport [*Sloyan and O'Kane*, 2015]; analogous results in the Agulhas system however have shown that decoupling between the Agulhas current and Agulhas leakage occurs at higher resolutions [*Loveday et al.*, 2014; *Holton et al.*, 2016]. Hence, future work is best completed with eddy-resolving resolution in which the wind field is perturbed in isolation.

Part 3. Wind forced variability in eddy formation, eddy shedding and the separation of the East Australian Current.

Part 3 contains a reformatted version of the published manuscript:

Bull, C. Y. S., Kiss, A. E., Jourdain, N. C., England, M. H., & van Sebille, E. (2017). Wind forced variability in eddy formation, eddy shedding and the separation of the East Australian Current. *Journal of Geophysical Research: Oceans*, 122. https//doi.org/10.1002.2017JC013311.

Abstract

The East Australian Current (EAC), like many other subtropical western boundary currents, is believed to be penetrating further poleward in recent decades. Previous observational and model studies have used steady state dynamics to relate changes in the westerly winds to changes in the separation behaviour of the EAC. As yet, little work has been undertaken on the impact of forcing variability on the EAC and Tasman Sea circulation. Here, using an eddy-permitting regional ocean model, we present a suite of simulations forced by the same time-mean fields, but with different atmospheric and remote ocean variability. These eddy-permitting results demonstrate the non-linear response of the EAC to variable, non-stationary inhomogeneous forcing. These simulations show an EAC with high intrinsic variability and stochastic eddy shedding. We show that wind stress variability on timescales shorter than 56 days leads to increases in eddy shedding rates and southward eddy propagation, producing an increased transport and southward reach of the mean EAC extension. We adopt an energetics framework that shows the EAC extension changes to be coincident with an increase in offshore, upstream eddy variance (via increased barotropic instability) and increase in sub-surface mean kinetic energy along the length of the EAC. The response of EAC separation to regional variable wind stress has important implications for both past and future climate change studies.

3.1 Introduction

The East Australian Current (EAC) in the western South Pacific Ocean is Australia's strongest and most important boundary current, supporting Australia's temperate coastlines by transporting 1.35±0.42 PW of heat poleward [*Wu et al.*, 2012; *Hu et al.*, 2015; *Sloyan et al.*, 2016]. At around 30-32°S the EAC partially bifurcates into the Tasman Front and the EAC extension [*Cetina-Heredia et al.*, 2014], and in the process of separating, the EAC sheds a large number of eddies in a region known as the EAC extension [*Everett et al.*, 2012]. These eddies propagate southwest toward Tasmania and a smaller portion continue around Tasmania into the Indian Ocean via a flow pathway known as the Tasman leakage [*van Sebille et al.*, 2012]. Via the Tasman Leakage, the EAC participates in the Southern Hemisphere supergyre circulation, a key pathway of the global thermohaline circulation [*Ridgway and Dunn*, 2007; *Speich et al.*, 2007].

Given the growing interest in the likelihood of changes in the mid-latitude westerlies driving an enhancement of the EAC extension [*Cai et al.*, 2005; *Ridgway*, 2007a; *Roemmich et al.*, 2007, 2016; *Oliver and Holbrook*, 2014; *Sloyan and O'Kane*, 2015; *Feng et al.*, 2016], understanding the factors that influence the mean circulation in the Tasman Sea is an important problem to consider. The large-scale South Pacific gyre circulation is believed to be determined by the wind stress curl, *Godfrey* [1989] Island Rule and Sverdrup balance [*Gray and Riser*, 2014; *Thomas et al.*, 2014]. It is well documented (e.g. [*Rhines and Schopp*, 1991; *Verron and Le Provost*, 1991; *Kiss*, 2010b]) that wind features (such as the steepest gradient in the integrated wind stress curl) offer at best a partial explanation for the separation latitude of western boundary currents (WBCs) due to the importance of advection in these regions. The norm in the climate change literature however, is that linear theory and time-mean low-frequency changes in forcing are often used to attribute changes in WBC regions (e.g. [*Wu et al.*, 2012]). Using observations (Maria Island temperature/salinity and XBTs) and two ocean state estimates, *Hill et al.* [2011] invoke steady-state linear dynamics to associate changes in the basin-scale wind stress curl with the southern extent of the South Pacific gyre; they also found the EAC extension and Tasman Front transport to be anti-correlated. This wind-induced partitioning (also termed a 'gating effect' [*Ganachaud et al.*, 2014]) of the EAC's pathway has been discussed by several subsequent studies on a range of time-scales using both observations and models (e.g. [*Oliver and Holbrook*, 2014; *Chiswell and Sutton*, 2015; *Hu et al.*, 2015; *Sloyan and O'Kane*, 2015]). Since subtropical gyres readily respond to low-frequency decadal wind forcing variability [*Willebrand et al.*, 1980; *Roemmich et al.*, 2016], existing work on the EAC gating effect has focused on low-frequency south Pacific basin-scale responses [*Cai et al.*, 2005; *Hill et al.*, 2011; *Oliver and Holbrook*, 2014]; yet little is known about how the Tasman Sea circulation responds to local higher-frequency wind forcing.

There are a number of known factors that influence the East Australian Current's mean flow and variability. Due to the Indonesian Throughflow [*Tomczak and Godfrey*, 2003] the EAC has the weakest mean flow of the major WBCs [*Mata et al.*, 2000, 2006; *Tomczak and Godfrey*, 2003]; 22.1 Sv at 27°S [*Sloyan et al.*, 2016]. Whilst the mean flow dominates the energy field at 27°S [*Sloyan et al.*, 2016], at 30°S the energy field is increasingly eddy-rich with the mean and standard deviation of transport being of a similar magnitude [*Mata et al.*, 2000]. The EAC exhibits a large seasonal cycle of 8.9 Sv at 27°S, with a narrower, higher transport (36.3 Sv) in Austral summer and a broader, weaker transport (27.4 Sv) during winter [*Ridgway and Godfrey*, 1997]. *Qiu and Chen* [2004] observed that the EAC's seasonal cycle in EKE appears to be similar in amplitude and phase to the seasonal cycle in EKE of the south equatorial countercurrent. Subsequent studies *Bowen et al.*, [2005] and *Mata et al.* [2006], focusing on mesoscale variability did not find strong evidence of offshore forcing. Recent work has implicated baroclinic Rossby waves in EAC transport variability at interannual to decadal timescales [*Hill et al.*, 2008, 2011; *Holbrook et al.*, 2011; *O'Kane et al.*, 2014; *Sloyan and O'Kane*, 2015].

The growth, migration and detachment of EAC eddies determine the EAC's separation latitude and the eddies are a large component of the transport in the EAC extension. Through the EAC's bifurcation and subsequent shedding process, the EAC spawns an eddy approximately every 100 days [*Mata et al.*, 2006]. A number of studies have attempted to understand the processes that cause the formation, detachment and reattachment of mesoscale eddies in the separation region. *Nilsson and Cresswell* [1980] suggest a Rossby wave propagates westward along the Tasman Front to the separation region, reflecting off the coast, and subsequently pinching off eddies. *Marchesiello and Middleton* [2000], using a regional modelling configuration, corroborated the *Nilsson and Cresswell* [1980] eddy shedding process. In contrast, the contemporary view via observational and modelling studies [*Bowen et al.*, 2005; *Mata et al.*, 2006; *Wilkin and Zhang*, 2007] suggests eddies arise from locally generated mixed baroclinic and barotropic instabilities propagating southward along Australia's east coast with little involvement from Rossby waves at the eddy-shedding timescale. Although idealised models show that variable forcing can control the timing of intrinsic WBC variability (e.g. [Kiss and Frankcombe, 2016]), it remains an open question whether variable forcing can influence the timing of EAC eddy shedding or change the relative importance of barotropic/baroclinic instability in the EAC.

Past studies suggest that both barotropic and baroclinic instabilities are active in the EAC eddy shedding process; *Bowen et al.* [2005] and *Mata et al.* [2006] propose that barotropic energy conversion is the larger term in the separation region, although this dominance is not confirmed by *Oliver et al.* [2015]. Future climate change simulations by

Oliver et al. [2015] suggest that increases in both barotropic and baroclinic instabilities will drive increased growth and lifetime of anti-cyclonic eddies in the EAC extension, and this leads to a near doubling of eddy-related southward heat transport in the EAC Extension. *O'Kane et al.* [2014] and *Sloyan and O'Kane* [2015] suggest that upstream EAC transport has not changed significantly in recent decades whereas increases in the EAC extension transport since 1948 are associated with propagating baroclinic disturbances across the South Equatorial Current into the East Australian Current. However, the *Sloyan and O'Kane* [2015] study was limited by a coarse 1° resolution which is unable to accurately resolve the EAC.

In summary, the EAC displays variability on a wide range of timescales; whilst the EAC appears to respond to low-frequency basin-scale variability and perhaps also local high-frequency forcing, the partitioning of variability in the EAC system between the intrinsic variability, and the response to these different forcings, remains unknown. The focus of this study is to characterise the EAC's intrinsic variability and response in terms of both local and remote forcing. Specifically, this study will examine the influence of steady and variable forcing on:

1. the mean state of the EAC in terms of the partial separation, strength of EAC extension and Tasman sea circulation;
2. EAC eddy formation and shedding;
3. the barotropic and baroclinic energy conversion in the EAC region.

Using the Nucleus for European Modelling of Ocean model (NEMO), we present a hierarchy of eddy-permitting simulations beginning with steady forcing (no synoptic, seasonal or interannual variability), and then introducing variability in the remote ocean boundaries, followed by atmospheric variability in the local Australasian domain, and finally full variability in both local and remote regions (see Section 3.2.3 for discussion on the anticipated response). The experiments/model configuration is described in Section 3.2 with model evaluation in Section 3.3. Results characterising the dominant role of the regional surface forcing in the rectified circulation in the Tasman Sea are given in Sections 3.4.1-3.4.3 and a mechanism is proposed in Section 3.4.4. Discussion and opportunities for further work are given in Section 3.5.

3.2 Model and methods

3.2.1 Ocean model configuration

The ocean general circulation model used in this study is version 3.4 of the Nucleus for European Modelling of Ocean model [*Madec*, 2012] (NEMO). NEMO solves the incompressible, Boussinesq, hydrostatic, primitive equations with a filtered free surface. NEMO uses a z-coordinate C-grid with partial cells at the bottom-most layer in order to provide more realistic representation of bottom topography [*Barnier et al.*, 2006]. At the lateral continental boundaries, a free slip condition is employed which means that there is no velocity gradient (i.e. no horizontal shear) at the solid boundaries of the model. The energy- and enstrophy- conserving momentum advection scheme and free slip configuration used have been found to be optimal for realistic variability of WBCs [*Penduff et al.*, 2007; *Le Sommer et al.*, 2009; *Fransner*, 2012]. Topography is taken from the ETOPO1 dataset [*Amante and Eakins*, 2009]. In our configuration, NEMO has 75 vertical levels, with 24 levels in the upper 100m and 22 levels between 100-1000m; this enables realistic representation of coastlines and continental shelves. This high number of near-surface levels also improves fidelity of the mixed-layer and thermocline variations [*Bernie et al.*, 2005], as well as resolution of baroclinic flow [*Stewart et al.*, 2017]. NEMO is run with a prognostic turbulent kinetic energy (TKE) scheme for vertical mixing. Laterally we have spatially varying eddy coefficients (according to local mesh size) with a Laplacian operator for iso-neutral diffusion of tracers and a biharmonic operator for lateral diffusion of momentum.

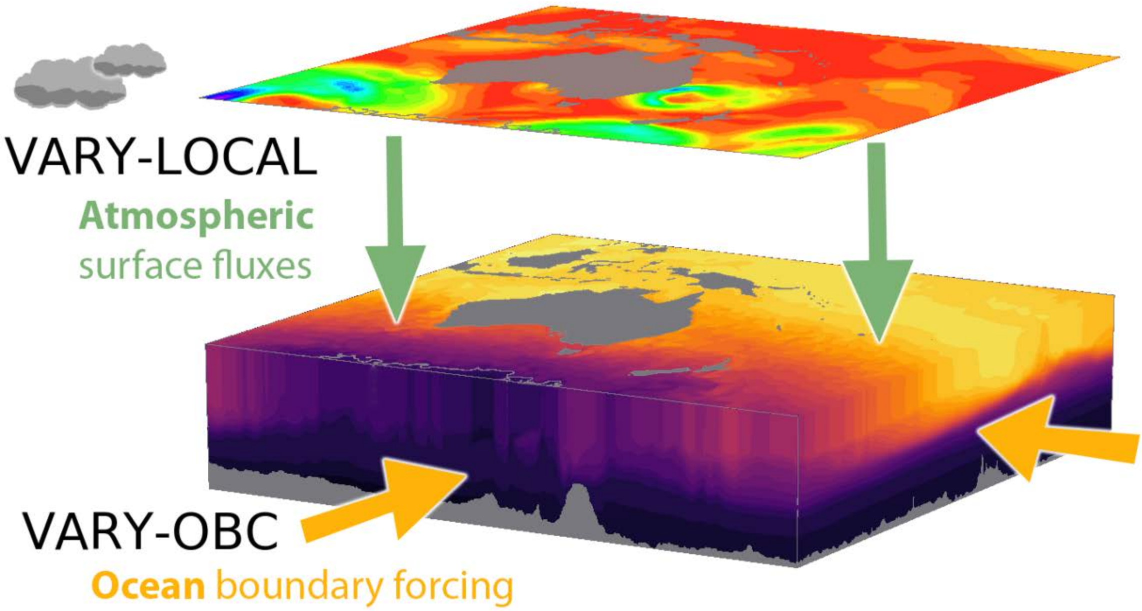

Figure 3-1. Experiment design schematic that illustrates the model domain and spatial extent of the variable forcing. NEMO configuration has a regional domain (pictured, bottom) that is forced by ERA-Interim at the surface and ORCA025-L75-MJM95 in the ocean boundaries. The four main experiments consist of: 1. steady surface forcing and ocean boundary conditions (CONSTANT), 2. varying the remote ocean (VARY-OBC), 3. varying surface fluxes (VARY-LOCAL) and 4. varying both the remote ocean and local forcing (VARY-ALL). Fields are illustrative only, pictured are snapshots (14-05-2005) of the variable surface wind stress (top) and temperature (bottom).

The regional Australasian model domain is pictured in Figure 3-1. The grid is curvilinear (shown in Figure 3-2) with an eddy-permitting (nominally 1/4°) horizontal resolution. Specifically, the meridional width of each grid cell is 24.5 km whereas the zonal width varies with both longitude and latitude between 19.5 and 24.5 km. This regional simulation is forced by temperature, salinity, u/v-velocity at the open ocean boundaries with 5-day means from a global NEMO ocean simulation run at 1/4° resolution with 75 vertical levels (namely, ORCA025-L75-MJM95, provided by the DRAKKAR/MyOcean group [*Barnier et al.*, 2007, 2011]). Further details regarding the handling of the ocean boundary conditions are given in section 8.4 in *Madec* [2012], *Barnier et al.* [1998] and *Marchesiello et al.* [2001]. ORCA025-L75-MJM95 was forced by the 3-hourly T255 (~0.75°) ERA-interim atmospheric reanalysis [*Dee et al.*, 2011] through the CORE bulk formulae. The initial conditions for ocean temperature and salinity are taken from *Levitus et al.* [1998] with an ocean at rest. The regional simulation surface forcing is also from the ERA-interim atmospheric reanalysis [*Dee et al.*, 2011] between 1989-2009. There is no sea surface salinity relaxation in the regional domain; precipitation plus runoff minus evaporation determines the freshwater flux across the air-sea interface. The temporal resolution of ERA-Interim in the regional domain depends on the variable: winds and humidity are imposed at 3-hourly time-steps whereas precipitation and long wave/short wave radiation are imposed daily. Our simulations are analysed from 1994-2009, in which ERA-interim uses data from continuous satellite wind stress coverage, namely, ERS-1, ERS-2, and QuickSCAT [*Dee et al.*, 2011].

3.2.2 Experiments

The ERA-Interim variables within the Australasian domain will be referred to as the *local forcing* and the ocean boundary conditions (OBCs; taken from the ORCA025-L75-MJM95 simulation) will be called the *remote forcing*. All experiments have the same time-mean local and remote boundary forcing.

Experiment Name	**Description**
1. CONSTANT	Control experiment: all forcing fields, both local and remote taken from the twenty-year time-mean fields
2. VARY-OBC	Constant time-mean local forcing but varying remote ocean boundary conditions
3. VARY-LOCAL	Constant time-mean remote forcing but varying local surface atmospheric forcing (over the regional model domain)
4. VARY-ALL	Both local and remote forcing are fully varying (i.e. realistic forcing)
5. <56	Constant time-mean remote forcing and constant local buoyancy fluxes. Local wind stress variability <56 days only
6. 56-148	Constant time-mean remote forcing and constant local buoyancy fluxes. Local wind stress variability 56-148 days only
7. 148-330	Constant time-mean remote forcing and constant local buoyancy fluxes. Local wind stress variability 148-330 days only
8. 330-400	Constant time-mean remote forcing and constant local buoyancy fluxes. Local wind stress variability 330-400 days only
9. >400	Constant time-mean remote forcing and constant local buoyancy fluxes. Local wind stress variability >400 days only

Table 3.1. List of regional NEMO experiments designed to characterise the EAC's intrinsic variability and response in terms of both local and remote forcing. Four main experiments (1-4) assess the impact of local and remote forcing variability, five further experiments (5-9) determine which wind frequencies in the local wind stress forcing are responsible for the changes seen in the Tasman Sea mean circulation (see Section 3.4).

Table 3.1 summarises the four main experiments (1-4) used to assess the impact of local and remote forcing variability on the Tasman Sea circulation. CONSTANT has no local or remote forcing variability. The surface atmospheric forcing for the VARY-LOCAL simulation contains variability across different time scales, from 3-hourly averages for winds and humidity, through to daily, seasonal and interannual time-scales for those and all other variables. The variable remote ocean forcing for simulation VARY-OBC, contains 5-days to interannual time-scales in temperature, salinity and velocity via the open ocean boundary conditions. VARY-ALL has both local and remote forcing variability (i.e. VARY-LOCAL and VARY-OBC).

In contrast to idealised studies [*Pedlosky*, 1965; *Veronis*, 1970; *Willebrand et al.*, 1980; *Andres et al.*, 2012; *Jouanno et al.*, 2016] the experiments here utilise realistic bathymetry, coastlines, stratification and non-stationary/non-homogeneity in the wind stress fields. The novelty of these experiments is that they progress from an idealised time-mean steady forcing to a fully varying realistic configuration (i.e. VARY-ALL) that would be typical of the oceanic component of a CMIP model.

In the variable local forcing cases, taking the time-mean of the wind velocity field would result in different time-mean wind *stress* fields, due to the quadratic dependence of the wind stress on the wind velocity (e.g. [*Zhai*, 2013]) and non-linear terms in the calculation of the drag coefficient [*Large and Yeager*, 2004]. As the focus of this study is the non-linear EAC response to variable forcing, this issue is best avoided. Therefore, the NEMO simulations described above are run with directly prescribed air-sea fluxes (including heat, freshwater and stress) in the regional domain. To obtain the fluxes and minimise temperature and salinity drift, NEMO was first run with fully varying ERA-Interim fluxes using the CORE bulk formulae with absolute wind [*Large and Yeager*, 2004], and the resulting 3-hourly surface stress, freshwater and heat fluxes were stored and used to force all the above NEMO simulations (including VARY-ALL), using the time-mean where described. This approach ensures that the time-mean of all components of air-sea fluxes to be the same across all the experiments in Table 3.1, regardless of the variability imposed in the forcing.

Experiments 5-9 in Table 3.1 are used to determine which wind frequencies in the local wind stress forcing are responsible for the changes we see in the mean circulation (see Sections 3.4). These have fixed lateral boundary conditions as in VARY-LOCAL, and all surface fluxes except for the wind stress are also fixed. The wind stress field in the local domain (used to force VARY-LOCAL and VARY-ALL) contains variability from 3-hourly to interannual timescales. In experiments 5-9 we high-pass, low-pass- or band-pass the wind stress via various "brick wall" filters in the frequency domain, yielding five experiments forced by variability restricted to: 5) <56 days 6) 56-148 days 7) 148-330 days 8) 330-400 days 9) >400 days period. The time-mean wind stress from the unfiltered forcing is also added to the filtered forcing in experiments 5-8 so that all five experiments include the same time-mean. Experiment 5 is intended to capture synoptic to monthly variability with experiments 6-9 capturing progressively longer modes of variability. In particular, experiment 8 contains the annual peak and experiment 9 has inter-annual and longer variability. Our approach of filtering the wind field in frequency space avoids leakage of adjacent frequencies unlike the commonly used monthly averaging strategy (e.g. [*Penduff et al.*, 2011; *Wu et al.*, 2016]).

Similar to other boundary current regional configurations (e.g. [*Renault et al.*, 2016b]), experiments are spun-up for five years (in this case Jan. 1989 – Dec. 1993; see Figure 3-13), and all results presented in this study use daily-averaged model output from 16 years of integration after spin-up (Jan. 1994 – Dec. 2009).

3.2.3 Theoretical expectations: anticipated response to varying forcing

The anticipated EAC response from steady to realistically varying forcing warrants an *a priori* discussion, in which we also define some necessary terminology. We define *intrinsic variability* as variability arising without any variability in the local surface forcing or remote ocean boundary conditions. This terminology differs from some studies, for example Sérazin et al. [2015] who define intrinsic variability as ocean variability arising from an atmospheric forcing with a repeated climatological seasonal cycle. *Rectification* is defined as the emergence of a different time-mean state (despite the same time-mean forcing) due to variability in the atmosphere or ocean boundary conditions. Oceanic variability is a result of a combination of (1) the response of the ocean to local and/or remote forcing variability, and (2) intrinsic dynamical instability processes (e.g. barotropic/baroclinic instability, or topographically generated eddies and meanders in oceanic jets) [Stammer and Wunsch, 1999]. On the large scale, the time-mean wind stress alone is expected to drive an oceanic circulation characterised by an intense WBC that is intrinsically unstable (e.g. [*Pedlosky*, 1996]). The wind field's fluctuating component alone can also give rise to rectified mean currents, that are likely much weaker in magnitude [*Willebrand et al.*, 1980]. The subsequent mean and rectified mean currents from the mean and variable winds interact to create a new mean circulation. To put this in context, the CONSTANT experiment will only have mean currents from the mean forcing whereas the VARY-LOCAL simulation will have the net interaction of time-mean currents from the time-mean and variable forcing. Whilst the difference between the VARY-LOCAL and CONSTANT simulations will allow us to infer the effect of local variable forcing, this study will not characterise the rectified mean circulation from variable forcing with zero mean. Similar approaches to understanding the effect of variable forcing are used in *Penduff et al.* [2011] and *Jouanno et al.* [2016].

3.2.4 Estimating the Separation Latitude

The separation latitude of the EAC is calculated from each daily average output, using SSH contours to indicate a separation of the main current from the coast, following the method described by [*Cetina-Heredia et al.*, 2014; *Ypma et al.*, 2016]. This method captures eddy detachment and reattachment, which characterises changes in the separation latitude on short timescales. The method involves:

1. Finding the core of the EAC upstream of the separation at 28°S, defined as the maximum southward geostrophic surface velocity as determined from the SSH field.

2. Following the SSH contour at the location of the maximum velocity southwards, and then recording the first location at which the contour turns more than 30°S eastward of south as the separation latitude.

Daily separation latitudes lying more than 1 standard deviation from the 50-day running mean are considered false detections and ignored (gray crosses in Figure 3-6).

3.2.5 Eddy tracking

This study uses the eddy detection and tracking algorithm developed by *Chelton et al.* [2011] and coded by *Oliver et al.* [2013]. Eddy detection involves finding closed contours of sea level anomalies above a specified threshold for each daily map of filtered sea surface height. Additional necessary criteria include: a minimum eddy radius, peak amplitude and local extrema for cyclonic and anti-cyclonic eddies. Eddy tracks are then generated for each eddy by searching for all eddy centroids at successive time steps that lie within a specified ellipsoid centred on the eddy. Further details of the algorithm can be found in Appendix B2 of *Chelton et al.* [2011] and its implementation can be found in Appendix A of *Oliver et al.* [2013].

3.2.6 Energetics

Energetics metrics are used to quantify differences in the energy conversion between the experiments. Here, we define the eddy state as any deviation from the time-mean state; this results in a Reynolds decomposition of the zonal (u) and meridional (v) velocities into their time-mean ($\bar{u}, \bar{v}$) and eddy-varying components (u', v'), and similarly for density ρ. We calculate the following widely-used (e.g. [*Eden and Böning*, 2002; *Bowen et al.*, 2005; *Mata et al.*, 2006; *Loveday et al.*, 2014; *Oliver et al.*, 2015]) quantities (all averaged between depths z_1 and z_2):

- Mean Kinetic Energy, MKE(x,y) = $\frac{\rho_0}{2(z_2-z_1)}\int_{-z_2}^{-z_1}(\bar{u}^2+\bar{v}^2)\ dz;$ (1)

- Eddy Kinetic Energy, EKE(x,y) = $\frac{\rho_0}{2(z_2-z_1)}\int_{-z_2}^{-z_1}(\overline{u'^2}+\overline{v'^2})\ dz;$ (2)

- Mean potential energy →Eddy potential energy (MPE→EPE),

$$\mathrm{BCC} = \frac{g}{z_2-z_1}\int_{-z_2}^{-z_1}\left(\frac{\overline{u'\rho'}\frac{\partial\tilde{\rho}}{\partial x}+\overline{v'\rho'}\frac{\partial\tilde{\rho}}{\partial y}}{\frac{\partial\tilde{\rho}}{\partial z}}\right)dz; \quad (3)$$

- MKE→EKE is BTC $= -\frac{\tilde{\rho}}{z_2-z_1}\int_{-z_2}^{-z_1}\left(\overline{u'u'}\frac{\partial\bar{u}}{\partial x}+\overline{u'v'}\left(\frac{\partial\bar{u}}{\partial y}+\frac{\partial\bar{v}}{\partial x}\right)+\overline{v'v'}\ \frac{\partial\bar{v}}{\partial y}\right)dz.$ (4)

Physically, positive values of 3 are an indication of baroclinic instability (BCC) and positive values of 4 suggests the occurrence of barotropic instability (BTC). Since $z_2 - z_1$ is the thickness of each latitude/longitude grid cell, the depth average removes the effects of topography/partial cells. The kinetic energy is based on $\rho_0 = 1035\ kg\ m^{-3}$, as that is the value used in NEMO in solving the momentum equations under the Boussinesq approximation. Density for BCC and BTC was calculated from the temperature and salinity fields using the Jackett and McDougall [1994] Equation of State which matches the method used in this version of NEMO. Reference stratification $\tilde{\rho}(z)$ is approximated by the zonally and meridionally averaged density; see the Appendix in *Kang and Curchitser* [2015] for a discussion of the sensitivity to the reference stratification. Typical of other studies using these metrics (e.g. [*Böning and Budich*, 1992; *Haidvogel and Beckmann*, 1999; *Mata et al.*, 2006]), contributions from vertical velocities are likely small and so are neglected. Similarly, these diagnostics are calculated offline from daily average fields where the following relation simplifies the computation: $\overline{u'u'} = \overline{uu} - \bar{u}\bar{u}$ [*Stewart et al.*, 2015; *Doddridge et al.*, 2016].

3.3 Evaluation of the simulated Tasman Sea circulation (VARY-ALL)

3.3.1 Mean and variability of sea surface height

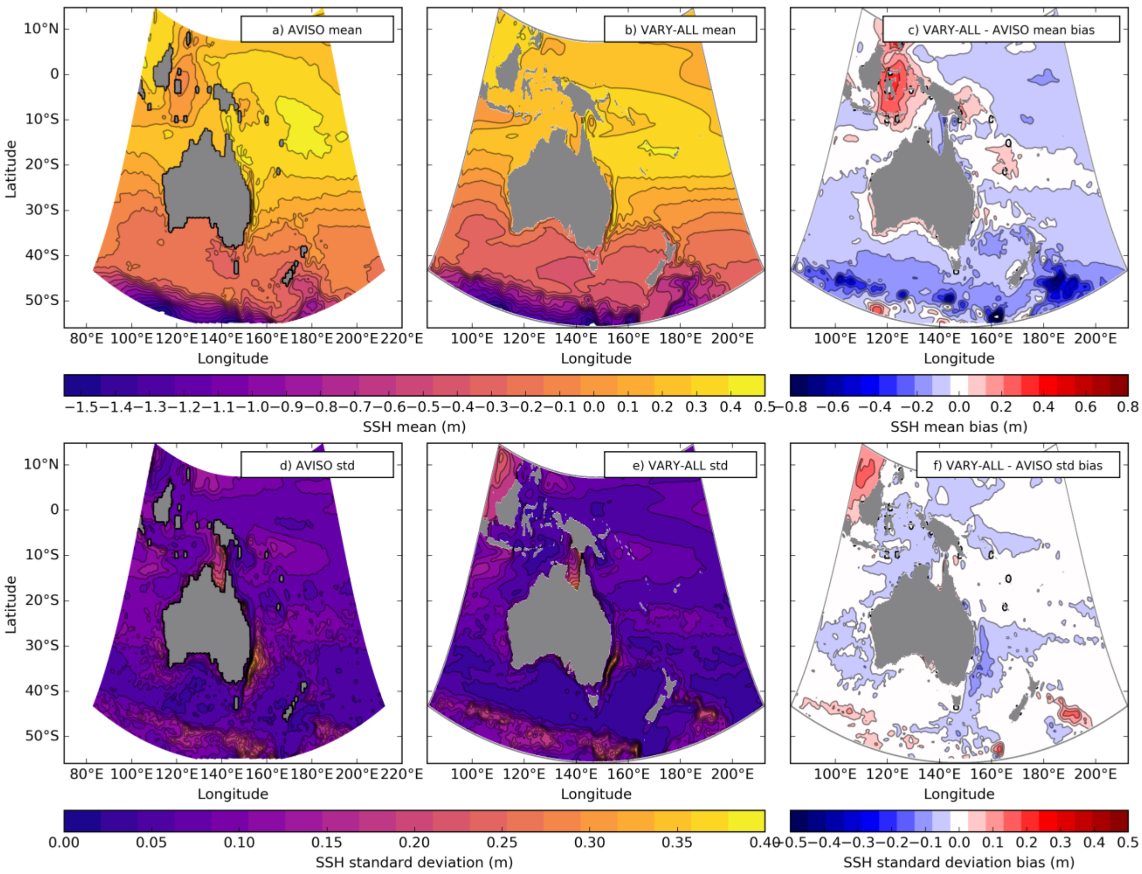

Figure 3-2. Comparison of VARY-ALL (NEMO) and AVISO sea surface height (SSH) between 1994-2009. a-b) mean SSH anomaly and d-e) SSH standard deviation. The sea surface height mean anomalies in a,b are relative to the temporal and spatial average to emphasise the difference in time-mean gradients between VARY-ALL and AVISO. Biases of VARY-ALL relative to AVISO are given in panels c,f.

In Figure 3-2, the VARY-ALL simulation with full variability is evaluated with respect to satellite altimetry (AVISO) over 1994-2009 when the available observations and simulation overlap. The VARY-ALL Tasman Sea large-scale circulation is similar to the observations; specifically, the East Australian Current and East Auckland Current are clearly visible in VARY-ALL. In particular, the EAC's modelled SSH gradients are similar in location and structure. Biases however do exist (Figure 3-2c); for example, there are SSH gradients in the Indonesian Throughflow that are not present in VARY-ALL and the modelled SSH gradients across the Tasman Front are sharper than the observations. The Antarctic Circumpolar Current region has biases in the location and strength of fronts along the southern edge of the domain, particularly in Figure 3-2c. These biases may be related to the ORCA025-L75-MJM95 ocean boundary conditions, limited fidelity in the resolved bathymetry and the relatively coarse resolution of the model configuration (since the Rossby radius decreases as latitude increases).

The variability of sea surface height in VARY-ALL is also in good agreement with AVISO in many areas (see white areas in Figure 3-2f) but underestimated by up to 50% in the East Australian Current (Figure 3-2d-f). This understimation is typical of 1/4° eddy-permitting resolution models (e.g. [*Ypma et al.*, 2016]). There is also an enhancement of variability in the north-western corner of the domain, which is largely an artefact of running a regional simulation in which equatorially trapped waves cannot exit the domain. Given that this spurious variability is far away from our region of interest it is unlikely to adversely affect the results presented.

3.3.2 Depth-integrated transports in the East Australian Current region

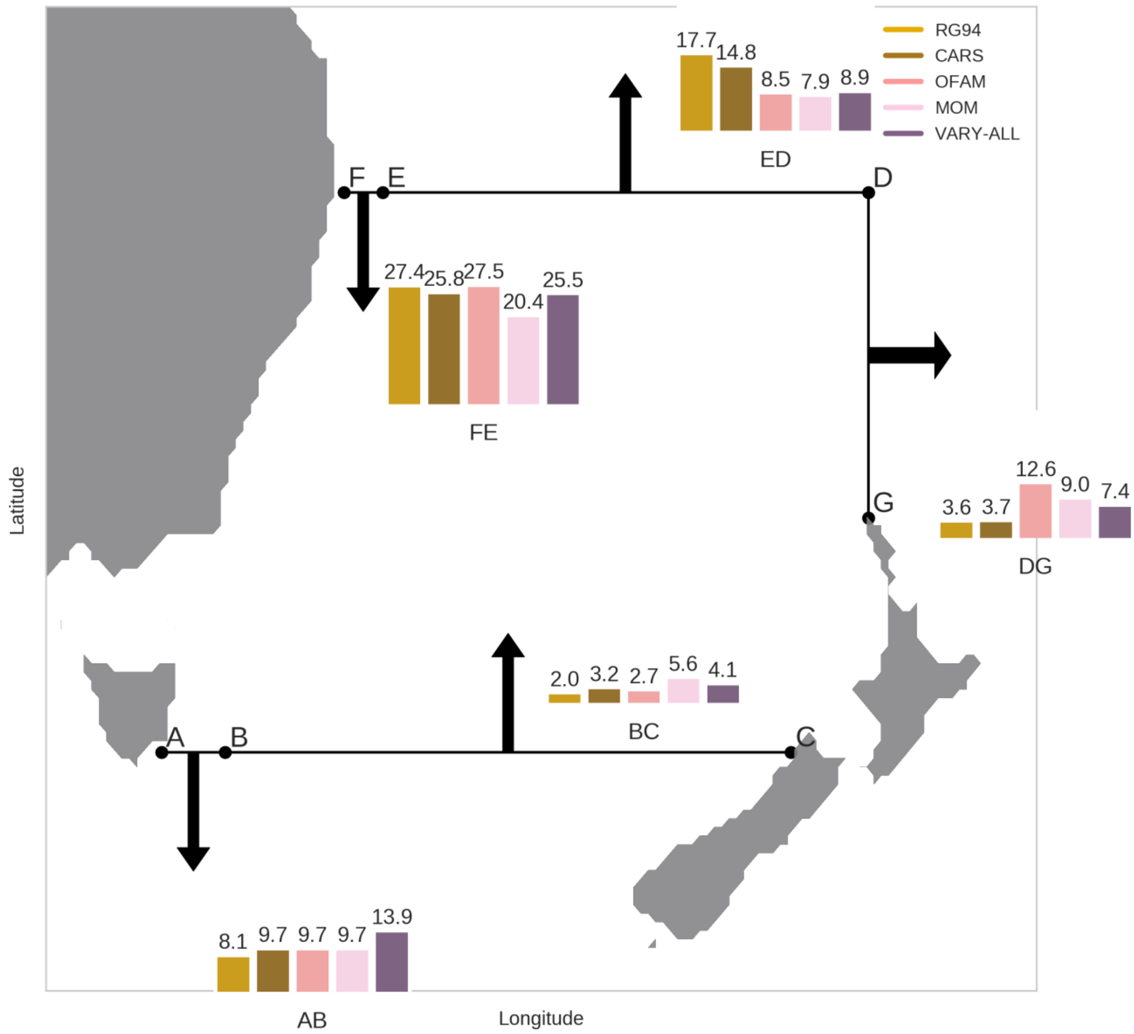

Figure 3-3. Schematic of VARY-ALL (NEMO) mean depth-integrated transport with observations (browns) and models (pinks). Units are Sverdrups. NEMO transports are depth-integrated to 1945m. The observations are from Ridgway and Godfrey [1994] (RG94) and CARS, via Oliver and Holbrook [2014]. Model transports OFAM (1/10° resolution) and MOM (1/4° resolution) are from Oliver and Holbrook [2014] and Ypma et al. [2016], respectively. Here, OFAM is forced by a repeatedly ‘‘normal year’’ forcing representing the decade of the 1990s from ERA-40 [*Chamberlain et al.*, 2012; *Oliver and Holbrook*, 2014] and MOM uses a CORE-NYF forcing [*Large and Yeager*, 2008; *Griffies et al.*, 2009]. Section end points are similar to Oliver and Holbrook [2014] but sections are aligned with the curvilinear model grid (not strictly zonal/meridional) transport is calculated using grid, normal velocities. The section end points are: A (148.2°E 42.6°S), B

(150.8°E 42.6°S), C (172.5°E 40.6°S), D (171.3°E 25.8°S), E (155.6°E 27.6°S), F (153.6°E 27.8°S), G (173.6°E 34.9°S), H (146.9°E 43.4°S) and I (146.9°E 45.8°S).

Depth-integrated time-mean (1994 – 2009) transports down to 1945m in VARY-ALL and observations in the Tasman Sea are shown in Figure 3-3. These section locations and observations are also analysed in *Oliver and Holbrook* [2014]. Section end points match those of *Oliver and Holbrook* [2014], insofar as the model grid allows, to ensure a closed transport budget. The observations originate from RG94 [*Ridgway and Godfrey*, 1994; *Ridgway and Dunn*, 2003] and the CSIRO Atlas of Regional Seas (CARS) climatology [*Ridgway et al.*, 2002] using a reference level of 2000 dbar (level of no motion). Model transports from OFAM and MOM are from Oliver and Holbrook [2014] and Ypma et al. [2016], respectively. The VARY-ALL (NEMO), MOM, OFAM and RG94 transports include both Ekman and geostrophic components, but the CARS transports are geostrophic components only. From Figure 3-5 in *Oliver and Holbrook* [2014], the Ekman components are 0-12% of the RG94 geostrophic transport for sections FE, ED, DG, AB and 100% for BC, thus aside from BC, we can expect the omission of the Ekman component in CARS would have only a small effect on the results presented.

Comparing transports flowing into the boxed Tasman Sea region to observations, the VARY-ALL simulation approximately captures the core EAC transport (FE) but overestimates the southern inflow (BC). The modelled upstream EAC transport (FE) of 25.5 Sv is within the observed and modelled range of EAC transports shown in Figure 3-3, and most importantly the recent 18-month full-depth 152km wide mooring based observations by *Sloyan et al.* [2016] at 27°S, namely 22.1±7.5 Sv. Across BC, given that the observed geostrophic transport varies by 2.2 Sv (1.0 Sv in RG94 versus 3.2 Sv in CARS), the bias in the VARY-ALL simulation is small.

Examining transports out of the Tasman Sea box, we see a weaker northward outflow (ED) compensated by anomalously strong eastward outflows (DG) and the EAC extension (AB). Comparing combined north-eastward outflow (DG+ED), VARY-ALL (16.2 Sv) and MOM (16.9 Sv) simulate a weaker DG+ED outflow than is observed by RG94 (21.3 Sv) and CARS (18.5 Sv). Having said this, whilst not directly comparable to DG, more recent, direct mooring observations of the Tasman Front in the Tasman Sea interior give a higher mean transport of 7.8 Sv [*Sutton and Bowen*, 2014] with high variability ranging between -4 and 17.8 Sv (4.4 Sv standard deviation). The VARY-ALL simulation's large bias in the EAC extension (AB) is likely offset by having the weakest north-eastward outflow at DG+ED as well as the previously discussed stronger inflow across BC.

In summary, whilst biases in transport magnitude remain, the VARY-ALL simulation captures the overall structure and magnitude of Tasman Sea flow.

3.4 Results

Throughout this part the CONSTANT experiment is used as a control because it is the shared basis of all nine experiments (see 3.2.2 or Table 3.1) and also enables a characterisation of changes in the mean and variable state of the Tasman Sea circulation that are not intrinsic to the mean forcing.

3.4.1 Sea Surface height and transport comparison

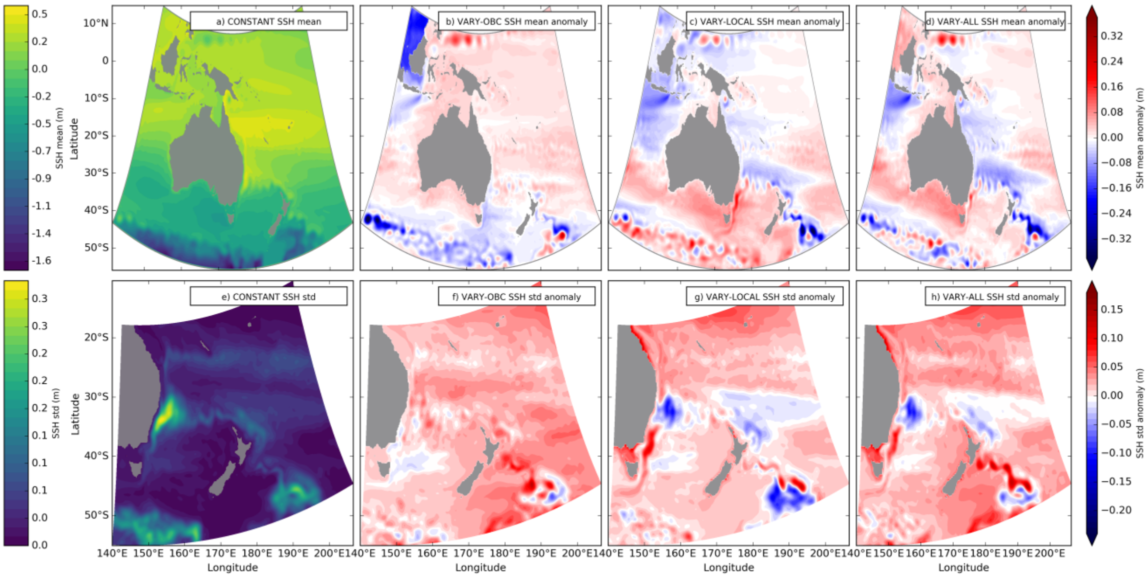

Figure 3-4. (a) Sea surface height (m) and (e) its standard deviation (m) for the CONSTANT (control) experiment. (b-d) SSH anomaly relative to CONSTANT for VARY-OBC, VARY-LOCAL and VARY-ALL, respectively (to emphasise the changes in the geostrophic currents between each experiment, the area-mean is removed from each sea surface height field.) (f-h) SSH standard deviation anomaly relative to CONSTANT for VARY-OBC, VARY-LOCAL and VARY-ALL, respectively. Positive anomalies indicate values exceed CONSTANT.

Spatial maps of NEMO sea surface height mean and standard deviation anomalies under differing forcing are presented in Figure 3-4. In the Tasman Sea, VARY-ALL more closely resembles VARY-LOCAL than VARY-OBC in the changes of SSH mean and standard deviation relative to CONSTANT. Assuming the forcing effects are linear, this suggests that the local surface forcing is largely responsible for the spatial pattern of change seen in VARY-ALL in the Tasman Sea.

Focusing on the time-mean changes from CONSTANT in Figure 3-4b-d, VARY-LOCAL and VARY-ALL have the largest changes in the Tasman Sea circulation, with a less distinct Tasman Front and a more defined EAC extension (clearest in Figure 3-4c and Figure 3-5a). The standard deviation of sea surface height (Figure 3-4f-h) shows the spatial changes in variability between the experiments with forced variability and CONSTANT. VARY-OBC shows a basin-wide increase in variability and a relatively small reduction in eddy activity in the EAC extension. In both the VARY-LOCAL and VARY-ALL (Figure 3-4g-h) simulations there is a large reduction in variability in the EAC separation region, and also an increase in variability in both the upstream region of the EAC and the EAC extension. *Ypma et al.* [2016] also find enhancement of variability both upstream and in the EAC extension when changing from atmospheric normal year forcing to forcing with full interannual variability (their Figure 3-3c,d); however, unlike Figure 3-4g-h, they additionally found enhanced variability in the separation region.

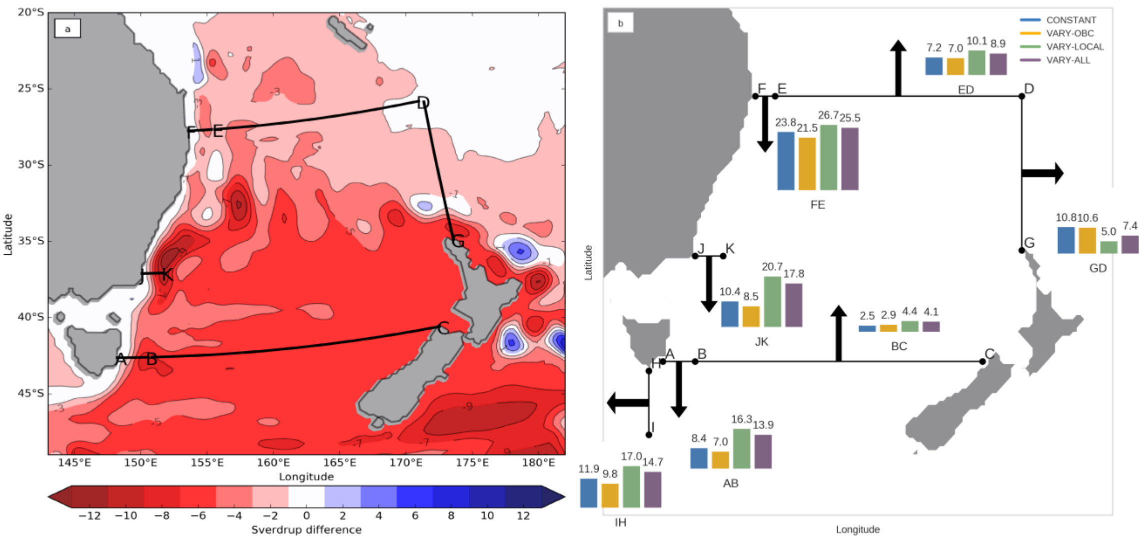

Figure 3-5. a) time-mean barotropic streamfunction difference between VARY-LOCAL and CONSTANT (integration taken eastward from Australia down to 1945m where the undifferenced streamfunction is defined by $(U, V) = (-{}^{\partial\Psi}/_{\partial y}, {}^{\partial\Psi}/_{\partial x})$; contours every 2 Sv). The CONSTANT streamfunction values are negative, so red (blue) differences indicate areas of enhanced (reduced) transport when local surface forcing is introduced. b) Comparison of depth-integrated transport (Sv) to 1945 m between CONSTANT (blue), VARY-OBC (yellow), VARY-LOCAL (green) and VARY-ALL (lavender). The section end points are the same as Figure ValTranObs, with the addition of points: J (150.1°E 37.1°S) and K (151.7°E 37.1°S).

The dramatic change in mean SSH gradients between CONSTANT and VARY-LOCAL in the EAC separation region can be visualised more clearly using a barotropic streamfunction (Figure 3-5a). The Tasman Sea-wide shift seen in the VARY-LOCAL experiment in Figure 3-4c, is now more clearly visualised as an overall increase in transport across the Tasman Sea with the largest depth-integrated increases in transport in the EAC extension along the coast of Australia. The depth-integrated transports in Figure 3-5b corroborate this story, indicating that the variability in the local surface forcing (VARY-LOCAL) increases the proportion of mean EAC transport that flows into the EAC Extension (section JK), with a concomitant reduction in the transport in the Tasman Front (section GD).

Figure 3-5b quantifies the effect of variable forcing on the time-mean Tasman Sea circulation. Across all coastal sections and experiments, the EAC post-separation (JK) displays the largest range of transports (8.5-20.7 Sv). Despite a modest mean change in upstream EAC transport (FE), we see a large rectification response at JK of 10.3 Sv between CONSTANT and VARY-LOCAL down to 1945m (standard error in the mean at JK is 0.7 Sv and 1.6 Sv, respectively). Across all sections excluding GD and BC, relative to the steady-state forcing in CONSTANT we find that variability in the remote ocean (VARY-OBC) weakens mean transport; for all sections excluding GD, variability in both the local/remote forcing (VARY-ALL) increases transport, and variability in the local forcing alone (VARY-LOCAL) produces the largest mean transport. The calculated net transport into the Tasman Sea bounded by A-F is 0.2 to 0.5 Sv for the four experiments, smaller than the imbalances of 0.5±2, -0.8, 0.6, and 1.5 Sv in *Ridgway and Godfrey* [1994], CARS, [*Ypma et al.*, 2016] and [*Oliver and Holbrook*, 2014], respectively. Interestingly, since all four experiments feel the same time-mean wind stress curl, a steady-state linear Sverdrup-Island-Rule [*Sverdrup*, 1947; *Godfrey*, 1989] model would give the same transport across GD, whereas our model gives a wide range of Tasman Sea outflow transports, from 5 to 10.8 Sv. Before proposing a mechanism for the described rectified circulation (section 6.4) we first examine changes in EAC variability.

3.4.2 Changes in EAC transport variability

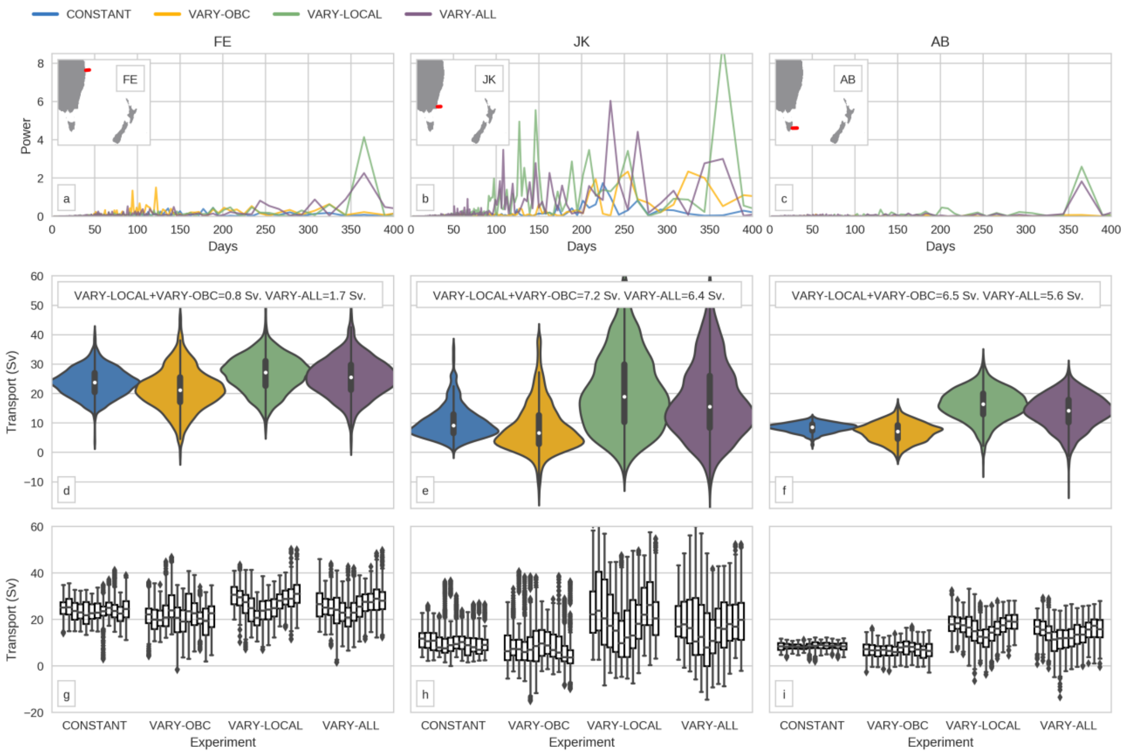

Figure 3-6. Comparison of depth-integrated (to 1945 m) southward transport timeseries in terms of power spectra (a, b, c), violin plots (d, e, f) and box plot for each month Jan-Dec (g, h, i), where each column is a different transport section across FE/JK/AB (see inset in a,b,c for location of section) for the four experiments (CONSTANT/VARY-OBC/VARY-LOCAL/VARY-ALL). The violin plots contain a normal box plot with the additional 'violin' indicating the transport distribution through a kernel density estimate (Scott reference rule is used for bandwidth selection). The top and bottom of each box (d-i) indicates the inter-quartile range (IQR). The median is represented by a white dot (d, e, f) or the mark within the box (g, h, i). The whiskers in (d-i) extend 1.5 x IQR beyond the box; dots that fall outside the whiskers (g-i only) are thus considered outliers. The textboxes in panels d-f check the linearity of the response in terms of median transport anomaly relative to CONSTANT.

We now explore how changes in transport variability determine the different mean states discussed in Section 3.4.1. To this end, Figure 3-6 shows power spectra, violin plots and boxplots for coastal EAC sections (FE/JK/AB) for the four experiments. Figure 3-6d shows that the upstream EAC has large intrinsic variability with CONSTANT the least variable and VARY-OBC the most variable. Specifically, Figure 3-6d shows that the CONSTANT EAC upstream (FE) Inter-Quartile Range (IQR) of transport is 6.5 Sv; the remaining experiments have a larger IQR ~8.5 Sv. The upstream EAC transport (FE) standard deviation for CONSTANT (4.8 Sv) is a sizeable fraction of that for VARY-OBC, VARY-LOCAL and VARY-ALL (7.1, 6.1 and 6.5 Sv, respectively). These values are similar to the EAC transport standard deviation of 7.5 Sv found by *Sloyan et al.* [2016] in an 18-month full-depth 152km wide mooring at 27°S. Comparing to CONSTANT, the increased IQR of VARY-OBC at JK and AB corroborates work by *Hill et al.* [2010], suggesting remote oceanic variability affects EAC extension transport variability.

The period with the greatest power in the power spectra (Figure 3-6a, b, c) is the annual peak at 365 days in the VARY-LOCAL experiment. A suggestion of seasonality is shown in the boxplots for the VARY-LOCAL and VARY-ALL experiments at FE and AB (Figure 3-6g, i). At FE, this is likely the documented summertime peak in upstream EAC transport [*Ridgway and Godfrey*, 1997; *Wang et al.*, 2013]. It is notable that remote forcing appears to play little role in the seasonality of the upstream EAC (VARY-OBC, Figure 3-6a). In all sections (Figure 3-6a, b, c), VARY-ALL appears to have a weaker annual peak compared to VARY-LOCAL, suggesting that the varying ocean boundary conditions are dampening the annual signal. Section JK is interesting as there are peaks for VARY-LOCAL/VARY-ALL between 90-200 days, some with a similar magnitude to the annual peak. This variability is likely related to the documented EAC eddy-shedding timescale [*Mata et al.*, 2000, 2006; *Bowen et al.*, 2005] (90-140, ~100, 90-180 days, respectively) and will be examined more closely in the next section.

3.4.3 Changes in eddy shedding and the EAC separation latitude

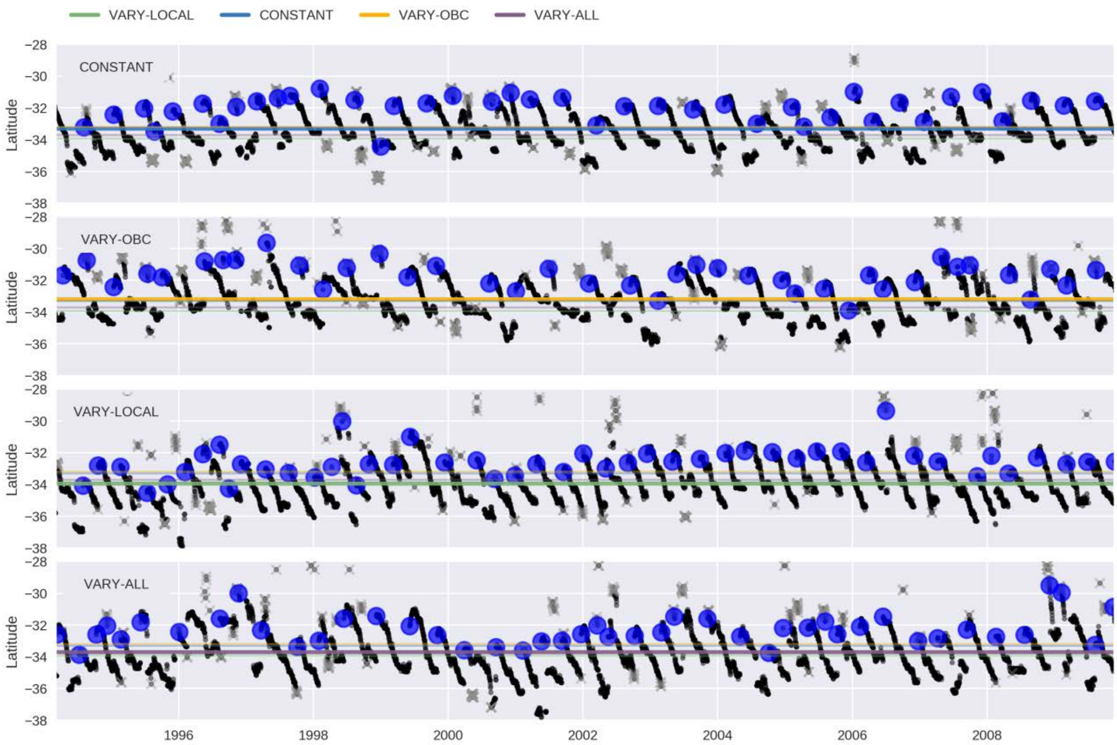

Figure 3-7. Separation latitude time series comparison. Black dots are detected separation latitude (grey crosses are considered false-positive outputs by the separation latitude algorithm). A 'retraction event' (blue circles) is defined as the times when the separation latitude jumps northward by more than 1.5° in a single day. Separation latitude mean is indicated for all experiments by horizontal lines.

Time-series of the separation latitude (details in Section 3.2.4) for the four experiments are presented in Figure 3-7. The separation latitude in the experiments including local forcing variability (i.e. VARY-LOCAL/VARY-ALL) is consistently further south. The mean separation latitude shift of 0.7°S (supplementary Figure 3-14) between CONSTANT and VARY-LOCAL exceeds the standard error in these means

(0.1° in both cases), indicating that the mean separation change is statistically significant despite being small relative to the variability. Moreover, the 0.7°S EAC separation shift is similar to the increase in mean separation latitude found in recent eddy-resolving simulations applying trends in forcing. For example, *Oliver and Holbrook* [2014] found a 0.8°S shift from present to future climate in a ~60 year A1B climate change scenario and *Cetina-Heredia et al.* [2014] found a modelled ~0.6° poleward mean shift during 1980-2010. The implications of this result will be discussed further in Section 3.5.

The introduction of variability in the local surface forcing decreases the time between eddy shedding events. There are 41, 40, 49, 45 detected retraction events (blue circles) in CONSTANT, VARY-OBC, VARY-LOCAL, VARY-ALL, respectively. Whilst the variability in retraction period is high (supplementary Figure 3-15), the introduction of regional atmospheric variability (VARY-LOCAL) leads to a 15% decrease in the mean time between eddy shedding events as compared to the intrinsic EAC eddy shedding timescale (CONSTANT). This change is statistically significant relative to the standard error in the mean. Given the increase in variability in the post-separated EAC in VARY-LOCAL in Figure 3-6e, it is notable that the EAC retraction period's IQR is smallest (i.e. the shedding is most regular) with regional atmospheric variability (VARY-LOCAL), suggesting that the annual cycle in the local forcing (see Figure 3-12f) may play some role in the timing of eddy-shedding.

3.4.4 Dynamics of rectified Tasman Sea circulation

Since we have now established that the variability in the EAC extension is mostly attributable to variability in the local atmospheric forcing, the remainder of Section 3.4 will focus on the differences between the CONSTANT and VARY-LOCAL experiments.

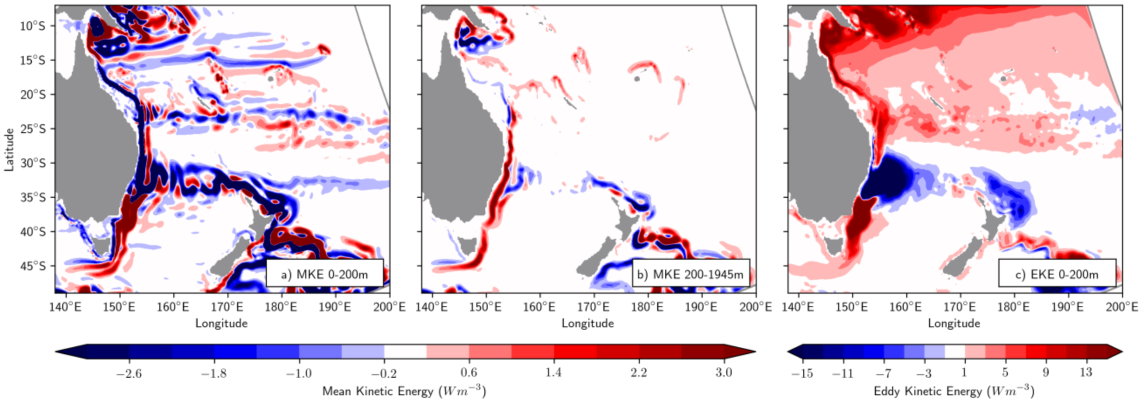

Figure 3-8. Change in VARY-LOCAL (a) 0-200m average MKE, (b) 200-1945m average MKE, and (c) 0-200m average EKE relative to CONSTANT.

Figure 3-8 shows large-scale changes in the Eddy Kinetic Energy (EKE) field at the surface (0-200m) and changes in the Mean Kinetic Energy field (MKE) at the surface and at depth (200-1945m) with the introduction of local variability. Near-surface MKE is increased in the EAC extension region but generally reduced upstream in the EAC, the EAC separation region, Tasman Front and offshore in the South Caledonian jet. In contrast, the response below 200m is a consistent enhancement of MKE along the coast. Stronger MKE at depth is consistent with an enhanced EAC extension (Figure 3-5a) and the idea that water parcels below approximately 460m are more likely to end up in the EAC extension [*Ypma et al.*, 2016]. Figure 3-8c shows a broad enhancement of near-surface EKE across the Pacific north of 25°S, with a strong increase in upstream coastal EKE up to Papua New Guinea. An increase in EKE south of New Caledonia also appears in VARY-LOCAL. Strong surface EKE south of New Caledonia can be seen in AVISO [*Qiu and Chen*, 2004], ORCA-R025 [*Barnier et al.*, 2006] and OFAM3 also forced by ERAI [*Feng et al.*, 2016]. Additionally, there is a large reduction in EKE in the upstream offshore area/separation region (25°S-35°S, 150°E-160°E) and a large increase in EKE in the EAC extension region (35°S -42°S, ~153°E). EKE differences below 200m (not shown) are similar to c). In summary, when the local surface forcing varies, the near-surface EKE in the upstream EAC and subsurface MKE along the pathway of the EAC are enhanced.

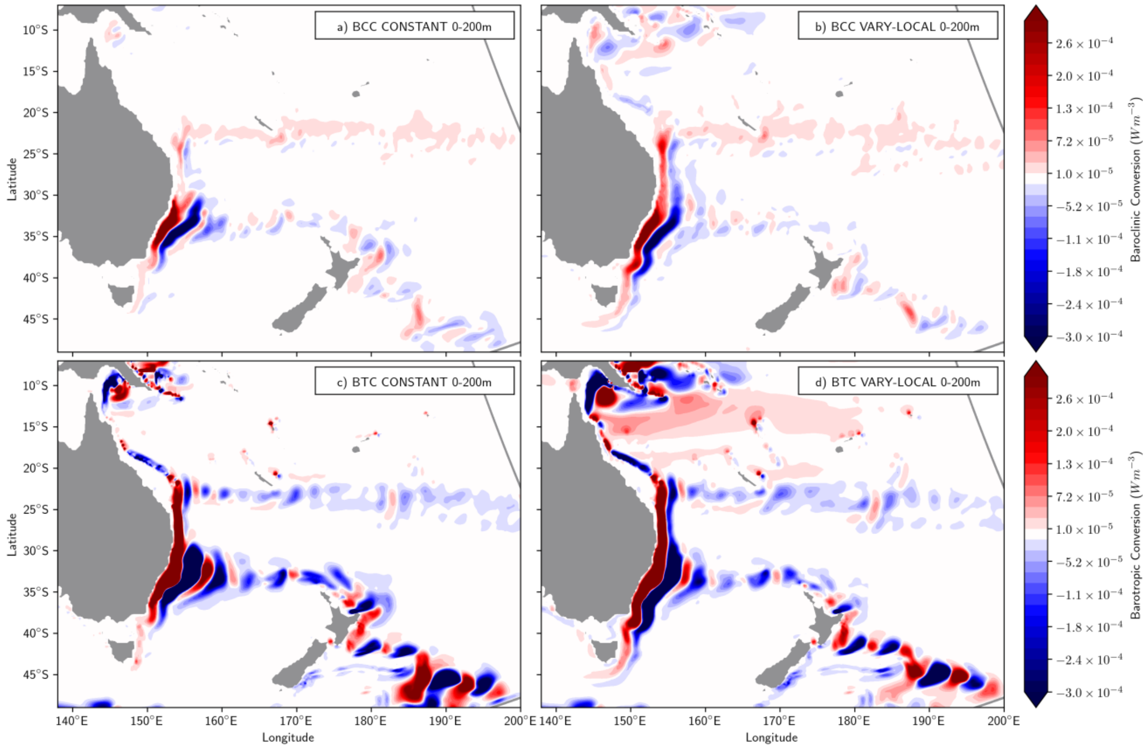

Figure 3-9. Baroclinic (BCC) and barotropic (BTC) conversion terms depth-averaged 0-200m for CONSTANT (a,c) and VARY-LOCAL (b,d). Positive values of these terms imply mean-to-eddy energy conversion.

Figure 3-9 shows the depth averaged (surface-200m) baroclinic (BCC) and barotropic (BTC) conversion terms (Section 3.2.6). In both CONSTANT and VARY-LOCAL cases, consistent with previous studies [*Bowen et al.*, 2005; *Mata et al.*, 2006; *Oliver et al.*, 2015], the coastal EAC region exhibits mixed barotropic/baroclinic conversion (positive values) suggesting both energy pathways are responsible for eddy generation. We now consider changes in the conversion terms firstly offshore, secondly upstream and lastly along the EAC coastal region (Figure 3-10).

Figure 3-9d shows a large increase in MKE → EKE (BTC) offshore of north-eastern Australia (12°S-20°S, 145°E-180°E) under local surface forcing (VARY-LOCAL). This is likely related to the established dominance of barotropic energy conversion in the region. Specifically, *Qiu and Chen* [2004] found that the seasonal variability of the EKE signal in the South Equatorial Current system was related to the varying strength of barotropic energy conversion and the seasonal intensity of the SECC jet. With local surface forcing variability (VARY-LOCAL) there is an increase in both MPE→EPE and EPE→MPE along the Queensland coast (Figure 3-9a,b). Finally, there are small increases in EKE → MKE (Figure 3-9d) and MPE → EPE (Figure 3-9b) south of New Caledonia. This increase in baroclinic energy conversion is located in the same position as the baroclinic waveguide south of New Caledonia discussed by *O'Kane et al.* [2014] and *Sloyan and O'Kane* [2015]. The non-linear, baroclinic flows south of New Caledonia are maintained by some of the strongest observed gradients between tropical and subtropical waters in the region [*Couvelard et al.*, 2008].

In the upstream EAC, there is a stronger, more continuous path of both MPE→EPE and EPE→MPE energy conversion in the VARY-LOCAL simulation (Figure 3-9a,b); the inshore positive contribution suggesting increased MPE → EPE conversion is consistent with stronger upstream eddy energy shown in Figure 3-8c.

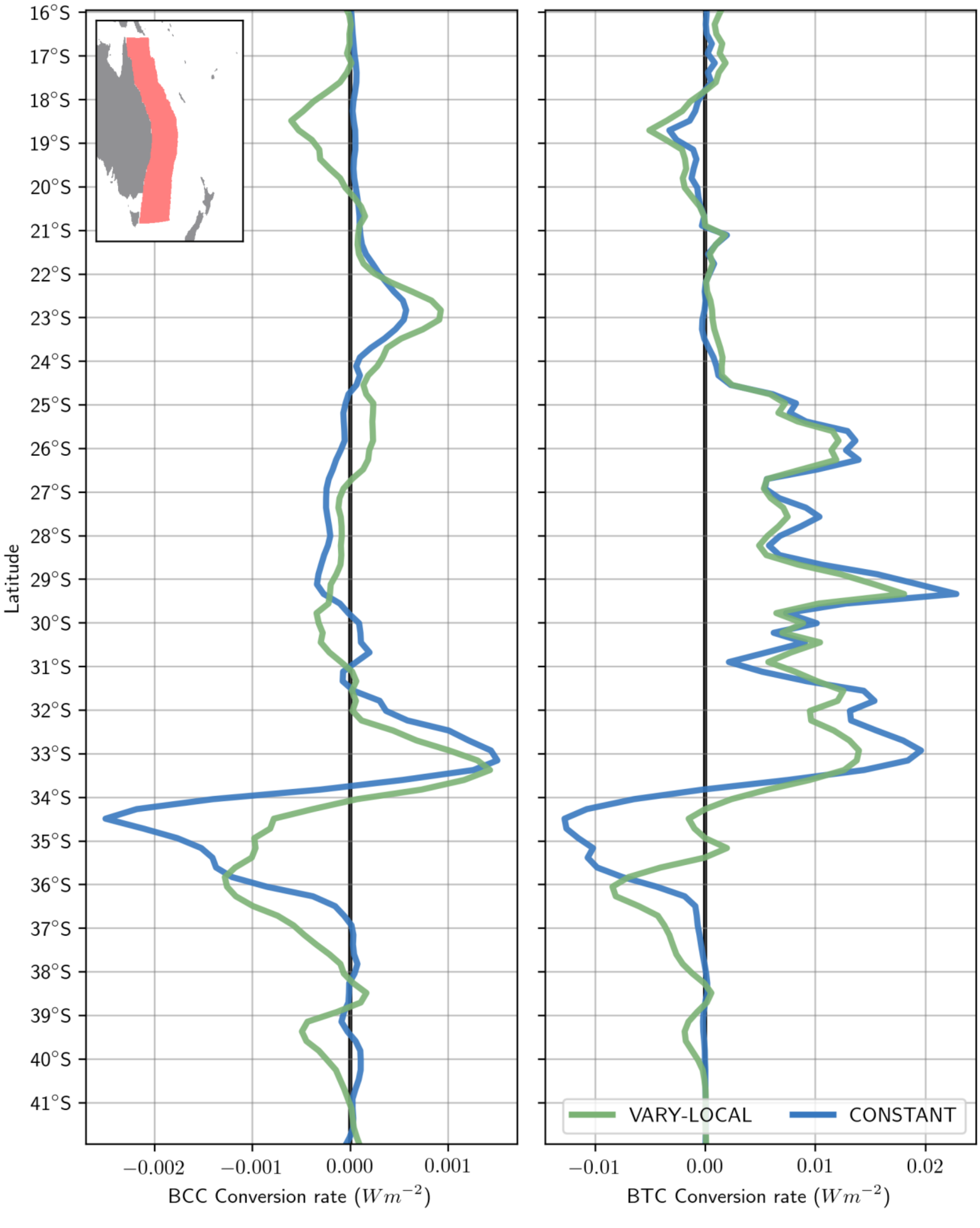

Figure 3-10. Baroclinic (left) and barotropic (right) conversion terms. Integrated vertically over the upper 200m and zonally over a band of 10° bounded on the west by the coastline (shaded on inset map).

To look at changes along the EAC, we follow a similar integration method to *Oliver et al.* [2015]: the coastally bound 10° offshore of the Australian continent is integrated in the upper 200m for the BCC and BTC conversion terms, shown in Figure 3-10. Whilst this integration provides a convenient summary we note that it involves cancellation between positive and negative terms and so only highlights the net energy transfer. The biggest change is seen at ~34.5°S, where the VARY-LOCAL experiment shows weaker conversion into the mean field (smaller negative values for both BCC and BTC), consistent with weaker EKE in the separation region in VARY-LOCAL (see Figure 3-8). Consistent with a stronger EAC extension, south of 36°S, VARY-LOCAL has enhanced eddy to mean flow conversion in both BCC and BTC.

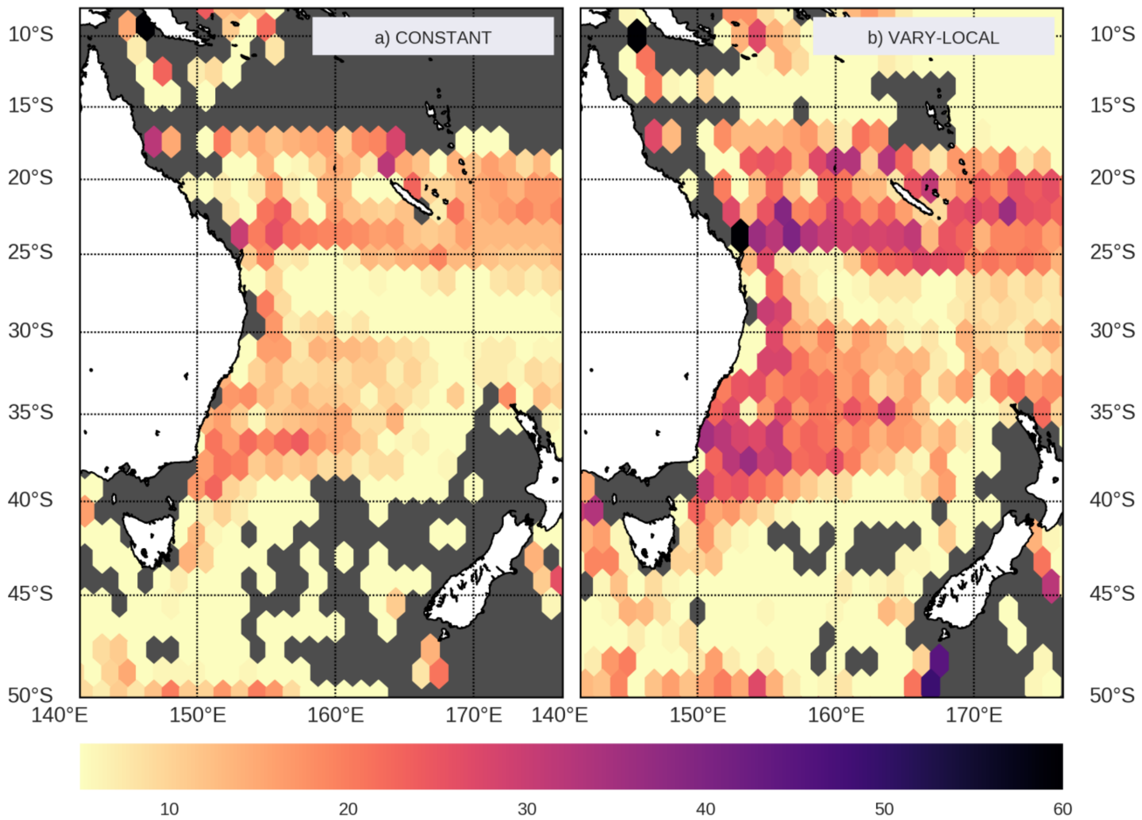

Figure 3-11. Total eddy count for tracked eddies with lifetimes of at least 4 days. Gray indicates areas of no data or where fewer than five eddies were detected. Eddies are only counted in each pixel or 'hexbin' once in their tracked lifetime. a) CONSTANT and b) VARY-LOCAL experiment.

Figure 3-11 shows large-scale differences between the eddy tracks of CONSTANT and VARY-ALL; the eddies are tracked using the method described in Section 3.2.5. Specifically, Figure 3-11 shows eddies that have been tracked for at least 4 days. Compared to VARY-ALL, the CONSTANT experiment has large regions where no or fewer than five eddies were detected (grey hexbins); for example over the northern area of the domain (8°S -20°S, 140°E-175°E) and in the Tasman Sea on the western side of New Zealand. The most striking difference between the two experiments is the increase in the number of eddies upstream in the EAC and offshore into the Pacific north and south of New Caledonia (20°S -25°S, 153°E-175°E).

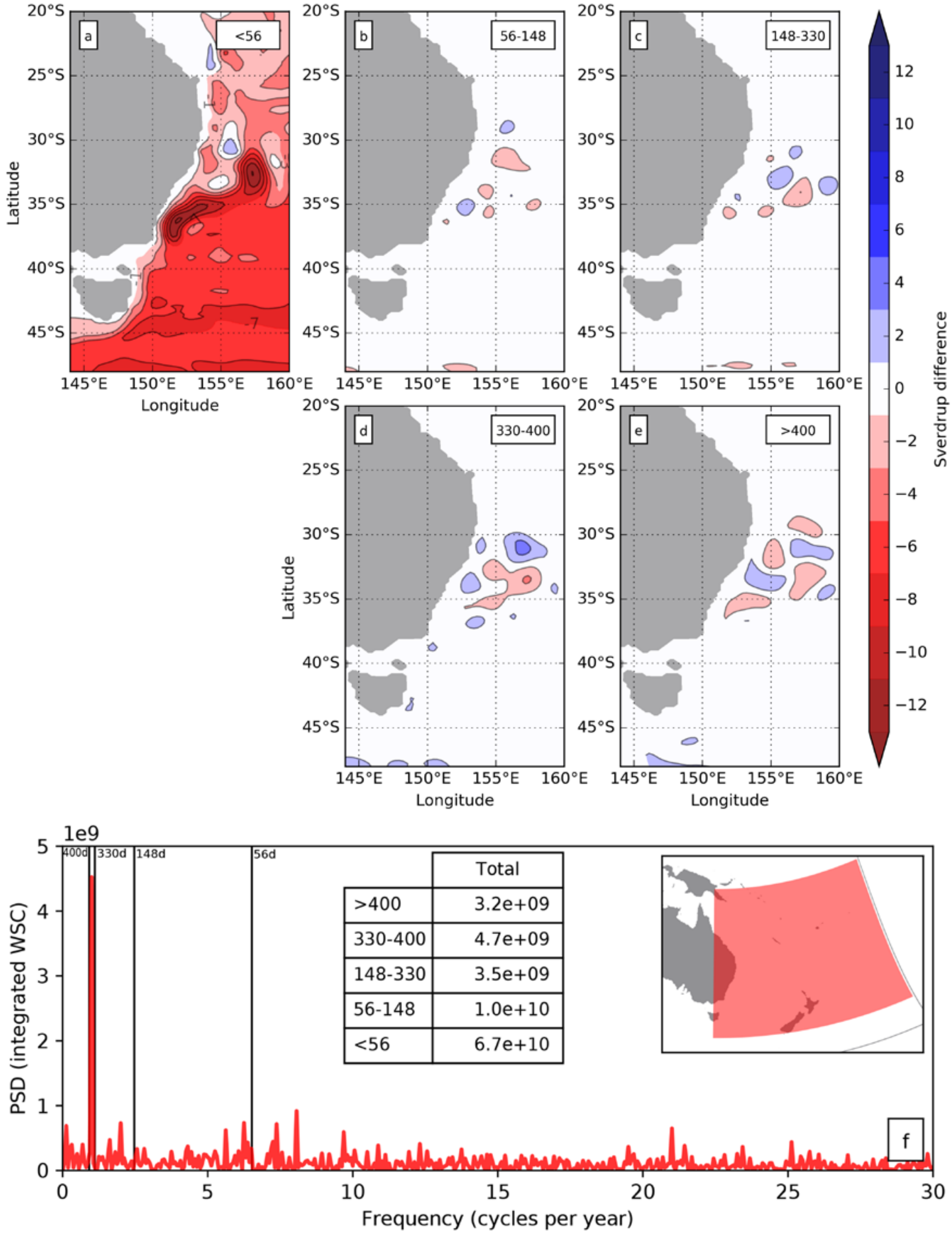

Figure 3-12. a-e) Time-mean barotropic streamfunction difference between filtered regional wind stress experiment and CONSTANT (integration taken eastward from Australia down to 1945m; contours every 2 Sv; matches Figure 3-4a for comparison). Wind stress is filtered, retaining only periods a) <56 days b) 56-148 days c) 148-330 days d) 330-400 days e) >400 days. f) Power spectral density of the integrated wind stress curl (between Jan. 1994 – Dec. 2009) for south-western Pacific Ocean (shaded red in inset).

Black lines indicate where the wind stress filtering occurs between experiments and the table indicates the total integrated wind stress curl for the filtered experiments 5-9 (see Table S1).

Figure 3-12a-e presents additional experiments (Section 3.2.2) with filtered wind stress variability and all other surface and boundary fluxes held constant; Figure 3-12f shows the power spectrum of the spatially-integrated wind stress curl with the filter band edges marked. Figure 3-12 a closely resembles VARY-LOCAL (Figure 3-5a), showing that monthly to synoptic wind variability (faster than 56 days) is critically important for the rectified enhancement of the EAC extension (and also that variability of other surface fluxes is unimportant). In contrast, the lower frequency experiments in Figure 3-12b-e show little change in the EAC extension extent. This is an important result because high-frequency variability is not typically associated with the extent of the EAC extension (e.g. [*Cai*, 2006; *Hill et al.*, 2011; *Oliver and Holbrook*, 2014]). The importance of this high-frequency band is likely due to it containing more integrated variance than the others, despite having lower amplitude than the annual peak (see Figure 3-12f table; the total in the <56 day band is actually an underestimate, as the model output data was daily whereas the forcing was 3-hourly; in addition the spatial averaging reduces the high-frequency signal from synoptic weather).

3.5 Summary and Discussion

A hierarchy of ocean model simulations with the same time-mean wind-stress forcing was examined to understand the impacts of local and remote forcing variability on the EAC (here "local" means surface forcing over the regional domain, and "remote" means the ocean boundary forcing – see section 3.2.2). The modelled East Australian Current has high intrinsic variability when forced only by a time-mean steady wind field and surface fluxes. Oceanic variability through the remote ocean boundary conditions was found to have limited impact on the mean transport in the EAC extension and mean state of the Tasman Sea circulation. Given the high intrinsic variability (as shown in the CONSTANT experiment) and the limited impact of varying ocean boundary conditions, it is unsurprising that previous studies have only found weak correlations between EAC variability and climate modes such as ENSO [*Hu et al.*, 2015]. In comparison to steady forcing, we find that variability in the local forcing field creates: a rectified subsurface enhancement of the EAC with increased eddy variance in the upstream EAC, a shorter eddy shedding timescale, and a time-mean EAC extension that extends further south towards Tasmania. Although we find no evidence of phase-locking (e.g. [*Kiss and Frankcombe*, 2016]) between the seasonal cycle of the forcing field and EAC eddy-shedding, we do see a reduction in the variability of the eddy-shedding timing under variable surface forcing (Figure 3-15). Additional experiments (Figure 3-12) reveal that regional variability in the wind stress field shorter than 56 days accounts for the enhancement of the mean EAC extension, and that variability at longer timescales and/or in other surface fluxes is unimportant for this feature.

The impact of time-varying forcing (with the same time-mean) on the extent of the EAC extension has implications for climate change simulations in the Tasman Sea. Coastal downstream EAC extension sections JK and AB show a mean transport change of 7.4 and 5.5 Sv, respectively, between steady forcing (CONSTANT) and variable forcing (VARY-ALL) experiments. With a maximum standard error in the mean of 1.5 Sv, these changes are statistically significant. This is an important result as these are similar to the long-term changes in transports predicted by recent climate change simulations both in an eddy-resolving model (4.3 Sv at section AB [*Oliver and Holbrook*, 2014]) and the multi-model mean from 33 CMIP5 coupled simulations (6.8 Sv between 35-45°S [*Sen Gupta et al.*, 2016]). Both these studies look at changes in a time-mean component of the wind-stress curl (not the varying part) to explain simulated changes to the EAC extension, an assumption that is not uncommon (e.g. [*Cai*, 2006; *Hill et al.*, 2011; *Feng et al.*, 2016]). The present study suggests that long term trends in local, *high-frequency* variability (<56 days) are an important additional nonlinear consideration for climate change studies focusing on the spinup of the EAC.

The EAC inflows and formation regions are highly non-linear and baroclinic [*Webb*, 2000; *Qiu and Chen*, 2004; *Couvelard et al.*, 2008; *Srinivasan et al.*, 2017]. There is mounting evidence that WBCs are not strengthening in a time-mean Sverdrup-like response but rather with enhanced eddy fields [*Ganachaud et al.*, 2014; *Sloyan and O'Kane*, 2015; *Beal and Elipot*, 2016]. We offer additional dynamical insight into the historical spin-up/decadal variability mechanism put forward by *O'Kane et al.* [2014] and *Sloyan and O'Kane* [2015] and endorsed by *Oliver et al.* [2015] in an eddy-resolving future climate simulation. Specifically, we find evidence that appears consistent with parts of the mechanism presented in *Sloyan and O'Kane* [2015], namely that non-linear baroclinic offshore variability drives modest changes in the upstream EAC but strong changes in the EAC-extension, Tasman Sea stratification and thermocline depth (Figure 3-16). Our study extends *Sloyan and O'Kane* [2015] by using an eddy-permitting model. We also find a subsurface increase in MKE along the whole length of the EAC forced by local wind variability of timescales <56 days, rather than the low-frequency remote forcing implied by *Sloyan and O'Kane* [2015]. Unlike *Sloyan and O'Kane* [2015], we do not find that a weaker EAC transport at 28°S leads to a weaker EAC extension; however, we do find the well documented anti-correlation of the Tasman Front and EAC extension transports (e.g. [*Hill et al.*, 2011]). Future work could examine the role of resolution and realistic wind perturbations in the EAC extension and Tasman Front pathways (e.g. [*Loveday et al.*, 2014; *Holton et al.*, 2016; *Seager and Simpson*, 2016]).

Qiu and Chen [2004] suggested that the annual cycle of the South Equatorial Countercurrent's EKE was similar in phase and amplitude to the EAC, starting a discussion in the literature on whether the EAC was influenced by offshore variability. Whilst there is evidence of EAC variability being determined by offshore variability on decadal timescales [*Hill et al.*, 2008; *Holbrook et al.*, 2011], there has been little evidence of forced variability at mesoscale or eddy-shedding timescales [*Bowen et al.*, 2005; *Mata et al.*, 2006]. Consistent with *Bowen et al.* [2005] and *Mata et al.* [2006], our study finds that the EAC sheds eddies due to intrinsically generated mixed barotropic/baroclinic instabilities; we extend this paradigm by showing that the spatial location and conversion rate of instability can be influenced by local surface forcing variability. Whilst beyond the scope of this paper, an interesting extension would refine the size of the local surface forcing (i.e. spatially modify the forcing area from VARY-LOCAL) and qualify the importance of remote higher-period variability (>5-day means). In addition, the change in eddy shedding behaviour would benefit from a more detailed energetics analysis (e.g. [*Kang and Curchitser*, 2015; *Jouanno et al.*, 2016; *Zhao et al.*, 2016; *Zhong et al.*, 2016]).

Mesoscale ocean-atmosphere interactions are increasingly recognised as important for the pathway and extension of WBCs (e.g. [*Ma et al.*, 2016; *Renault et al.*, 2016a, 2017]). Here, we have studied the simplest scenario, uncoupled simulations under prescribed variable surface flux forcing (no bulk formulae); the simulations shown in Figure 3-12 also have no variability in buoyancy fluxes. By design then, this excludes: nonlinear feedback of air-sea turbulent fluxes (see [*Hogg et al.*, 2009; *Wu et al.*, 2016]) and in particular the 'eddy-killing effect', nonlinearity in the stress formula, and relative wind (e.g. [*Dawe and Thompson*, 2006; *Zhai et al.*, 2012; *Zhai*, 2013; *Renault et al.*, 2016b]). Future work could look at the sensitivity of the EAC extension extent to high-frequency forcing in more realistic frameworks. Given the increasing evidence for a South Pacific gyre in a transitional state responding to an evolving wind forcing [*Roemmich et* *al.*, 2016; *Yang et al.*, 2016], this kind of research is crucial if we wish to understand the past and future circulation of the Tasman Sea.

3.6 Supplementary Figures

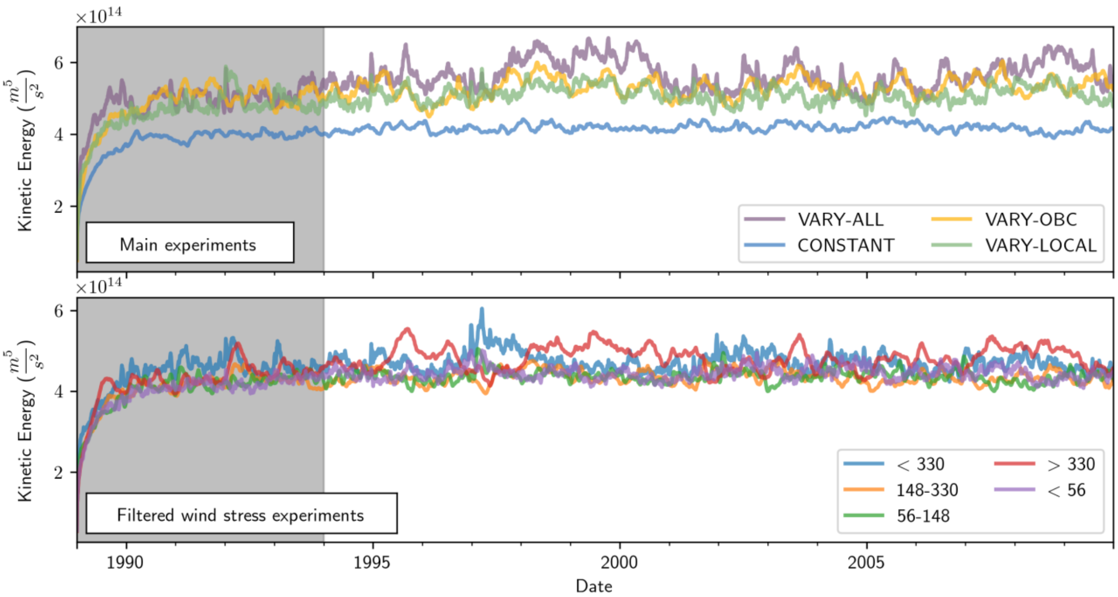

Figure 3-13. Times series of volume integrated Kinetic Energy $(\int \frac{1}{2}(u^2 + v^2)dV)$, grey shaded region (Jan. 1989 – Dec. 1993) indicates simulation years devoted to spin-up. All results presented in this study use daily-averaged model output from the subsequent 16 years of integration.

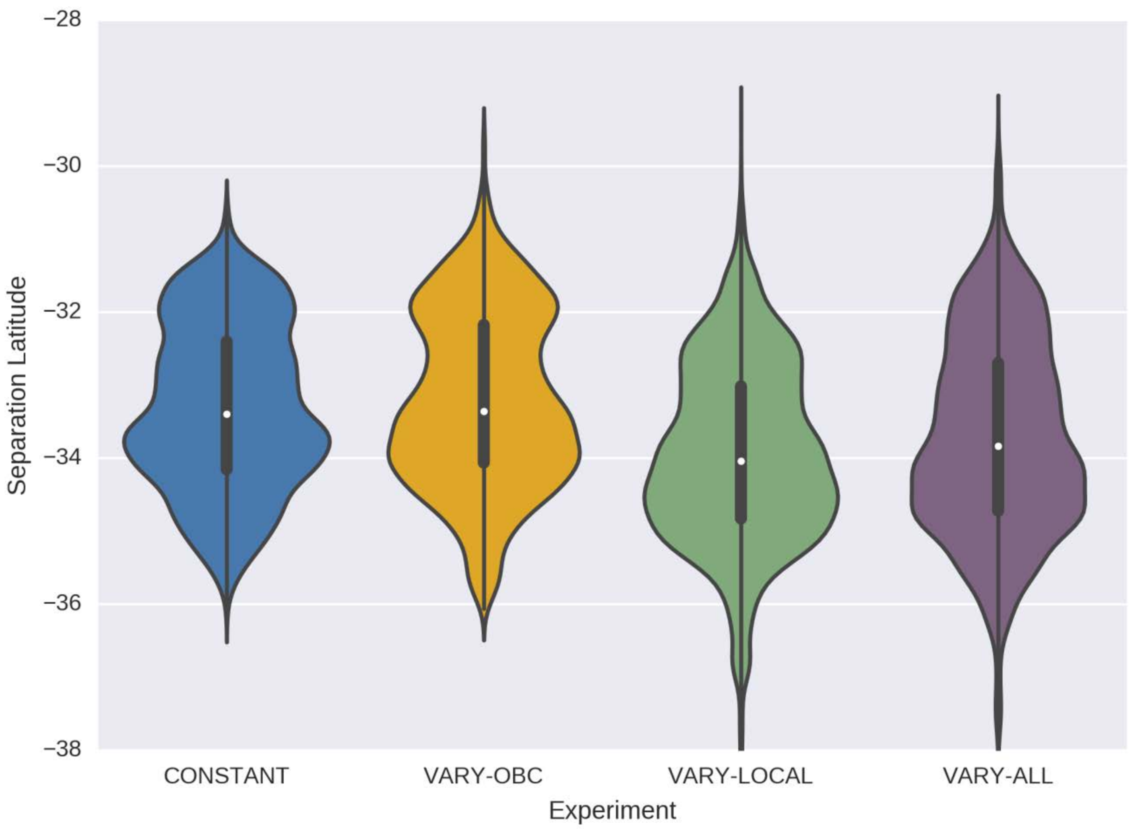

Figure 3-14. Violin plot of separation latitudes with a comparison between: between the four main experiments. Each box plot shows the inter-quartile range between the 25th-75th percentile. The median is represented by the line within the box. The shape of the 'violin' outlines the kernel density estimate.

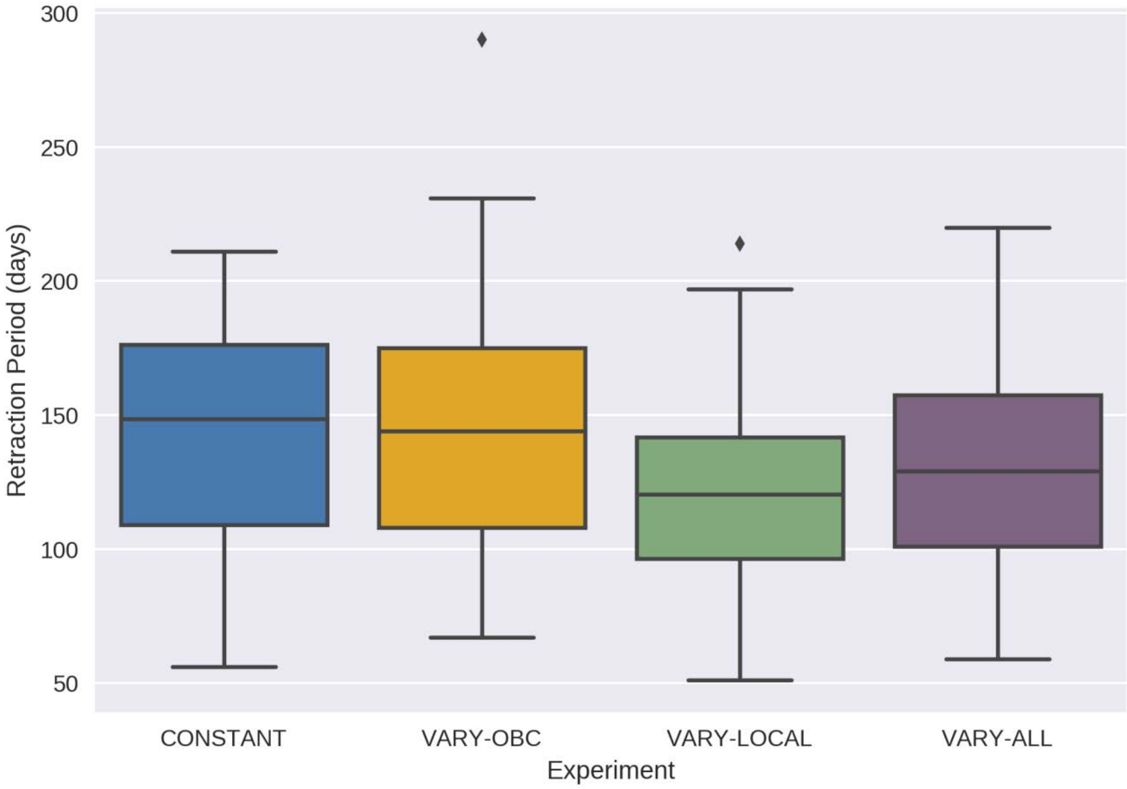

Figure 3-15. Boxplot of time between successive eddy retraction events for different experiments. An eddy retraction event is determined when the separation latitude jumps northward by more than 1.5° in a single time step. These times are indicated by blue circles in Figure 7.

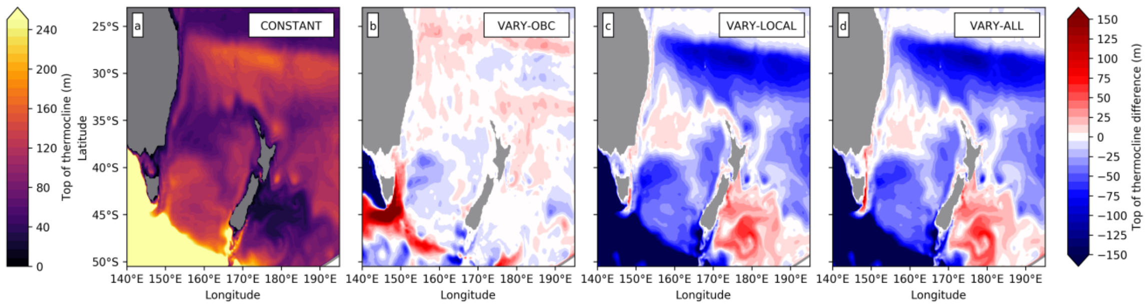

Figure 3-16. (a) CONSTANT top of thermocline depth. (b-c) Top of thermocline depth difference between CONSTANT and perturbed where red (blue) indicates areas where thermocline has been raised (lowered) compared to CONSTANT.

Concluding Remarks

This thesis characterised the role of non-linear processes and eddies in controlling Australia's boundary currents in terms of their circulation, dynamics and variability. Using the ocean circulation model NEMO we have used a range of modelling approaches including new analysis techniques and simulations. In the context of the Leeuwin Current (Part 1), the first quantitative assessment of Leeuwin Current pathways around Australia's southwest coastline were analyzed using offline particles and six coastally bound sectors. The remainder of this thesis (Part 2 and Part 3) focused on the partial separation of the East Australian Current. A hierarchy of sensitivity experiments exposed the complex interplay of factors that influence the EAC's separation. In Part 2 we explored the role of deep bathymetry and nonlinear processes in the partial separation of the EAC and circulation in the Tasman Sea. In Part 3, we examined the forcing factors that influence the mean state of the EAC (including the EAC separation), characterizing the EAC's intrinsic/forced variability in terms of both steady and variable forcing. These methods have allowed us to better understand the importance of non-linear dynamics and eddies in Australia's boundary currents.

This thesis aimed to investigate a series of questions (as set out in the Preface; page xxi) using the most relevant tools, diagnostics and modeling framework available. Part 1 of this thesis focused on the Leeuwin Current's source water pathways, and the role of eddy fluxes in modulating these pathways, and for this reason a Lagrangian framework in an eddy-resolving simulation was the most appropriate modelling choice. In contrast, Part 2 and Part 3 of this thesis focused more on the large-scale factors controlling the EAC separation; a smaller modelling domain, shorter simulations and a coarser NEMO model configuration facilitated a large number of simulations to be completed. We also utilised the ERA-Interim wind stress product for Part 2 and Part 3 as the reliability of the wind product was crucial to a realistic simulation (ERA-Interim uses continuous satellite wind stress coverage between early 1992 and 2009 [Dee et al., 2011]). Part 2 and Part 3 also switched from a Lagrangian to a Eulerian perspective, as the latter offered more insight into the underlying dynamics (e.g. mean to eddy conversion metrics in Section 3.2.6 on page 70). Combinations of these approaches do offer scope for further work and are discussed below (see Future work; page 102). In this final section, we briefly summarize the main findings of this thesis and suggest avenues for further research.

Summary of findings

Previous work by *Kundu and McCreary* [1986] suggested a possible advective pathway between the Indonesian Throughflow and the Leeuwin Current. *Domingues et al.* [2007] confirmed this general pathway, however more recently, *Lambert et al.* [2016] found no supporting evidence. Here, in Part 1 the first quantitative assessment of Leeuwin Current pathways found a mean poleward transport of 3.7 Sv in which the tropical sources account for 60–78% of the transport. The Lagrangian framework quantified the preferential pathway for Leeuwin Current waters to bifurcate away from the coast north of 30°S in a 1/10° degree global model. Beyond this latitude they were more likely to continue downstream. In particular, we suggested that eddy fluxes prevent significant transport travelling the entire length of the Leeuwin Current into the Great Australian Bight (only ~0.2 Sv makes this journey).

Previous work in the climate change attribution literature has invoked linear theory to attribute changes in the Tasman Sea circulation to changes in forcing (e.g. [*Wu et al.*, 2012; *Oliver and Holbrook*, 2014; *Feng et al.*, 2016; *Sen Gupta et al.*, 2016]). Here, utilizing a hierarchy of sensitivity experiments in Part 2 and Part 3, we have quantified the importance of non-linear processes in controlling the EAC separation latitude and circulation in the Tasman Sea. Part 2 of this thesis examined the role of deep bathymetry in the EAC separation; we progressively removed more of New Zealand across four experiments, whilst retaining the same atmospheric forcing. This was designed to test the established view (e.g. [*Tilburg et al.*, 2001; *Ridgway and Dunn*, 2003; *Bostock et al.*, 2006]) that a steep meridional gradient in the zonally-integrated wind stress curl solely determines the EAC time-mean separation latitude. We found that the complete removal of the New Zealand plateau leads to a smaller fraction of EAC transport heading east and more heading south, in other words, a weaker EAC separation. Specifically, the mean separation latitude shifted >100km southward; this is of a similar magnitude to changes simulated by climate change scenarios [*Matear et al.*, 2013; *Oliver and Holbrook*, 2014] and a hindcast simulation for the near-present day Tasman Sea [*Cetina-Heredia et al.*, 2014]. The circulation changes upon the complete removal of New Zealand demonstrate the importance of the New Zealand submarine platform in setting the spatial structure of temperature in the Tasman Sea. When New Zealand is completely removed, the greater southward migration of EAC extension eddies leads to a warming of ~2°C in the EAC extension region. To determine the underlying dynamics, we removed New Zealand with two linear models: the Sverdrup/Godfrey Island Rule [Sverdrup, 1947; Godfrey, 1989] and NEMO in linear mode. We found that linear processes and deep bathymetry play a major role in the mean Tasman Front position whereas non-linear processes are crucial for the extent of the EAC retroflection. Contrary to *Tilburg et al.* [2001], we find that meridional gradients in the basin-wide wind stress curl are not the sole factor determining EAC separation. Futhermore, the change in Tasman Sea outflow seen in linear NEMO but not *Tilburg et al.* [2001] is attributed to different meridional gradients in the integrated wind stress curl products used (ERA-Interim [*Dee et al.*, 2011] in NEMO and *Hellerman and Rosenstein* [1983] in *Tilburg et al.* [2001]).

Part 3 extended our analysis of the importance of non-linear processes in the EAC separation in a more climatically relevant scenario, namely, the roles of local and remote forcing variability in setting the mean state of the EAC, and its variability within the Tasman Sea circulation. To this end, a hierarchy of NEMO simulations was run; beginning with steady forcing, and then introducing variability in the remote ocean boundaries, followed by atmospheric variability in the local Australasian domain, and finally full variability in both local and remote regions. Oceanic variability through the remote ocean boundary conditions was found to have limited impact on the mean state of the EAC extension and Tasman Sea circulation. These simulations do show an EAC with high intrinsic variability and stochastic eddy shedding and demonstrate the non-linear response of the EAC to variable, non-stationary, inhomogeneous local surface forcing. We found that local, variable wind stress forcing, with a period shorter than ~2 months is responsible for a rectified Tasman Sea circulation which exhibits an enhanced EAC extension. The increased extent of the EAC extension is characterized by increases in eddy shedding rates, southward eddy propagation and increased EAC extension transports. An energetics framework suggests these EAC extension changes are coincident with increases in upstream eddy variance and an increase in sub-surface mean kinetic energy along the length of the EAC. The simulated time-mean increase in transport in the EAC extension under variable local surface forcing is of a similar magnitude to climate change simulations [*Oliver and Holbrook*, 2014; *Sen Gupta et al.*, 2016]. We therefore recommend that climate change attribution studies focusing on changes in the EAC extension also consider long term trends in local, *high-frequency* (< ~2 months) variability.

Future work

The findings of this thesis raise some interesting opportunities for further work; these are detailed below.

Dynamical connections between the LC and EAC are complicated by their different forcing mechanisms and the unique geometry in Australia's surrounding ocean basins. For example, the pressure gradient driving the LC is forced remotely by the Indonesian Throughflow and South Indian Counter Current, and rounding Cape Leeuwin the Leeuwin Current is directly wind forced [*Batteen and Miller*, 2009]. The EAC is in contrast a conventional western boundary current of a wind-driven gyre except that it has a relatively weak mean flow and high variability due to leakage through the Indonesian Throughflow. Despite these differences, some aspects of the modelling approaches used in Part 1 could be applied to the EAC, and similarly Part 3 to the LC. In the Tasman Sea climate change context, specifically, the gyre-scale response to changes in the westerlies, it is an open question as to whether the entire EAC spins up, or the EAC extension alone [*Ridgway*, 2007a; *Cetina-Heredia et al.*, 2014; *Sloyan and O'Kane*, 2015; *Feng et al.*, 2016]. With this issue in mind, an idealized climate change simulation with perturbed westerlies (e.g. [*Hogg et al.*, 2017]) could be examined using the Lagrangian analysis methods used in Part 1. This would track the complex inflow of pathways through the Coral Sea [*Couvelard et al.*, 2008; *Ganachaud et al.*, 2014] into the upstream EAC, providing information on the advective response time and the final fate of enhanced gyre transport in terms of the EAC spin-up. Conversely, the modelling approach used in Part 1 could be applied to the LC. Specifically, it has historically been believed that the LC's seasonality is derived from the alongshore equatorward wind stress being weakest in winter (e.g. [*Kundu and McCreary*, 1986; *Smith et al.*, 1991; *Benthuysen et al.*, 2014b]). Recent observationally based work by *Ridgway and Godfrey* [2015] suggests coastally trapped waves originating from the Gulf of Carpentaria (forced by monsoonal winds) are the dominant contributor to the Leeuwin Current's seasonal cycle. An interesting modelling study then, utilising similar techniques to Part 3, could introduce variability in western Australia's alongshore winds and then a separate simulation with the Gulf of Carpentaria's seasonally reversing monsoonal winds; these experiments would highlight the dynamical evolution of these two mechanisms.

Our work in Part 3 showed that wind frequencies with periods shorter than two months were particularly important for the extent of the EAC separation latitude; this is relevant because the EAC extent is normally associated with gyre-scale low-frequency wind variability (e.g. [*Cai*, 2006; *Hill et al.*, 2011; *Oliver and Holbrook*, 2014; *Feng et al.*, 2016]). Future work could identify the important forcing regions, their waveguides and the mechanisms by which they affect the EAC (e.g. [*Andres et al.*, 2011, 2012]). Past work suggests that the magnitude of the rectified currents in Part 3 is surprisingly large. *Willebrand et al.* [1980] found, due to a small Rossby number and lack of coherence, that rectified mean currents from varying winds alone (zero mean forcing) are expected to be of a small magnitude: ~2 Sv over 200km at a western boundary (less than half that seen in Part 3). Whilst the models and forcing used in Part 3 are very different to *Willebrand et al.* [1980], an idealized, process based study examining the evolution of the energetics (e.g. [*Jouanno et al.*, 2016; *Zhong et al.*, 2016; *Munday and Zhai*, 2017]) would reveal more details about the underlying dynamics. Our work in Part 3 also showed that the introduction of remote ocean variability has a small impact on the timing of EAC eddy shedding; future work could establish a mechanism by which this occurs and then look for a signal in the observations (e.g. [*Elipot and Beal*, 2015]).

Bibliography

Amante, C., and B. W. Eakins (2009), ETOPO1 1 Arc-Minute Global Relief Model: Procedures, Data Sources and Analysis, *NOAA Tech. Memo. NESDIS NGDC-24*, (March), 19, doi:10.1594/PANGAEA.769615.

Andres, M., Y. O. Kwon, and J. Yang (2011), Observations of the Kuroshio's barotropic and baroclinic responses to basin-wide wind forcing, *J. Geophys. Res. Ocean.*, *116*(4), 1–12, doi:10.1029/2010JC006863.

Andres, M., J. Yang, and Y.-O. Kwon (2012), Adjustment of a wind-driven two-layer system with mid-basin topography, *J. Mar. Res.*, *70*(6), 851–882, doi:10.1357/002224012806770946.

Ayers, J. M., P. G. Strutton, V. J. Coles, R. R. Hood, and R. J. Matear (2014), Indonesian throughflow nutrient fluxes and their potential impact on Indian Ocean productivity, *Geophys. Res. Lett.*, *41*(14), 5060–5067, doi:10.1002/2014GL060593.

Barnier, B., P. Marchesiello, A. P. De Miranda, and J. Molines (1998), A sigma-coordinate primitive equation model for studying the circulation in the South Atlantic . Part I : Model configuration with error estimates, , *45*, 543–572.

Barnier, B. et al. (2006), Impact of partial steps and momentum advection schemes in a global ocean circulation model at eddy-permitting resolution, *Ocean Dyn.*, *56*(5–6), 543–567, doi:10.1007/s10236-006-0082-1.

Barnier, B. et al. (2007), Eddy-permitting ocean circulation hindcasts of past decades, *CLIVAR Exch.*, *12*, 8–10.

Barnier, B., R. Dussin, and J. M. Molines (2011), *Scientific Validation Report (ScVR) for V1 Reprocessed Analysis and Reanalysis. WP 04 – GLO – CNRS_LEGI Grenoble.*

Batteen, M. L., and H. a. Miller (2009), Process-oriented modeling studies of the 5500-km-long boundary flow off western and southern Australia, *Cont. Shelf Res.*, *29*(4), 702–718, doi:10.1016/j.csr.2008.11.011.

Beal, L. M., and S. Elipot (2016), Broadening not strengthening of the Agulhas Current since the early 1990s, *Nature*, doi:10.1038/nature19853.

Benthuysen, J., R. Furue, J. P. McCreary, N. L. Bindoff, and H. E. Phillips (2014a), Dynamics of the Leeuwin Current: Part 2. Impacts of mixing, friction, and advection on a buoyancy-driven eastern boundary current over a shelf, *Dyn. Atmos. Ocean.*, *65*, 39–63, doi:10.1016/j.dynatmoce.2013.10.004.

Benthuysen, J., M. Feng, and L. Zhong (2014b), Spatial patterns of warming off Western Australia during the 2011 Ningaloo Niño: quantifying impacts of remote and local forcing, *Cont. Shelf Res.*

Bernie, D. J., S. J. Woolnough, J. M. Slingo, and E. Guilyardi (2005), Modeling diurnal and intraseasonal variability of the ocean mixed layer, *J. Clim.*, *18*(8), 1190–1202, doi:10.1175/JCLI3319.1.

Böning, C. W., and R. G. Budich (1992), Eddy Dynamics in a Primitive Equation Model: Sensitivity to Horizontal Resolution and Friction, *J. Phys. Oceanogr.*, *22*, 361–381.

Bostock, H. C., B. N. Opdyke, M. K. Gagan, A. E. Kiss, and L. K. Fifield (2006), Glacial/interglacial changes in the East Australian current, *Clim. Dyn.*, *26*(6), 645–659, doi:10.1007/s00382-005-0103-7.

Bowen, M. M., J. L. Wilkin, and W. J. Emery (2005), Variability and forcing of the East Australian Current, *J. Geophys. Res.*, *110*(C3), C03019, doi:10.1029/2004JC002533.

Cai, W. (2006), Antarctic ozone depletion causes an intensification of the Southern Ocean super-gyre circulation, *Geophys. Res. Lett.*, *33*(3), L03712, doi:10.1029/2005GL024911.

Cai, W., G. Shi, T. Cowan, D. Bi, and J. Ribbe (2005), The response of the Southern Annular Mode, the East Australian Current, and the southern mid-latitude ocean circulation to global warming, *Geophys. Res. Lett.*, *32*(23), L23706, doi:10.1029/2005GL024701.

Cetina-Heredia, P., M. Roughan, E. van Sebille, and M. A. Coleman (2014), Long-term trends in the East Australian Current separation latitude and eddy driven transport, *J. Geophys. Res. Ocean.*, *119*(7), 4351–4366, doi:10.1002/2014JC010071.Received.

Chamberlain, M. A., C. Sun, R. J. Matear, M. Feng, and S. J. Phipps (2012), Downscaling the climate change for oceans around Australia, *Geosci. Model Dev.*, *5*(5), 1177–1194, doi:10.5194/gmd-5-1177-2012.

Chassignet, E. P., and D. P. Marshall (2008), Gulf Stream Separation in Numerical Ocean Models, *Ocean Model. an Eddying Regime*, 39–61, doi:10.1029/177GM05.

Chelton, D. B., M. G. Schlax, and R. M. Samelson (2011), Global observations of nonlinear mesoscale eddies, *Prog. Oceanogr.*, *91*(2), 167–216, doi:10.1016/j.pocean.2011.01.002.

Chiswell, S. M., and P. J. Sutton (2015), Drifter- and float-derived mean circulation at the surface and 1000 m in the New Zealand region, *New Zeal. J. Mar. Freshw. Res.*, *49*(2), 259–277, doi:10.1080/00288330.2015.1008522.

Chiswell, S. M., H. C. Bostock, P. J. Sutton, and M. J. Williams (2015), Physical oceanography of the deep seas around New Zealand: a review, *New Zeal. J. Mar. Freshw. Res.*, *8330*(August 2015), 1–32, doi:10.1080/00288330.2014.992918.

Coleman, M., M. Feng, M. Roughan, P. Cetina-Heredia, and S. D. Connell (2013), Temperate shelf water dispersal by Australian boundary currents: Implications for population connectivity, *Limnol. Oceanogr. Fluids Environ.*, *3*, 295–309, doi:10.1215/21573689-2409306.

Couvelard, X., P. Marchesiello, L. Gourdeau, and J. Lefèvre (2008), Barotropic Zonal Jets Induced by Islands in the Southwest Pacific, *J. Phys. Oceanogr.*, *38*(10), 2185–2204, doi:10.1175/2008JPO3903.1.

Dai, A., and K. E. Trenberth (2002), Estimates of Freshwater Discharge from Continents: Latitudinal and Seasonal Variations, *J. Hydrometeorol.*, *3*(6), 660–687, doi:10.1175/1525-7541(2002)003<0660:EOFDFC>2.0.CO;2.

Dawe, J. T., and L. a. Thompson (2006), Effect of ocean surface currents on wind stress, heat flux, and wind power input to the ocean, *Geophys. Res. Lett.*, *33*(May), 1–5, doi:10.1029/2006GL025784.

Dee, D. P. et al. (2011), The ERA-Interim reanalysis: Configuration and performance of the data assimilation system, *Q. J. R. Meteorol. Soc.*, *137*(656), 553–597, doi:10.1002/qj.828.

Doddridge, E. W., D. P. Marshall, and A. M. Hogg (2016), Eddy Cancellation of the Ekman Cell in Subtropical Gyres, *J. Phys. Oceanogr.*, *46*(10), 2995–3010, doi:10.1175/JPO-D-16-0097.1.

Domingues, C. M., M. E. Maltrud, S. E. Wijffels, J. a. Church, and M. Tomczak (2007), Simulated Lagrangian pathways between the Leeuwin Current System and the upper-ocean circulation of the southeast Indian Ocean, *Deep Sea Res. Part II Top. Stud. Oceanogr.*, *54*(8–10), 797–817, doi:10.1016/j.dsr2.2006.10.003.

Döös, K. (1995), Interocean exchange of water masses, , *100*(95), 499–514.

Durgadoo, J. V., B. R. Loveday, C. J. C. Reason, P. Penven, and A. Biastoch (2013), Agulhas Leakage Predominantly Responds to the Southern Hemisphere Westerlies, *J. Phys. Oceanogr.*, *43*(10), 2113–2131, doi:10.1175/JPO-D-13-047.1.

Eden, C., and C. Böning (2002), Sources of Eddy Kinetic Energy in the Labrador Sea, *J. Phys. Oceanogr.*, *32*(12), 3346–3363, doi:10.1175/1520-0485(2002)032<3346:SOEKEI>2.0.CO;2.

Elipot, S., and L. M. Beal (2015), Characteristics, Energetics, and Origins of Agulhas Current Meanders and Their Limited Influence on Ring Shedding, *J. Phys. Oceanogr.*, *45*(9), 2294–2314, doi:10.1175/JPO-D-14-0254.1.

Everett, J. D., M. E. Baird, P. R. Oke, and I. M. Suthers (2012), An avenue of eddies: Quantifying the biophysical properties of mesoscale eddies in the Tasman Sea, *Geophys. Res. Lett.*, *39*(16), n/a-n/a, doi:10.1029/2012GL053091.

Feng, M. (2003), Annual and interannual variations of the Leeuwin Current at 32°S, *J. Geophys. Res.*, *108*(C11), 3355, doi:10.1029/2002JC001763.

Feng, M., S. Wijffels, S. Godfrey, and G. Meyers (2005), Do Eddies Play a Role in the Momentum Balance of the Leeuwin Current ?, *J. Phys. Oceanogr.*, *35*, 964–975.

Feng, M., A. Biastoch, C. Böning, N. Caputi, and G. Meyers (2008), Seasonal and interannual variations of upper ocean heat balance off the west coast of Australia, *J. Geophys. Res.*, *113*(C12), C12025, doi:10.1029/2008JC004908.

Feng, M., C. Böning, A. Biastoch, E. Behrens, E. Weller, and Y. Masumoto (2011), The reversal of the multi-decadal trends of the equatorial Pacific easterly winds, and the Indonesian Throughflow and Leeuwin Current transports, *Geophys. Res. Lett.*, *38*(11), n/a-n/a, doi:10.1029/2011GL047291.

Feng, M., M. J. McPhaden, S.-P. Xie, and J. Hafner (2013), La Niña forces unprecedented Leeuwin Current warming in 2011., *Sci. Rep.*, *3*, 1277, doi:10.1038/srep01277.

Feng, M., X. Zhang, P. Oke, D. Monselesan, M. Chamberlain, R. Matear, and A. Schiller (2016), Invigorating ocean boundary current systems around Australia during 1979–2014: As simulated in a near-global eddy-resolving ocean model, *J. Geophys. Res. Ocean.*, *121*, 3395–3408, doi:10.1002/2015JC011486.Received.

Fernandez, D., M. Bowen, and L. Carter (2014), Intensification and variability of the confluence of subtropical and subantartic boundary currents east of New Zealand, *J. Geophys. Res.*, 1–15, doi:10.1002/2013JC009153.Received.

Fransner, S. F. (2012), Effect of Model Settings on Western Boundary Currents in an Eddy Resolving Model, Université Joseph Fourier -Grenoble 1.

Furue, R., J. P. McCreary, J. Benthuysen, H. E. Phillips, and N. L. Bindoff (2013), Dynamics of the Leeuwin Current: Part 1. Coastal flows in an inviscid, variable-density, layer model, *Dyn. Atmos. Ocean.*, *63*, 24–59, doi:10.1016/j.dynatmoce.2013.03.003.

Furue, R., K. Guerreiro, H. E. Phillips, J. P. J. McCreary, and N. L. Bindoff (2017), On the Leeuwin Current System and Its Linkage to Zonal Flows in the South Indian Ocean as Inferred from a Gridded Hydrography, *J. Phys. Oceanogr.*, *47*(Lc), 583–602, doi:10.1175/JPO-D-16-0170.1.

Ganachaud, A. et al. (2014), The Southwest Pacific Ocean circulation and climate experiment (SPICE), *J. Geophys. Res. Ocean.*, *119*(11), 7660–7686, doi:10.1002/2013JC009678.

Gaspar, P., Y. Grégoris, and J.-M. Lefevre (1990), A simple eddy kinetic energy model for simulations of the oceanic vertical mixing: Tests at station Papa and long-term upper ocean study site, *J. Geophys. Res.*, *95*(C9), 16179, doi:10.1029/JC095iC09p16179.

Gersbach, G. H., C. B. Pattiaratchi, G. N. Ivey, and G. R. Cresswell (1999), Upwelling on the south-west coast of Australia—source of the Capes Current?, *Cont. Shelf Res.*, *19*(3), 363–400, doi:10.1016/S0278-4343(98)00088-0.

Godfrey, J. S. (1989), A Sverdrup model of the depth-integrated flow for the world ocean allowing for island circulations, *Geophys. Astrophys. Fluid Dyn.*, *45*(1–2), 89–112, doi:10.1080/03091928908208894.

Godfrey, J. S., G. R. Cresswell, T. J. Golding, A. F. Pearce, and R. Boyd (1980), The Separation of the East Australian Current, *J. Phys. Oceanogr.*, *10*(3), 430–440, doi:10.1175/1520-0485(1980)010<0430:TSOTEA>2.0.CO;2.

Gray, A. R., and S. C. Riser (2014), A Global Analysis of Sverdrup Balance Using Absolute Geostrophic Velocities from Argo, *J. Phys. Oceanogr.*, *44*(4), 1213–1229, doi:10.1175/JPO-D-12-0206.1.

Griffies, S. M. et al. (2009), Coordinated Ocean-ice Reference Experiments (COREs), *Ocean Model.*, *26*(1–2), 1–46, doi:10.1016/j.ocemod.2008.08.007.

Sen Gupta, A., S. McGregor, E. van Sebille, A. Ganachaud, J. Brown, and A. Santoso (2016), Future changes to the Indonesian Throughflow and Pacific circulation: the role of wind and deep circulation changes, *Geophys. Res. Lett.*

Haidvogel, D. B., and A. Beckmann (1999), *Numerical Ocean Circulation Modeling*, Imperical College Press, London.

Heath, R. A. (1985), Large-scale influence of the New Zealand seafloor topography on western boundary currents of the South Pacific Ocean., *Aust. J. Mar. Freshw. Res.*, *36*(Heath 19756), 1–14, doi:10.1071/MF9850001.

Hellerman, S., and M. Rosenstein (1983), Normal Monthly Wind Stress Over the World Ocean with Error Estimates, *J. Phys. Oceanogr.*, *13*(7), 1093–1104, doi:10.1175/1520-0485(1983)013<1093:NMWSOT>2.0.CO;2.

Hendon, H. H., and G. Wang (2009), Seasonal prediction of the Leeuwin Current using the POAMA dynamical seasonal forecast model, *Clim. Dyn.*, *34*(7–8), 1129–1137, doi:10.1007/s00382-009-0570-3.

Hill, K. L., S. R. Rintoul, R. Coleman, and K. R. Ridgway (2008), Wind forced low frequency variability of the East Australia Current, *Geophys. Res. Lett.*, *35*(8), 1–5, doi:10.1029/2007GL032912.

Hill, K. L., S. R. Rintoul, P. R. Oke, and K. Ridgway (2010), Rapid response of the East Australian Current to remote wind forcing: The role of barotropic-baroclinic interactions, *J. Mar. Res.*, *68*(3), 413–431, doi:10.1357/002224010794657218.

Hill, K. L., S. R. Rintoul, K. R. Ridgway, and P. R. Oke (2011), Decadal changes in the South Pacific western boundary current system revealed in observations and ocean state estimates, *J. Geophys. Res. Ocean.*, *116*(1), 1–12, doi:10.1029/2009JC005926.

Hogg, A. M., W. K. Dewar, P. Berloff, S. Kravtsov, and D. K. Hutchinson (2009), The effects of mesoscale ocean-atmosphere coupling on the large-scale ocean circulation, *J. Clim.*, *22*(15), 4066–4082, doi:10.1175/2009JCLI2629.1.

Hogg, A. M., P. Spence, and S. M. Downes (2017), The Energetics of Southern Ocean Upwelling, *J. Phys. Oceanogr.*, *47*.

Holbrook, N. J., I. D. Goodwin, S. McGregor, E. Molina, and S. B. Power (2011), ENSO to multi-decadal time scale changes in East Australian Current transports and Fort Denison sea level: Oceanic Rossby waves as the connecting mechanism, *Deep Sea Res. Part II Top. Stud. Oceanogr.*, *58*(5), 547–558, doi:10.1016/j.dsr2.2010.06.007.

Holton, L., J. Deshayes, B. C. Backeberg, B. R. Loveday, J. C. Hermes, and C. J. C. Reason (2016), Spatio-temporal characteristics of Agulhas leakage: a model intercomparison study, *Clim. Dyn.*, *48*(7), 1–15, doi:10.1007/s00382-016-3193-5.

Hu, D. et al. (2015), Pacific western boundary currents and their roles in climate, *Nature*, *522*(7556), 299–308, doi:10.1038/nature14504.

Jackett, D. R., and T. J. McDougall (1994), Minimal Adjustment of Hydrographic Profiles to Achieve Static Stability, *J. Atmos. Ocean. Technol.*, *12*, 381–389, doi:10.1175/1520-0426(1995)012<0381:MAOHPT>2.0.CO;2.

Jouanno, J., X. Capet, G. Madec, G. Roullet, and P. Klein (2016), Dissipation of the energy imparted by mid-latitude storms in the Southern Ocean, *Ocean Sci.*, *12*(3), 743–769, doi:10.5194/os-12-743-2016.

Kang, D., and E. N. Curchitser (2015), Energetics of Eddy-Mean Flow Interactions in the Gulf Stream Region, *J. Phys. Oceanogr.*, *45*, 1103–1120, doi:10.1175/JPO-D-14-0200.1.

Kiss, A., and L. M. Frankcombe (2016), The influence of periodic forcing on the time dependence of western boundary currents : Phase-locking, chaos, and the origins of low-frequency variability, *J. Phys. Oceanogr.*, *46:4*, 1117–1136, doi:10.1175/JPO-D-15-0113.1.

Kiss, A. E. (2010a), Dynamics of separating western boundary currents in ocean models, in *IOP Conference Series: Earth and Environmental Science*, vol. 11.

Kiss, A. E. (2010b), Dynamics of separating western boundary currents in ocean models, *IOP Conf. Ser. Earth Environ. Sci.*, *11*, 12034, doi:10.1088/1755-1315/11/1/012034.

Kundu, P. K., and J. P. McCreary (1986), On the Dynamics of the Throughflow from the Pacific into the Indian Ocean, *J. Phys. Oceanogr.*, *16*, 2191–2198.

Lambert, E., D. Le Bars, and W. P. M. de Ruijter (2016), The dynamic connection of the Indonesian Throughflow, South Indian Ocean Countercurrent and the Leeuwin Current, *Ocean Sci. Discuss.*, *12*(5), 2231–2256, doi:10.5194/osd-12-2231-2015.

Large, W. G., and S. G. Yeager (2004), Diurnal to decadal global forcing for ocean and sea--ice models: {The} data sets and flux climatologies., *NCAR Tech. Note*, *TN--460+ST*(May), 105pp, doi:10.5065/D6KK98Q6.

Large, W. G., and S. G. Yeager (2008), The global climatology of an interannually varying air–sea flux data set, *Clim. Dyn.*, *33*(2–3), 341–364, doi:10.1007/s00382-008-0441-3.

Lee, S., W. Park, M. O. Baringer, A. L. Gordon, B. Huber, and Y. Liu (2015), Pacific origin of the abrupt increase in Indian Ocean heat content during the warming hiatus, *Nat. Geosci.*, (May), doi:10.1038/NGEO2438.

Levitus, S., M. Conkright, T. Boyer, T. O'Brien, J. Antonov, C. Stephens, L. Stathoplos, D. Johnson, and R. Gelfeld (1998), World Ocean Database 1998, Volume 1:

Introduction., *NOAA Atlas NESDIS 18.*, *1*, 346.

Loveday, B. R., J. V. Durgadoo, C. J. C. Reason, A. Biastoch, and P. Penven (2014), Decoupling of the Agulhas leakage from the Agulhas Current, *J. Phys. Oceanogr.*, *44*, 140411151744003, doi:10.1175/JPO-D-13-093.1.

Ma, X. et al. (2016), Western boundary currents regulated by interaction between ocean eddies and the atmosphere, *Nature*, *535*(7613), 533–537, doi:10.1038/nature18640.

Madec, G. (2008), NEMO ocean engine, *Note du Pole modélisation, Inst. Pierre- Simon Laplace (IPSL), Fr.*, (27).

Madec, G. (2012), NEMO ocean engine, *Note du Pôle modélisation, Inst. Pierre-Simon Laplace*, (27), 357pp.

Marchesiello, P., and J. H. Middleton (2000), Modeling the East Australian Current in the Western Tasman Sea, *J. Phys. Oceanogr.*, *30*(11), 2956–2971, doi:10.1175/1520-0485(2001)031<2956:MTEACI>2.0.CO;2.

Marchesiello, P., J. C. Mcwilliams, and A. Shchepetkin (2001), Open boundary conditions for long-term integration of regional oceanic models, , *3*.

Mata, M. M., M. Tomczak, S. Wijffels, and J. a Church (2000), East Australian Current volume transports at 30°S: Estimates from the World Ocean Circulation Experiment hydrographic sections PR11/P6 and the PCM3 current meter array, *J. Geophys. Res.*, *105*(C12), 28509–28526, doi:10.1029/1999jc000121.

Mata, M. M., S. E. Wijffels, J. A. Church, and M. Tomczak (2006), Eddy shedding and energy conversions in the East Australian Current, *J. Geophys. Res.*, *111*(C9), C09034, doi:10.1029/2006JC003592.

Matear, R. J., M. A. Chamberlain, C. Sun, and M. Feng (2013), Climate change projection of the Tasman Sea from an Eddy-resolving Ocean Model, *J. Geophys. Res. Ocean.*, *118*(6), 2961–2976, doi:10.1002/jgrc.20202.

McCreary, J. P., S. R. Shetye, and P. K. Kundul (1986), Thermohaline forcing of eastern boundary currents : off the west coast of Australia, *J. Mar. Res.*, *44*, 71–92.

Menezes, V. V., H. E. Phillips, A. Schiller, C. M. Domingues, and N. L. Bindoff (2013), Salinity dominance on the Indian Ocean Eastern Gyral current, *Geophys. Res. Lett.*, *40*(21), 5716–5721, doi:10.1002/2013GL057887.

Menezes, V. V., M. L. Vianna, and H. E. Phillips (2014a), Aquarius sea surface salinity in the South Indian Ocean: Revealing annual period planetary waves, *J. Geophys.*

Res. Ocean., 3883–3908, doi:10.1002/2014JC009935.Received.

Menezes, V. V., H. E. Phillips, A. Schiller, N. L. Bindoff, C. M. Domingues, and M. L. Vianna (2014b), South Indian Countercurrent and associated fronts, *J. Geophys. Res. Ocean.*, *119*(10), 6763–6791, doi:10.1002/2014JC010076.Received.

Meuleners, M. J., C. B. Pattiaratchi, and G. N. Ivey (2007), Numerical modelling of the mean flow characteristics of the Leeuwin Current System, *Deep Sea Res. Part II Top. Stud. Oceanogr.*, *54*(8–10), 837–858, doi:10.1016/j.dsr2.2007.02.003.

Middleton, J. F., and J. a. T. Bye (2007), A review of the shelf-slope circulation along Australia's southern shelves: Cape Leeuwin to Portland, *Prog. Oceanogr.*, *75*(1), 1–41, doi:10.1016/j.pocean.2007.07.001.

Morrow, R., F. Fang, M. Fieux, and R. Molcard (2003), Anatomy of three warm-core Leeuwin Current eddies, *Deep Sea Res. Part II Top. Stud. Oceanogr.*, *50*(12–13), 2229–2243, doi:10.1016/S0967-0645(03)00054-7.

Morrow, R., F. Birol, D. Griffin, and J. Sudre (2004), Divergent pathways of cylonic and anti-cyclonic ocean eddies, *Geophys. Res. Lett.*, *31*(24), 1–5, doi:10.1029/2004GL020974.

Munday, D. R., and X. Zhai (2017), The Impact of Atmospheric Storminess on the Sensitivity of Southern Ocean Circulation to Wind Stress Changes, *Ocean Model.*, *115*, 14–26, doi:10.1016/j.ocemod.2017.05.005.

Munk, W. H. (1950), On the wind-driven ocean circulation, *J. Meteorol.*, *7*(2), 80–93.

Nilsson, C. S., and G. R. Cresswell (1980), The formation and evolution of East Australian current warm-core eddies, *Prog. Oceanogr.*, *9*(3), 133–183, doi:10.1016/0079-6611(80)90008-7.

O'Kane, T. J., R. J. Matear, M. A. Chamberlain, E. C. J. Oliver, and N. J. Holbrook (2014), Storm tracks in the Southern Hemisphere subtropical oceans, *J. Geophys. Res. Ocean.*, *119*, 6078–6100, doi:10.1002/2014JC010192.Received.

Oliver, E. C. J., and N. J. Holbrook (2014), Extending our understanding of South Pacific gyre "spin-up": Modelling the East Australian Current in a future climate, *J. Geophys. Res. Ocean.*, n/a-n/a, doi:10.1002/2013JC009591.

Oliver, E. C. J., S. J. Wotherspoon, M. a. Chamberlain, and N. J. Holbrook (2013), Projected Tasman Sea Extremes in Sea Surface Temperature through the Twenty-First Century, *J. Clim.*, *27*, 1980–1998, doi:10.1175/JCLI-D-13-00259.1.

Oliver, E. C. J., T. J. O'Kane, N. J. Holbrook, T. J. O. Kane, and N. J. Holbrook (2015), Projected changes to Tasman Sea eddies in a future climate, *J. Geophys. Res. Ocean.*, *120*, 2331–2349.

Oliver, E. C. J., J. A. Benthuysen, N. L. Bindoff, A. J. Hobday, N. J. Holbrook, C. N. Cundy, and S. E. Perkins-Kirkpatrick (2017), The unprecedented 2015/16 Tasman Sea marine heatwave, *Nat. Commun.*, (May), 1–12, doi:10.1038/ncomms16101.

Palastanga, V., P. J. van Leeuwen, M. W. Schouten, and W. P. M. de Ruijter (2007), Flow structure and variability in the subtropical Indian Ocean: Instability of the South Indian Ocean Countercurrent, *J. Geophys. Res.*, *112*(C1), C01001, doi:10.1029/2005JC003395.

Paris, C. B., J. Helgers, E. van Sebille, and A. Srinivasan (2013), Connectivity Modeling System: A probabilistic modeling tool for the multi-scale tracking of biotic and abiotic variability in the ocean, *Environ. Model. Softw.*, *42*, 47–54, doi:10.1016/j.envsoft.2012.12.006.

Pearce, A., and M. Feng (2007), Observations of warming on the Western Australian continental shelf, *Mar. Freshw. Res.*, *58*(10), 914, doi:10.1071/MF07082.

Pearce, A., and C. Pattiaratchi (1998), The Capes Current: a summer countercurrent flowing past Cape Leeuwin and Cape Naturaliste, Western Australia, *Cont. Shelf Res.*, *19*(3), 401–420, doi:10.1016/S0278-4343(98)00089-2.

Pedlosky, J. (1965), A study of the Time Dependent Ocean Circulation, *J. Atmos. Sci.*, *22*, 267–272.

Pedlosky, J. (1996), *Ocean circulation theory*, Springer.

Penduff, T., J. Le Sommer, B. Barnier, a.-M. Treguier, J.-M. Molines, and G. Madec (2007), Influence of numerical schemes on current-topography interactions in 1/4° global ocean simulations, *Ocean Sci. Discuss.*, *4*(3), 491–528, doi:10.5194/osd-4-491-2007.

Penduff, T., M. Juza, B. Barnier, J. Zika, W. K. Dewar, A. M. Treguier, J. M. Molines, and N. Audiffren (2011), Sea level expression of intrinsic and forced ocean variabilities at interannual time scales, *J. Clim.*, *24*(21), 5652–5670, doi:10.1175/JCLI-D-11-00077.1.

Penven, P., J. R. E. Lutjeharms, and P. Florenchie (2006), Madagascar: A pacemaker for the Agulhas Current system?, *Geophys. Res. Lett.*, *33*(17), 1–5, doi:10.1029/2006GL026854.

Pilo, G. S., P. R. Oke, T. Rykova, R. Coleman, and K. Ridgway (2015), Do East Australian Current anticyclonic eddies leave the Tasman Sea?, *J. Geophys. Res. Ocean.*, *120*, 8099–8114, doi:10.1002/2015JC011026.

Qiu, B., and S. Chen (2004), Seasonal Modulations in the Eddy Field of the South Pacific Ocean, *J. Phys. Oceanogr.*, *34*(7), 1515–1527, doi:10.1175/1520-0485(2004)034<1515:SMITEF>2.0.CO;2.

Renault, L., M. J. Molemaker, J. Gula, S. Masson, and J. C. McWilliams (2016a), Control and Stabilization of the Gulf Stream by Oceanic Current Interaction with the Atmosphere, *J. Phys. Oceanogr.*, JPO-D-16-0115.1, doi:10.1175/JPO-D-16-0115.1.

Renault, L., M. J. Molemaker, J. C. McWilliams, A. F. Shchepetkin, F. Lemarié, D. Chelton, S. Illig, and A. Hall (2016b), Modulation of Wind-Work by Oceanic Current Interaction with the Atmosphere, *J. Clim.*, 0–52, doi:10.1175/JPO-D-15-0232.1.

Renault, L., J. C. McWilliams, and P. Penven (2017), Modulation of the Agulhas Current Retroflection and Leakage by Oceanic Current Interaction with the Atmosphere in Coupled Simulations, *J. Phys. Oceanogr.*, doi:10.1175/JPO-D-16-0168.1.

Rhein, M. et al. (2013), 2013: Observations: Ocean, in *Climate Change 2013: The Physical Science Basis. Contribution of Working Group I to the Fifth Assessment Report of the Intergovernmental Panel on Climate Change*, edited by V. B. and P. M. M. Stocker, T.F., D. Qin, G.-K. Plattner, M. Tignor, S.K. Allen, J. Boschung, A. Nauels, Y. Xia, pp. 255–315, Cambridge University Press, United Kingdom and New York, NY, USA.

Rhines, P. B., and R. Schopp (1991), The Wind-driven Circulation: Quasi-geostrophic Simulations and Theory for Nonsymmetric Winds, *J. Phys. Oceanogr.*, *21*(9), 1438–1469, doi:10.1175/1520-0485(1991)021<1438:TWDCQG>2.0.CO;2.

Ridgway, K., J. R. Dunn, and J. L. Wilkin (2002), Ocean Interpolation by Four-Dimensional Weighted Least Squares — Application to the Waters around Australasia, *J. Atmos. Ocean. Technol.*, *19*(9), 1357–1375.

Ridgway, K. ., and J. . Dunn (2003), Mesoscale structure of the mean East Australian Current System and its relationship with topography, *Prog. Oceanogr.*, *56*(2), 189–222, doi:10.1016/S0079-6611(03)00004-1.

Ridgway, K. R. (2007a), Long-term trend and decadal variability of the southward penetration of the East Australian Current, *Geophys. Res. Lett.*, *34*(13), n/a-n/a, doi:10.1029/2007GL030393.

Ridgway, K. R. (2007b), Seasonal circulation around Tasmania: An interface between eastern and western boundary dynamics, *J. Geophys. Res.*, *112*(C10), C10016, doi:10.1029/2006JC003898.

Ridgway, K. R., and S. A. Condie (2004), The 5500-km-long boundary flow off western and southern Australia, *J. Geophys. Res.*, *109*(C4), C04017, doi:10.1029/2003JC001921.

Ridgway, K. R., and J. R. Dunn (2007), Observational evidence for a Southern Hemisphere oceanic supergyre, *Geophys. Res. Lett.*, *34*(13), n/a-n/a, doi:10.1029/2007GL030392.

Ridgway, K. R., and J. S. Godfrey (1994), Mass and heat budgets in the East Australian current: A direct approach, *J. Geophys. Res. Ocean.*, *99*, 3231–3248.

Ridgway, K. R., and J. S. Godfrey (1997), Seasonal cycle of the East Australian Current, *J. Geophys. Res.*, *102*(C10), 22921, doi:10.1029/97JC00227.

Ridgway, K. R., and J. S. Godfrey (2015), The source of the Leeuwin Current seasonality, *J. Geophys. Res. Ocean.*, *6843–6864*(120), doi:10.1002/2015JC011049.

Ridgway, K. R., R. C. Coleman, R. J. Bailey, and P. Sutton (2008), Decadal variability of East Australian Current transport inferred from repeated high-density XBT transects, a CTD survey and satellite altimetry, *J. Geophys. Res.*, *113*(C8), C08039, doi:10.1029/2007JC004664.

Roemmich, D., J. Gilson, R. Davis, P. Sutton, S. Wijffels, and S. Riser (2007), Decadal Spinup of the South Pacific Subtropical Gyre, *J. Phys. Oceanogr.*, *37*(2), 162–173, doi:10.1175/JPO3004.1.

Roemmich, D., J. Gilson, P. Sutton, and N. Zilberman (2016), Multidecadal Change of the South Pacific Gyre Circulation, *J. Phys. Oceanogr.*, *46*(6), 1871–1883, doi:10.1175/JPO-D-15-0237.1.

Saraceno, M., P. T. Strub, and P. M. Kosro (2008), Estimates of sea surface height and near-surface alongshore coastal currents from combinations of altimeters and tide gauges, *J. Geophys. Res. Ocean.*, *113*(11), 1–20, doi:10.1029/2008JC004756.

Schloesser, F. (2014), A Dynamical Model for the Leeuwin Undercurrent, *J. Phys. Oceanogr.*, *44*(7), 1798–1810, doi:10.1175/JPO-D-13-0226.1.

Schoonover, J., W. K. Dewar, N. Wienders, B. Deremble, J. Schoonover, W. K. Dewar, N. Wienders, and B. Deremble (2016), Local Sensitivities of the Gulf Stream Separation, *J. Phys. Oceanogr.*, (2008), JPO-D-16-0195.1, doi:10.1175/JPO-D-16-0195.1.

Schwarzkopf, F. U., and C. W. Böning (2011), Contribution of Pacific wind stress to multi-decadal variations in upper-ocean heat content and sea level in the tropical south Indian Ocean, *Geophys. Res. Lett.*, *38*(12), n/a-n/a, doi:10.1029/2011GL047651.

Seager, R., and I. R. Simpson (2016), Western boundary currents and climate change, *J. Geophys. Res. Ocean.*, *121*, 7212–7214, doi:10.1002/2016JC011935.Received.

van Sebille, E., P. J. van Leeuwen, A. Biastoch, and W. P. M. de Ruijter (2010), Flux comparison of Eulerian and Lagrangian estimates of Agulhas leakage: A case study using a numerical model, *Deep Sea Res. Part I Oceanogr. Res. Pap.*, *57*(3), 319–327, doi:10.1016/j.dsr.2009.12.006.

van Sebille, E., M. H. England, J. D. Zika, and B. M. Sloyan (2012), Tasman leakage in a fine-resolution ocean model, *Geophys. Res. Lett.*, *39*(6), doi:10.1029/2012GL051004.

van Sebille, E., P. Spence, M. R. Mazloff, M. H. England, S. R. Rintoul, and O. a. Saenko (2013), Abyssal connections of Antarctic Bottom Water in a Southern Ocean State Estimate, *Geophys. Res. Lett.*, *40*(December 2007), doi:10.1002/grl.50483.

van Sebille, E., J. Sprintall, F. U. Schwarzkopf, A. Sen Gupta, A. Santoso, M. H. England, A. Biastoch, and C. W. Böning (2014), Pacific to Indian Ocean connectivity: Tasman leakage, Indonesian Throughflow, and the role of ENSO, *J. Geophys. Res. Ocean.*, *119*(2), 1365–1382.

van Sebille, E. et al. (2018), Lagrangian ocean analysis: Fundamentals and practices, *Ocean Model.*, *121*(July 2016), 49–75, doi:10.1016/j.ocemod.2017.11.008.

Sérazin, G., T. Penduff, S. Grégorio, B. Barnier, J.-M. Molines, and L. Terray (2015), Intrinsic Variability of Sea Level from Global Ocean Simulations: Spatiotemporal Scales, *J. Clim.*, *28*(10), 4279–4292, doi:10.1175/JCLI-D-14-00554.1.

Siedler, G., M. Rouault, and J. R. E. Lutjeharms (2006), Structure and origin of the subtropical South Indian Ocean Countercurrent, *Geophys. Res. Lett.*, *33*(24), L24609, doi:10.1029/2006GL027399.

Sloyan, B. M., and T. J. O'Kane (2015), Oceans Drivers of decadal variability in the Tasman Sea, *J. Geophys. Res. Ocean.*, 1–18, doi:10.1002/2014JC010550.Received.

Sloyan, B. M., K. R. Ridgway, and R. Cowley (2016), The East Australian Current and Property Transport at 27 S from 2012-2013, *J. Phys. Oceanogr.*, 160108151222003, doi:10.1175/JPO-D-15-0052.1.

Smith, R., A. Huyer, J. S. Godfrey, and J. A. Church (1991), The Leeuwin current off western Australia, 1986-1987, *J. Phys. ...*, (21), 323–345.

Le Sommer, J., T. Penduff, S. Theetten, G. Madec, and B. Barnier (2009), How momentum advection schemes influence current-topography interactions at eddy permitting resolution, *Ocean Model.*, *29*(1), 1–14, doi:10.1016/j.ocemod.2008.11.007.

Speich, S., B. Blanke, P. De Vries, S. Drijfhouté, K. Döös, and A. Ganachaud (2002), Tasman leakage : A new route in the global ocean conveyor belt, *Geophys. Res. Lett.*, *29*(May).

Speich, S., B. Blanke, and W. Cai (2007), Atlantic meridional overturning circulation and the Southern Hemisphere supergyre, *Geophys. Res. Lett.*, *34*(23), n/a-n/a, doi:10.1029/2007GL031583.

Srinivasan, K., J. C. McWilliams, L. Renault, H. G. Hristova, J. Molemaker, and W. S. Kessler (2017), Topographic and Mixed Layer Submesoscale Currents in the Near-Surface Southwestern Tropical Pacific, *J. Phys. Oceanogr.*, *47*(6), 1221–1242, doi:10.1175/JPO-D-16-0216.1.

Stammer, D., and C. Wunsch (1999), Temporal changes in eddy energy of the oceans, *Deep. Res. Part II Top. Stud. Oceanogr.*, *46*(1–2), 77–108, doi:10.1016/S0967-0645(98)00106-4.

Stanton, B. R. (1979), The Tasman Front, *New Zeal. J. Mar. Freshw. Res.*, *13*(2), 201–214, doi:10.1080/00288330.1979.9515795.

Stanton, B. R. (1981), An oceanographic survey of the Tasman Front, *New Zeal. J. Mar. Freshw. Res.*, *15*(3), 289–297, doi:10.1080/00288330.1981.9515924.

Stewart, K. D., P. Spence, S. Waterman, J. Le Sommer, J. M. Molines, J. M. Lilly, and M. H. England (2015), Anisotropy of eddy variability in the global ocean, *Ocean Model.*, *95*, 53–65, doi:10.1016/j.ocemod.2015.09.005.

Stewart, K. D., A. M. Hogg, S. M. Griffies, and A. P. Heerdegen (2017), Vertical resolution of baroclinic modes in global ocean models, *Submitt. to Ocean Model.*, *113*, 50–65, doi:10.1016/j.ocemod.2017.03.012.

Stommel, H. (1948), The westward intensification of wind-driven ocean currents, *Eos, Trans. Am. Geophys. Union*, *29*(2), 202–206, doi:10.1029/TR029i002p00202.

Sun, C., M. Feng, R. J. Matear, M. a. Chamberlain, P. Craig, K. R. Ridgway, and A. Schiller (2012), Marine Downscaling of a Future Climate Scenario for Australian Boundary Currents, *J. Clim.*, *25*(8), 2947–2962, doi:10.1175/JCLI-D-11-00159.1.

Sutton, P. J. H., and M. Bowen (2014), Flows in the Tasman Front south of Norfolk Island, *J. Geophys. Res. Ocean.*, *119*(5), 3041–3053, doi:10.1002/2013JC009543.Received.

Sverdrup, H. U. (1947), Wind-Driven Currents in a Baroclinic Ocean; with Application to the Equatorial Currents of the Eastern Pacific, *Proc. Natl. Acad. Sci.*, (1), 318–326.

Swart, N. C., and J. C. Fyfe (2012), Observed and simulated changes in the Southern Hemisphere surface westerly wind-stress, *Geophys. Res. Lett.*, *39*(16), 6–11, doi:10.1029/2012GL052810.

Thomas, M. D., A. M. De Boer, H. L. Johnson, and D. P. Stevens (2014), Spatial and Temporal Scales of Sverdrup Balance*, *J. Phys. Oceanogr.*, *44*(10), doi:10.1175/JPO-D-13-0192.1.

Thompson, P. A., P. Bonham, P. Thomson, W. Rochester, M. A. Doblin, A. M. Waite, A. Richardson, and C. S. Rousseaux (2015), Climate variability drives plankton community composition changes: the 2010–2011 El Niño to La Niña transition around Australia, *J. Plankton Res.*, *37*(5), 966–984, doi:10.1093/plankt/fbv069.

Tilburg, C. E., H. E. Hurlburt, J. J. O'Brien, and J. F. Shriver (2001), The Dynamics of the East Australian Current System: The Tasman Front, the East Auckland Current, and the East Cape Current, *J. Phys. Oceanogr.*, *31*(10), 2917–2943, doi:10.1175/1520-0485(2001)031<2917:TDOTEA>2.0.CO;2.

Tomczak, M., and J. S. Godfrey (1994), *Regional oceanography: an introduction*, Pergamon.

Tomczak, M., and J. S. Godfrey (2003), *Regional Oceanography: an Introduction*, Daya Publishing House.

Veronis, G. (1970), Effect of fluctuating winds on ocean circulation, , *17*(November 1969).

Verron, J., and C. Le Provost (1991), Response of eddy-resolved general circulation numerical models to asymmetrical wind forcing, *Dyn. Atmos. Ocean.*, *15*(6), 505–

533, doi:10.1016/0377-0265(91)90002-W.

Waite, A. M. et al. (2007), The Leeuwin Current and its eddies: An introductory overview, *Deep Sea Res. Part II Top. Stud. Oceanogr.*, *54*(8–10), 789–796, doi:10.1016/j.dsr2.2006.12.008.

Wang, M., R. O'Rorke, a. M. Waite, L. E. Beckley, P. Thompson, and a. G. Jeffs (2015), Condition of larvae of western rock lobster (Panulirus cygnus) in cyclonic and anticyclonic eddies of the Leeuwin Current off Western Australia, *Mar. Freshw. Res.*, *122*, 1158–1167, doi:10.1016/j.pocean.2014.01.003.

Wang, X. H., V. Bhatt, and Y.-J. Sun (2013), Study of seasonal variability and heat budget of the East Australian Current using two eddy-resolving ocean circulation models, *Ocean Dyn.*, *63*(5), 549–563, doi:10.1007/s10236-013-0605-5.

Warren, B. A. (1970), General circulation in the South Pacific, in *Scientific Exploration of the South Pacific*, edited by W. S. Wooster, pp. 33–49, National Academy of Sciences.

Weaver, A. J., and J. H. Middleton (1989), On the Dynamics of the Leeuwin Current, *J. Phys. Oceanogr.*, *19*(5), 626–648.

Weaver, A. J., and J. H. Middleton (1990), An analytic model for the Leeuwin Current off western Australia, *Cont. Shelf Res.*, *10*(2), 105–122.

Webb, D. J. J. (2000), Evidence for Shallow Zonal Jets in the South Equatorial Current Region of the Southwest Pacific, *J. Phys. Oceanogr.*, *30*(4), 706–720, doi:10.1175/1520-0485(2000)030<0706:EFSZJI>2.0.CO;2.

Wernberg, T., B. Russell, P. J. Moore, S. D. Ling, D. a. Smale, A. Campbell, M. a. Coleman, P. D. Steinberg, G. a. Kendrick, and S. D. Connell (2011), Impacts of climate change in a global hotspot for temperate marine biodiversity and ocean warming, *J. Exp. Mar. Bio. Ecol.*, *400*(1–2), 7–16, doi:10.1016/j.jembe.2011.02.021.

Wilkin, J. L., and W. G. Zhang (2007), Modes of mesoscale sea surface height and temperature variability in the East Australian current, *J. Geophys. Res. Ocean.*, *112*(1), 1–14, doi:10.1029/2006JC003590.

Willebrand, J., S. G. H. Philander, and R. C. Pacanowski (1980), The Oceanic Response to Large-Scale Atmospheric Disturbances, *J. Phys. Oceanogr.*, *10*(3), 411–429, doi:10.1175/1520-0485(1980)010<0411:TORTLS>2.0.CO;2.

Woo, M., and C. Pattiaratchi (2008), Hydrography and water masses off the western Australian coast, *Deep Sea Res. Part I Oceanogr. Res. Pap.*, *55*(9), 1090–1104, doi:10.1016/j.dsr.2008.05.005.

Woo, M., C. Pattiaratchi, and W. Schroeder (2006), Dynamics of the Ningaloo Current off Point Cloates, Western Australia, *Mar. Freshw. Res.*, *57*(3), 291, doi:10.1071/MF05106.

Wu, L. et al. (2012), Enhanced warming over the global subtropical western boundary currents, *Nat. Clim. Chang.*, *2*(3), 161–166, doi:10.1038/nclimate1353.

Wu, Y., X. Zhai, and Z. Wang (2016), Impact of synoptic atmospheric forcing on the mean ocean circulation, *J. Clim.*, *29*(16), 5709–5724, doi:10.1175/JCLI-D-15-0819.1.

Xu, J., R. J. Lowe, G. N. Ivey, N. L. Jones, and R. Brinkman (2015), Observations of the shelf circulation dynamics along Ningaloo Reef, Western Australia during the austral spring and summer, *Cont. Shelf Res.*, *95*, 54–73, doi:10.1016/j.csr.2014.12.013.

Yang, H., G. Lohmann, W. Wei, M. Dima, M. Ionita, and J. Liu (2016), Intensification and poleward shift of subtropical western boundary currents in a warming climate, *J. Geophys. Res. Ocean.*, *121*, 4928–4945, doi:10.1002/2015JC011421.Received.

Ypma, S. L., E. van Sebille, A. E. Kiss, and P. Spence (2016), The separation of the East Australian Current: A Lagrangian approach to potential vorticity and upstream control, *J. Geophys. Res. Ocean.*, doi:10.1002/2014JC010632.

Zhai, X. (2013), On the wind mechanical forcing of the ocean general circulation, *J. Geophys. Res. Ocean.*, *118*(12), 6561–6577, doi:10.1002/2013JC009086.

Zhai, X., H. L. Johnson, D. P. Marshall, and C. Wunsch (2012), On the Wind Power Input to the Ocean General Circulation, *J. Phys. Oceanogr.*, *42*(8), 1357–1365, doi:10.1175/JPO-D-12-09.1.

Zhao, Y.-B., X. S. Liang, and J. Gan (2016), Nonlinear multiscale interactions and internal dynamics underlying a typical eddy-shedding event at Luzon Strait, *J. Geophys. Res. Ocean.*, *121*, 8208–8229, doi:10.1002/2016JC012483.Received.

Zhong, L., L. Hua, and D. Luo (2016), The Eddy–Mean Flow Interaction and the Intrusion of Western Boundary Current into the South China Sea–Type Basin in an Idealized Model, *J. Phys. Oceanogr.*, *46*(8), 2493–2527, doi:10.1175/JPO-D-15-0220.1.